NATIONAL AND KAPODISTRIAN UNIVERSITY OF ATHENS

SCHOOL OF SCIENCE
DEPARTMENT OF INFORMATICS AND TELECOMMUNICATIONS

INTERDISCIPLINARY POSTGRADUATE PROGRAM
"INFORMATION TECHNOLOGIES IN MEDICINE AND BIOLOGY"

MASTER'S THESIS

Modeling and simulations of functionalized magnetic nanoparticles as drug delivery systems

Konstantina D. Karathanou

Supervisor: **Dr. Zoe Cournia,** Researcher - Assistant Professor Level, Biomedical Research Foundation of the Academy of Athens (BRFAA)

ATHENS

OCTOBER 2017

ΕΘΝΙΚΟ ΚΑΙ ΚΑΠΟΔΙΣΤΡΙΑΚΟ ΠΑΝΕΠΙΣΤΗΜΙΟ ΑΘΗΝΩΝ

ΣΧΟΛΗ ΘΕΤΙΚΩΝ ΕΠΙΣΤΗΜΩΝ
ΤΜΗΜΑ ΠΛΗΡΟΦΟΡΙΚΗΣ ΚΑΙ ΤΗΛΕΠΙΚΟΙΝΩΝΙΩΝ

ΔΙΑΤΜΗΜΑΤΙΚΟ ΜΕΤΑΠΤΥΧΙΑΚΟ ΠΡΟΓΡΑΜΜΑ
"ΤΕΧΝΟΛΟΓΙΕΣ ΠΛΗΡΟΦΟΡΙΚΗΣ ΣΤΗΝ ΙΑΤΡΙΚΗ ΚΑΙ ΤΗ ΒΙΟΛΟΓΙΑ"

ΔΙΠΛΩΜΑΤΙΚΗ ΕΡΓΑΣΙΑ

Μοντελοποίηση και προσομοίωση μοριακής δυναμικής μαγνητικών νανοσωματιδίων ως συστημάτων μεταφοράς φαρμάκων

Κωνσταντίνα Δ. Καραθάνου

Επιβλέπουσα: **Δρ. Ζωή Κούρνια,** Ερευνήτρια Γ', Ίδρυμα Ιατροβιολογικών Ερευνών Ακαδημίας Αθηνών (ΙΙΒΕΑΑ)

ΑΘΗΝΑ

ΟΚΤΩΒΡΙΟΣ 2017

MASTER'S THESIS

Modeling and simulations of functionalized magnetic nanoparticles as drug delivery systems

Konstantina D. Karathanou
R.N.: PIV0126

SUPERVISOR: **Dr. Zoe Cournia,** Researcher - Assistant Professor Level, Biomedical Research Foundation of the Academy of Athens (BRFAA)

EXAMINATION COMITTEE:

Dr. Zoe Cournia, Researcher - Assistant Professor Level, Biomedical Research Foundation of the Academy of Athens (BRFAA)
Dr. George Spyrou, Head of the Bioinformatics Group, Cyprus Institute of Neurology and Genetics (CING)
Dr. Evangelia Chrysina, Researcher B - Institute of Biology, Medicinal Chemistry and Biotechnology, National Hellenic Research Foundation (NHRF)

October 2017

ΔΙΠΛΩΜΑΤΙΚΗ ΕΡΓΑΣΙΑ

Μοντελοποίηση και προσομοίωση μοριακής δυναμικής μαγνητικών νανοσωματιδίων ως συστημάτων μεταφοράς φαρμάκων

Κωνσταντίνα Δ. Καραθάνου

Α.Μ.: ΤΠΙΒ0126

ΕΠΙΒΛΕΠΟΥΣΑ: **Δρ. Ζωή Κούρνια,** Ερευνήτρια Γ', Ίδρυμα Ιατροβιολογικών Ερευνών Ακαδημίας Αθηνών (ΙΙΒΕΑΑ)

ΕΞΕΤΑΣΤΙΚΗ ΕΠΙΤΡΟΠΗ:

Δρ. Ζωή Κούρνια, Ερευνήτρια Γ', Ίδρυμα Ιατροβιολογικών Ερευνών Ακαδημίας Αθηνών (ΙΙΒΕΑΑ)
Δρ. Γεώργιος Σπύρου, Επικεφαλής της ομάδας Βιοπληροφορικής, Κυπριακό Ινστιτούτο Νευρολογίας και Γενετικής
Δρ. Ευαγγελία Χρυσίνα, Ερευνήτρια Β', Ινστιτούτο Βιολογίας, Φαρμακευτικής Χημείας και Βιοτεχνολογιας, Εθνικό Ίδρυμα Ερευνών (ΕΙΕ)

Οκτώβριος 2017

ABSTRACT

Nanoparticles (NPs) as drug delivery systems are engineered technologies for the delivery of therapeutic agents to their targets in a controlled manner and have shown significant potential to be employed in cancer treatment, with the aim to improve the biodistribution of cancer drugs. Magnetic nanoparticles (MNPs) are a class of nanoparticles, which can be manipulated using magnetic field gradients in order to reach the target site of interest and deliver the drug faster and more efficiently. Common MNPs consist of biocompatible iron oxide MNPs such as magnetite (Fe_3O_4) and its oxidized form maghemite (γ-Fe_2O_3) with proper surface architecture and conjugated targeting ligands/proteins.

A first consideration in assessing MNP toxicity as well as efficiency of translocation in a cell is the interaction of the MNP with the cell membrane. In the present thesis, computational approaches were used for the construction of functionalized magnetite MNPs of different shape, size, and surface chemistry. Subsequently, Molecular Dynamics (MD) simulations were performed to investigate the MNP in contact with a model cell membrane in order to gain insights into the physicochemical properties that govern the interactions between different classes of MNPs and the membrane.

Initially, a generic code that builds the model of the NP core of a given size and surface architecture was developed. The growing planes of the Fe_3O_4 crystal, which are analogous to the minimum surface energies, were used to extend the size and shape of the NP. This approach was generalized by developing an algorithm that constructs different crystal morphologies for a given crystal based on its preferred growing planes, the Miller indices and a user-defined size of the crystal. Subsequently, another algorithm was developed to attach polyvinyl alcohol (PVA) and polyarabic acid (ARA) ligands to the Fe_3O_4 MNP core. A dipalmitoylphosphatidylcholine (DPPC) lipid bilayer was then built as a model cell membrane. Finally, the two model MNPs were placed in the water phase of the lipid bilayer and atomistic MD simulations were performed in order to describe the nanoparticle-membrane interactions in atomic-level detail.

The results from our simulations were further compared to available experimental data from our collaborators and conclusions were drawn for the distinct interactions between the different ligand coating of the NP and the model cell membrane.

SUBJECT AREA: Computational Molecular Biophysics

KEYWORDS: nanoparticles, drug delivery systems, magnetite, molecular dynamics, atomistic simulations

ΠΕΡΙΛΗΨΗ

Τα νανοσωματίδια (NPs) ως συστήματα μεταφοράς φαρμάκων αφορούν τεχνολογίες μηχανικής για τη στοχευμένη μεταφορά και την ελεγχόμενη απελευθέρωση θεραπευτικών παραγόντων και παρουσιάζουν σημαντική επιστημονική υπόσχεση στη θεραπεία του καρκίνου, όπου χρησιμοποιούνται στη βελτίωση της βιοκατανομής των αντικαρκινικών φαρμάκων. Τα μαγνητικά νανοσωματίδια (MNPs) αποτελούν μια κατηγορία νανοσωματιδίων, τα οποία μπορούν να χρησιμοποιηθούν κάτω από την επίδραση έντασης μαγνητικού πεδίου με σκοπό να φτάσουν στη στοχευμένη περιοχή και να απελευθερώσουν το φάρμακο πιο γρήγορα και πιο αποτελεσματικά. Τέτοια σωματίδια συνήθως αποτελούνται από βιοσυμβατά MNPs οξειδίου του σιδήρου όπως είναι ο μαγνητίτης (Fe_3O_4) και η οξειδωμένη μορφή του, ο μαγεμίτης (γ-Fe_2O_3), με κατάλληλη αρχιτεκτονική επιφάνειας και συζευγμένα μόρια/πρωτείνες.

Η πρώτη εκτίμηση σχετικά με την τοξικότητα των MNPs καθώς και της αποτελεσματικής μεταφοράς τους στο κύτταρο, είναι η αλληλεπίδραση του MNP με την κυτταρική μεμβράνη. Στην παρούσα διπλωματική εργασία, χρησιμοποιήθηκαν υπολογιστικές προσεγγίσεις για την κατασκευή νανοσωματιδίων μαγνητίτη διαφορετικού σχήματος, μεγέθους και χημείας της επιφάνειάς τους. Ακολούθως, προσομοιώσεις μοριακής δυναμικής εφαρμόστηκαν για τη διερεύνηση της επαφής του MNP με την κυτταρική μεμβράνη, προκειμένου να αποκτηθεί γνώση των φυσικοχημικών ιδιοτήτων που διέπουν τις αλληλεπιδράσεις μεταξύ διαφορετικών κατηγοριών MNPs και της μεμβράνης.

Αρχικά, ένας γενικός κώδικας αναπτύχθηκε για την κατασκευή του μοντέλου πυρήνα νανοσωματιδίων δεδομένου μεγέθους και αρχιτεκτονικής επιφάνειας. Τα επίπεδα ανάπτυξης του Fe_3O_4 κρυστάλλου, τα οποία σχετίζονται με την ελάχιστη ενέργεια επιφάνειας, χρησιμοποιήθηκαν για την επέκταση του μεγέθους και σχήματος του νανοσωματιδίου. Η προσέγγιση αυτή γενικεύτηκε με την ανάπτυξη ενός αλγορίθμου κατασκευής διαφορετικών μορφολογιών κρυστάλλου με βάση τα επίπεδα ανάπτυξης του κρυστάλλου, τους δείκτες Miller και του κρυσταλλικού μεγέθους καθορισμένο από τον χρήστη. Ακολούθως, η υλοποίηση ενός άλλου προγράμματος επιτρέπει την πρόσδεση των αλυσίδων πολυβινυλικής αλκοόλης (PVA) και πολυακριλικού οξέως (ARA) στον Fe_3O_4 MNP πυρήνα. Η λιπιδική διπλοστοιβάδα (dipalmitoylphosphatidylcholine - DPPC) κατασκευάστηκε στη συνέχεια ως μοντέλο της κυτταρικής μεμβράνης. Τέλος, τα δύο μοντέλα MNPs τοποθετήθηκαν στην υδάτινη περιοχή της λιπιδικής διπλοστοιβάδας και ατομικιστικές προσομοιώσεις μοριακής δυναμικής εφαρμόστηκαν με σκοπό την περιγραφή των αλληλεπιδράσεων νανοσωματιδίου-μεμβράνης σε ατομικό επίπεδο.

Τα αποτελέσματα της προσομοίωσης συγκρίνονται περαιτέρω με τα διαθέσιμα πειραματικά δεδομένα από τους συνεργάτες μας και τα συμπεράσματα συντάσσονται ως πρός τις διαφορετικές αλληλεπιδράσεις μεταξύ διαφορετικών προσδετών του NP και του μοντέλου κυτταρικής μεμβράνης.

ΘΕΜΑΤΙΚΗ ΠΕΡΙΟΧΗ: Υπολογιστική Μοριακή Βιοφυσική

ΛΕΞΕΙΣ ΚΛΕΙΔΙΑ: νανοσωματίδια, συστήματα μεταφοράς φαρμάκων, μαγνητίτης, μοριακή δυναμική, ατομικιστικές προσομοιώσεις

To my family,

ACKNOWLEDGMENTS

I would like to take this opportunity to acknowledge those who have helped me complete this thesis. First and foremost, I would like to express my gratitude to my supervisor, Dr. Zoe Cournia, Researcher - Assistant Professor Level, at the Biomedical Research Foundation of the Academy of Athens (BRFAA) - her encouragement, support, and thoughtful advice have been immensely valuable for me and my academic steps. Her guidance helped me in my research and in writing this thesis.

I would like to thank Dr. Paraskevi Gkeka, Research Associate at the Biomedical Research Foundation Academy of Athens, with whom I worked closely in the beginning of this thesis. Dr. Gkeka introduced me to the methodology of this work and the topic of the thesis; I would like to thank her for all her valuable help as well as for her support along the way. I would also like to thank my examination committee, Dr. George Spyrou, Head of the Bioinformatics Group, Cyprus Institute of Neurology and Genetics (CING) and Dr. Evangelia Chrysina, Researcher B' at the Institute of Biology, Medicinal Chemistry and Biotechnology, National Hellenic Research Foundation (NHRF).

I would like to thank our collaborators Professor C. Demetzos and Dr. A. Pippa, Department of Pharmaceutical Technology, Faculty of Pharmacy, National and Kapodistrian University of Athens, Greece for their work on investigating the interactions of MAG-PVA and MAG-ARA, which is the topic of this thesis, with a DPPC bilayer using differential scanning calorimetry. Also, Dr. A. Klinakis and Dr. M. Patitsa, Biomedical Research Foundation of the Academy of Athens (BRFAA), for our collaboration in assessing these nanoparticles in vitro and in vivo.

My sincere thanks also goes to Dr. Xenophon Krokidis and Dr. Dora Spyriouni, who provided me the opportunity to work with them in a part of this project within the Scienomics company, at the National Center for Scientific Research "Demokritos", Athens, Greece, as an intern. With them I learned the principles of working in a company and applying my research on real life problems.

I thank my fellow labmates, Giannis Galdadas for valuable discussions and suggestions to my thesis, Dr. Hari Leontiadou, Dr. Spyros Vicatos, Marilena Liosi, Theodora Tafarli, Ioanna Tremi, Christina Athanasiou for the stimulating discussions, for working together and for all the fun times we had in the lab.

Last but not least, I would like to thank my family: my parents, my brother and all my friends for supporting me spiritually throughout writing this thesis and in my life in general.

CONTENTS

LIST OF FIGURES

LIST OF TABLES

PROLOGUE

The master thesis ‘Modeling and simulations of functionalized magnetic nanoparticles as drug delivery systems’, has been conducted at the Biomedical Research Foundation, Academy of Athens for completion of the Postgraduate Program "Information Technologies in Medicine and Biology" (I.T.M.B.), Department of Informatics and Telecommunications, National and Kapodistrian University of Athens, Greece.

The First Chapter presents the motivation of the study, the application of nanoparticles (NPs) in Medicine as drug delivery systems and their advantages, the importance of Magnetic Nanoparticles (MNPs) as a class of NPs, and their biodistribution within an organism along with the toxicity studies required. Furthermore, the characteristics of the plasma membrane and the lipid bilayer are presented and the nanoparticle-membrane interactions are explained. The study objectives are then defined.

The Second Chapter presents the theoretical foundations of the present work. First, an introduction to Molecular Dynamics (MD) simulations theory is presented and the potential energy function used (force field). The roots of MD lie in statistical mechanics, a branch of Physical Chemistry, which aims to construct macroscopic properties of a system from basic information about intermolecular interactions taken from the microscopic world. Next, an introduction of the principles of crystallographic techniques is presented, including crystal directions and planes. Finally, the information of the atomic structure of the magnetite is given, which is essential for the analysis of the computational approaches for the construction and modeling of functionalized magnetic nanoparticles (MNPs) used in this thesis.

The computational framework of the present thesis is presented in Chapter Three. An analysis of the tools developed during this study for the construction and modeling of magnetite nanoparticles (spherical or truncated MNPs) is presented along with a general code implementation for the computing of the macroscopic morphology of any periodic crystal using its stable growing planes and the distance from a reference point. Additionally, information about the functionalization of the magnetite (two types of ligands attached to the magnetite core) is given as well as details about the construction of the lipid bilayer that is used to model the cell membrane. Next, the development of the topology and parameter files for the magnetite core and ligands is described. The chapter closes with a discussion on the simulation setup of the two model MNPs in the water phase of the lipid bilayer and our results describing the nanoparticle-membrane interactions in atomic-level detail.

Finally, Chapter Four constitutes the epilogue of the thesis together with the conclusions and possible future extensions of our work.

1. INTRODUCTION

Although modern medicine has achieved remarkable progress in the field of cancer treatment, some cancer types remain hard to treat or are even untreatable in some cases, making cancer the second biggest cause of mortality worldwide with approximately 13% of all deaths accounted to untreated cancer [1]. In the past seven decades, cancer deaths are continuingly increasing, as opposed to other fatal diseases such as heart diseases, cerebrovascular diseases, pneumonia, viral infections etc., which are showing significant reduction [1].

Accessing the tumor microenvironment with drugs poses significant challenges. P-glycoproteins (P-gp) frequently become antagonists to conventional chemotherapy treatments by blocking the pharmaceutical substances from accessing the tumor mass [2] [6]. Furthermore, in vivo delivery of pharmacological agents faces a variety of physiological barriers as well. Such barriers include hepatic and renal clearance, enzymolysis and hydrolysis, endosomal/lysosomal degradation etc. [3] [4] [5] [6]. Additionally, the effectiveness of antitumor pharmaceutical substances is restricted by their substandard properties, such as reduced solubility, constricted therapeutic window, and increased cytotoxicity causing extensive damages to healthy tissues, which contribute to reduced cancer treatment success [7] [8].

Worldwide research is currently concentrating in the development and investigations of new therapeutic methods, which will prevail over the disadvantages observed by traditional drugs, but at the same time successfully annihilate tumors, with a major goal being the preservation of surrounding healthy tissue and minimization of relapse resistant.

Drug delivery systems are engineered technologies for the delivery of therapeutic agents to their targets in a controlled manner. Nanoparticles (NPs) as drug delivery systems have shown significant promise in cancer treatment, where they are used to improve the biodistribution of cancer drugs. The design of nanoplatforms has so far included the use of a variety of nanoparticles including, -fibers, -gels, liposomes, dendrimers, or quantum dots [9] [10] [11]. These nanoparticles contain desirable qualities, such as biological stability and biocompatibility, making them much more flexible when route of administration is concerned since they can be delivered to the target mass through a variety of administration routes while integrating an extensive range of drug molecules. Additionally, these nanoparticles exhibit easiness of surface modification (like in the case of Tween 80, polyethylene glycol (PEG) or poloxamers and poloxamines) thus extending their circulation time [12] [13] [14]. Even more, these particles exhibit large versatility of functionalization which in turn improves their selectivity against tumor growths. Therefore these may demonstrate lower toxicity and therapeutic effect enhancement, a well-known obstacle in today's chemotherapeutic methods. Thus, the use of nanoparticles has the potential to become a much safer means of cancer therapy and management, since the patient's health and health related quality of life are compromised in a lower degree [15].

For designing an effective NP, the consideration of the size, shape, surface chemistry, patient-specific information, and other parameters is crucial. Optimizing all of these parameters through experiments is both time and resource-intensive. Therefore, computational modeling is used to reduce this possibility space. Simulations have been

used to model the continuum of the NP transport at the tumor site and investigate the physical interactions between NPs and the cell membrane.

The aim of this thesis is to a) create a general methodology/algorithm for creating crystal NPs according to their preferred growing planes, b) create a general methodology/algorithm for functionalizing these NPs with ligands, and c) model the interaction of the NPs with the cell membrane using Molecular Dynamics simulations in order to understand their interaction with the lipid bilayer. Research of these nanocarriers is a dynamic field prompting more useful therapeutic efficacy through advances in material construction, auxiliary outline and cell targeting. The joining of forces of multiple scientific fields such as, material, engineering and information technology outlines a new era in medical science, one where medications will have generously expanded adequacy and administration convenience with high bioavailability and less adverse effects [16].

1.1 Nanoparticles (NPs) as Drug Delivery System

Nanotechnology is defined as the formation and exploitation of materials, designs and frameworks through the control of substances on the nanometer-length scale, i.e., at the level of particles, atoms and supramolecular structures [17] [18]. The use of nanotechnology in different scientific fields and particularly in medicine, is slowly but steadily increasing and the road to replacing conventional medications has just started. Therefore, even though satisfactory drug delivery is the foremost challenge that biotechnological and pharmaceutical research has to overcome, it seems as though nanotechnology can advocate the innovation of drug development for commercial use in the near future [19]. Nanotechnology concentrates on manufacturing therapeutic substances in biocompatible nanocarriers, such as NPs, nanocapsules, micellar systems and dendrimers (Figure 1) [20] [21]. Moreover, one of the major advantages that nanotechnology offers is targeted drug delivery to the site of disease.

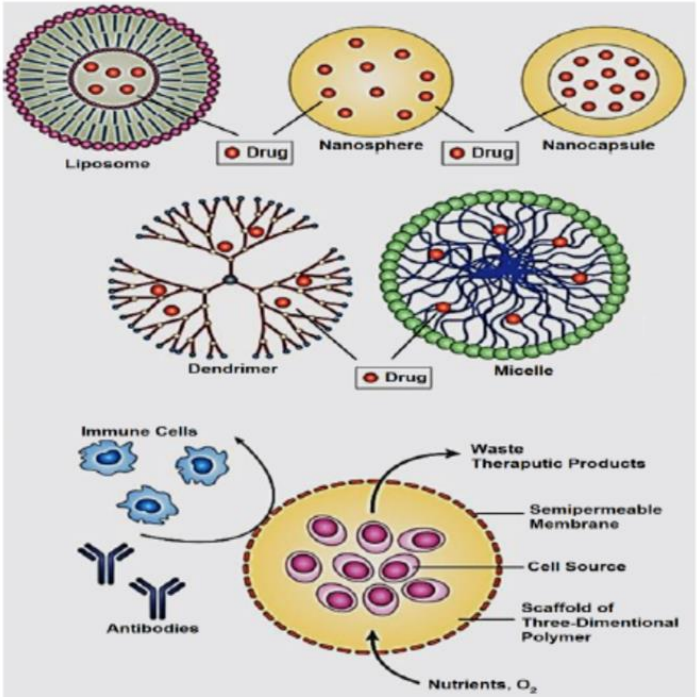

Figure 1: Schematic representation of different nanotechnology-based drug-delivery systems. [21]

1.1.1 Nanoparticles in medicine

Therapeutics

A large reference database reveals the therapeutic use of NPs in vitro and in vivo applications. The therapeutic use of NPs is wide, showing a range from cancer therapy and management application to microbial therapeutic effects, vaccination efficacy, gene delivery and site-specific targeting, while subsiding the adverse effects observed by current therapeutics [22] [23]. According to numerous studies, NPs have successfully been used as carriers for a variety of chemotherapeutic drugs (e.g. etoposide, paclitaxel, carboplatin, doxorubicin etc.), creating nanoparticulate systems which are extremely effective against a wide diversity of cancer types (Figure 2) [24] [25] [26] [27] [28] [29].

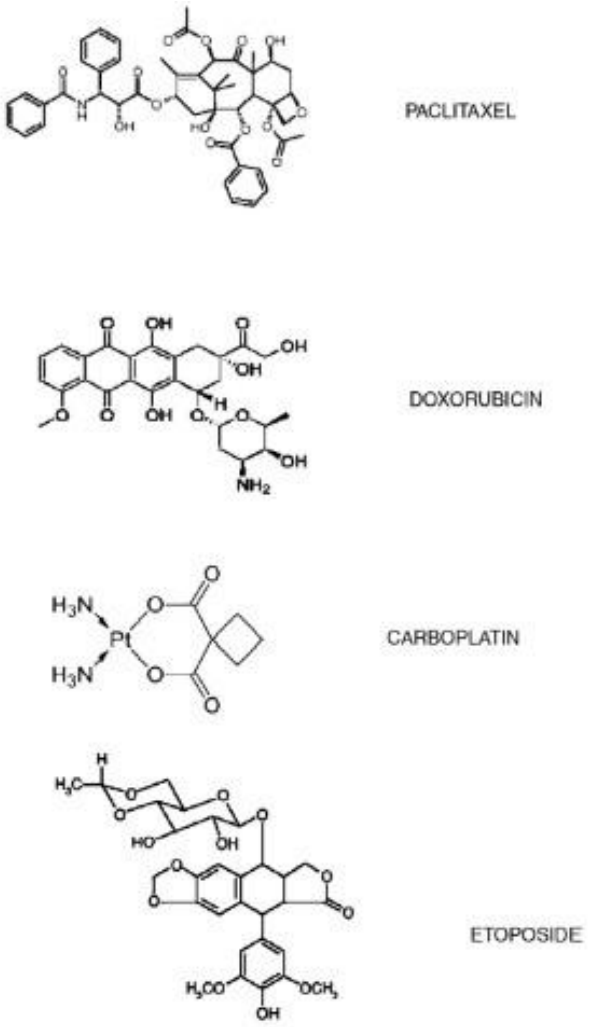

Figure 2: Chemical structure of therapeutic drugs that can be encapsulated into NPs. [29]

Multipurpose NPs that contain surface functionalized biomolecules are also developed in order to serve as perspective therapeutic agents, targeted gene silencing agents. Scientific and research society is intrigued by functionalized NPs due to their therapeutic exciting prospects as antimicrobial agents as well [29]] [30] [31]. Table 1 highlights some of the NPs that can be effectively used for therapeutics.

Table 1: NPs as therapeutic agents [29]

Type of nanomaterial	Encapsulant	Indicator	Therapeutic improvement
Polyisohexylcyanoacrylate NPs	DOX	Hepato-cellular Carcinoma	Higher antitumor efficacy than native doxorubicin and can overcome multiple drug resistance phenotype
PLGA NPs	Paclitaxel	Various cancers	Effective in chemotherapeutic and photothermal destruction of cancer cells
Gold NPs (AuNPs)	-	Various cancers	Effective as radiation sensitizers for cancer therapy
Chitosan NP (CNP)	siRNA	Ovarian cancer	Increased selective intratumoral delivery and significant inhibition of tumor growth compared to controls
Cetyl alcohol/polysorbate NPs	Paclitaxel	Brain tumor	Higher brain and tumor cell uptake, thus leading to greater cytotoxicity; also effective towards p-glycoprotein expressing tumor cells.
Lipid nanocapsules	Etoposide	Glioma	Greater cytotoxicity. Can overcome p-glycoprotein dependent multidrug resistance.
P (4-vinylpyridine) particles	-	Antimicro-bial agent	These particles can be used to inhibit bacterial growth for various bacteria as biocolloids
Chitosan-alginate NPs	Carboplatin	Retinobla-stoma	Enhanced antiproliferative activity and cytotoxicity of NPs in comparison with native carboplatin
Poly (3-hydroxybutyrate-co-3-hydroxyoctanoate) NPs	DOX	Various cancers	Effective in selective delivery of anticancer drug to the folate receptor-overexpressed cancer cells

Diagnostics

In order to sufficiently comprehend the biology and pathology of diseases, especially cancer at the molecular level, advanced analysis systems are required. The field of nanomaterials and nanotechnology combined with today's instrumental technology is considered to be able to satisfy all needs that arise from this emerging challenge [32] [33] [109]. The solutions offered by the use of nanotechnology and nanomaterials in the area of multiplex diagnostics are numerous with the added benefit of creating a perceptive, prompt and cost-effective base for advanced laboratory and diagnostic clinical environment. Utilization of NPs is constantly increasing in the discipline of molecular diagnostics and a large variety of tools are currently being developed. The most commonly used NPs so far are gold (Au) NPs and quantum dots (QDs) or similar to those types [29] [34] [35].

Semiconductor QDs are NPs with incomparable, stable fluorescence that can empower the recognition of more than several dozen tumor biomarkers in blood analysis or on malignancy tissue biopsies. They offer distinctive components that permit the identification of malignancy markers in natural examples at pg/mL focuses [35] [110]. Furthermore, molecular diagnostics has also managed to succeed major achievements ever since the advent of AuNPs, due to their high levels of sensitivity and specificity, multiplexing competence and short process cycle completion period required. AuNP-based colorometric analysis and Aptamer-conjugated AuNPs, show immense ability in bedside testing needs, especially for oncology patients. Their popular use as labels in diagnostics and detection is attributed to their one of a kind chemical and physical properties amalgamation, which permits biological molecules to be identified at low intensity [36] [37] [38] [110].

Even more, according to the up-to–date worldwide research database, a broad range of other nanotechnological devices for manipulation at a nano-scale, as well as nano-biosensors, are showing encouraging outcomes and are considered for the use of clinical applications [39] [40]. Specialists are facing the immense challenge to develop straightforward, quick, effective and easy to understand identification techniques for the recognition of disease cells in general, and cancer cell in particular. Cancer is an incapacitating disease and early and precise detection can make a vast difference not only in the patients' chances of complete therapy but also in improving their quality of life as well. Therefore, a large number of NP types in order to meet and address the demands of effective diagnostics is currently being developed. Such examples are shown in Table 2 [41] [42] [43] [44].

Table 2: NPs as diagnostic agents [29]

Type of nanomaterial	Diagnostic strategy	Advantages
AuNPs	The selectivity and specific affinity of aptamers is combined with spectroscopic advantages of AuNPs to detect diseased cells	For sensitive detection of cancer cells. Can easily differentiate between different types of target and control cells based on the aptamer
Magnetofluorescent particle systems	These bimodal contrast agents allows detection of cancer cells	Noninvasive diagnosis of breast cancer
AuNPs	Identification is based on the reaction of cell surface proteins with specific antibodies conjugated with AuNPs	Rapid identification and quantification of tumor cells
Semiconductor fluorescent QDs	These fluorescent biomarkers are analyzed by their resulting fluorescence and thus enables efficient cancer diagnostics	Enables fast and precise cancer diagnostics
Semiconductor QDs	Intense stable fluorescence enables the detection of cancer biomarkers	Useful for molecular diagnostics of cancer
Aptamer conjugated NPs	Aptamer-conjugated magnetic NPs can be used for selective targeting cell extraction and aptamerconjugated fluorescent NPs can be used for sensitive cancer detection	Enables the collection and detection of multiple cancer cells
Fluorescent europium(III)-chelate-doped NP	Highly fluorescent europium(III) with high affinity monoclonal antibodies coated on label particles and microtitration wells provides a sensitive immunoassay	Has potential in sensitive screening of viral analytes

Imaging

The advancement of an efficient transporter framework does not just mean the execution of transportation, but the successful affirmation of the site-particular distribution of the medication. For that reason, the power to trace and project the pathway of any nanomedicine from the systemic to the subcellular level becomes a necessity [45]. NPs can be effectively exploited to enhance the efficacy of fluorescent markers for medicinal imaging and health related investigated purposes. Even though different fluorescent markers are broadly employed as a part of in vitro and in vivo diagnostic applications, existing methods display a variety of weaknesses, for example, the prerequisite of color coordinated lasers, fluorescence fading and absence of oppressive limit of numerous dyes, and so on. Fluorescent NPs can productively triumph over these tribulations and provide important advancement towards commercial clinical application in the imaging of tumors and disease in general [46].

A lately discovered type of engineered optical probes, called fluorescent silica NPs (FSNPs), which is silica NPs enriched with fluorescent dye, have also been proven immensely useful in cancer imaging [47] [48]. The utilization of water-solvent functionalized QDs, which are profoundly steady against oxidation for natural and biomedical applications, is at me moment one of the quickest developing fields of nanotechnology. QDs display secure fluorescent assets, and at the same time exhibit new possibilities for in vivo imaging and diagnostic techniques in live cells [49]. Magnetic iron oxide NPs, have also gathered scientific interest as innovative contrast agents for biomedical imaging due to their capacity of deep-tissue imaging while considered as noninvasiveness and low toxicity techniques [50] [51].

Another modern technology showing promising potential in the attempt of effective imaging and therapeutic invertions in cancer patients is the use of dynamic magnetomotion of magnetic NPs (MNPs) detected with magnetomotive optical coherence tomography (MM-OCT) [52] [53]. AuNPs are also widely in use for cellular imaging [54] [55]. In today's bibliography and research database it is made fairly clear that a variety of nanoparticulate system types can be abundantly utilized as in vitro and in vivo imaging agents for proficient diagnostics and therapeutics [29] [56] [57] [58].

1.1.2 Advantages of NPs as drug delivery systems

NPs are defined as microscopic, colloidal elements, with their size varying from 10 – 1000 nm in diameter [59] [60]. Different kinds of NPs can be employed as medication conveyance frameworks and these can be devised from differing materials with distinctive designs, to function as a conceivable medication conveyance vehicle to treat a specific pathology. Pharmacological substances can be inserted into NPs by different techniques, for example, encapsulation, surface attachment or entrapment [61].

NPs, because of their small size, can productively enter crosswise over obstructions through small capilaries into singular cells, and therefore permitting effective medication amassing at the objective site. Hence, the undesirable symptoms and the poisonous qualities of the therapeutic agents is diminished and the restorative viability is enhanced [20] [62] [63]. Pharmaceutical biotechnology uses NPs to enhance the therapeutic ratio of medications and give answers for future delivery issues for modern and newly arrived categories of biotechnological products for example, recombinant proteins and oligonucleotides [64].

In all reality, NPs pave the way for the development of new therapeutic technologies and medication that will be able to be used successfully in all care settings but without exhibiting any of the poor bioavailability and instability properties of today's therapeutic agents. Table 3 summarizes some of the most obvious advantages of NPs. Since the diverse outcomes displayed by the use of NPs, the type of NPs used in the transportation of the active medicinal agents to the site of action can vary according to the cause or type of pathogenesis. Nevertheless, although NPs are widely used in drug delivery applications, their colloid constancy in such systems has almost gone unnoticed. To progress the stability of NPs, polymeric surfactants or other modifiers are frequently imbedded in particles, forming a layer that generates an effective repulsive force between NPs that prevents flocculation [65] [66].

Table 3: Advantages of nanoparticles [29]

Advantages of nanoparticles
Increase the aqueous solubility of the drug
Protect the drug from degradation
Produce a prolonged release of the drug
Improve the bioavailability of the drug
Provide a targeted delivery of the drug
Decrease the toxic side effects of the drug
Offer appropriate form for all routes of administration
Allow rapid-formulation development

1.2 Magnetic Nanoparticles (MNPs)

Magnetic nanoparticles, may consist of iron, nickel and/or cobalt, which exhibit magnetic properties [67] [68]. Magnetic properties of a material emerge from magnetic moments of single electrons due to their orbital motion around the nucleus of an atom and intrinsic spinning around their axes. Because of the thermal instability of magnetic moments that cause changes in direction, a number of magnetic nanoparticles display superparamagnetic properties which are described as the nonappearance of magnetic behavior when the magnetic field is not present [69]. In the case of the iron oxide maghemite (γ-Fe_2O_3), superparamagnetic properties are detected at sizes smaller than 15 nm [70].

Furthermore, magnetic nanoparticles of small sizes, containing iron oxides that demonstrate magnetic behavior only in the existence of a magnetic field are called superparamagnetic iron oxide nanoparticles (SPIONs). The use of SPIONs in biomedical applications is considered fundamental given that the everlasting magnetic behavior of magnetic particles within an organism would be unnecessary or even disparaging when the magnetic field is removed. For example, magnetically induced deformation of endosomes containing paramagnetic nanoparticles was shown by the transmission electron microscope (TEM) [71].

The most common magnetic nanoparticles used in targeted drug delivery methods are chemically iron oxides. Iron is an important metal for the majority of living organisms even humans (endogenic iron oxide nanoparticles have been traced in the human

hippocampus) [72] [73]. However, iron oxide due to the production of free oxygen and nitrogen based atoms (called reactive oxygen and nitrogen species or ROS and RNS respectively), can cause high levels of cellular cytotoxicity [74].Therefore, magnetic nanoparticles are primarily constructed by using core-shell methodology. According to Lodhia, Mandarano, Ferris, Eu & Cowell (2010) the magnetic foundation of iron oxide nanoparticles is compiled of magnetite (Fe_3O_4) and/or maghemite (γ-Fe_2O_3) while their exterior layer can be composed by organic compounds, including inorganic material (silica, oxides, metals carbon) as well as surfactants and synthetic or natural polymers [75]. There is a multipurpose significance of the type of the core – shell combination of magnetic NPs:

(i) shielding the magnetic core from oxidation,
(ii) defending the surface from damaged caused by chemical reactions,
(iii) evading aggregate and agglomerates configuration due to Van der Waals forces, hydrophobic reactions end products and magnetic attractions,
(iv) competence of the various therapeutics connection and intensification of the cellular uptake rate [76] [77].

Biocompatibility of magnetic nanoparticles is based on the type of their exterior coating (biodegradable, i.e. contains certain polymers, or non-biodegradable, i.e. contains materials such as silica). The size of the magnetic NPs is also important factor of their biocompatibility. The size of the outside layer establishes the overall size of the magnetic NPs, for instance inorganic material types coating is smaller in size (below 100 nm) while polymer types coating is almost always above average size wise (i.e. above 100 nm) [78] [79]. The type of the coating determines characteristics of the particle surface, such as hydrophilicity and surface charge [80].

The form of ferrofluids (magnetic liquids) are preferred for the use in biomedical applications for convenience reasons since their surface charge is interchangeable according to the surface groups' ionization or by penetration of charged species of a surrounding liquid medium onto the particle surface thus forming an external layer surrounding the particle. The potential difference between the surrounding liquid medium and the layer around the particle is called the zeta potential, which in scales higher than 30 mV, regardless whether they are of positive or negative charge, will prevent each other, stay separated and therefore form a stable ferrofluid [80].
Magnetic NPs can contribute to the accomplishments of cancer therapy as drug or gene delivery systems in a variety of ways. Foremost is the exhibited magnetic behavior by magnetic NPs as opposed to the nonmagnetic NPs, permits observation and numerical quantifications of their biodistribution by MRI, which makes possible the determination of the optimal dosing in cancer therapy. Moreover, targeted drug delivery at the tumor site by magnetic NPs offers a more sufficient cancer therapy treatment technique since certain hindrances such as restricted bloodstream penetration shown by a variety of therapeutic substances are now subsided. Finally, site selectivity of tumor reduction and therapy medicines is enhanced and reduced adverse effects, none or less invasive as well as less cost-effective therapies are made possible with the use of magnetically-guided nanoparticles [80].
The success of site targeting with the use of magnetic NPs in the oncology field is to augment antitumor efficacy and simultaneously diminish unwanted systemic damage of healthy tissues in the following manners [81]:

(i) passive targeting,
(ii) active targeting
(iii) targeting with an external magnetic field

Passive and active targeting can be achieved regardless of nanoparticles magnetic behavior. Passive targeting is referred to the extravasation of nanoparticles from the blood-stream into the tumor due to disorganized and leaky tumor vasculature [82]. Active targeting is associated with suitable ligands, primarily monoclonal antibodies and their fragments, tyrosine kinase inhibitors and aptamers. All these molecules are actively able to connect to NPs and aim at tumor markers [83]. According to Babincova & Babinec (2009) [81], ligands can target extracellular matrix, surface receptors on endothelial cells of tumor vessels or pericytes and tumor cell surface receptors. In contrary external magnetic targeting can only be achieved by using magnetic NPs. Even more, according to Prijic & Sersa (2011) [80], combination of the two above mentioned systems can result to the provision of dual - targeting where the magnetic field represents an initial targeting vector that deliberates magnetic NPs in the cancerous site followed by second level active targeting by means of ligands, bound onto the surface of magnetic nanoparticles that are specific for tumor cells.

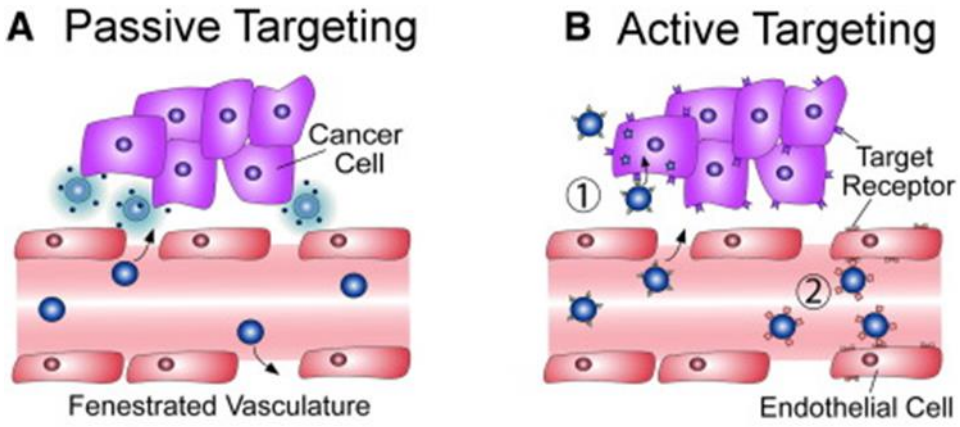

Figure 3: Diagrammatic representation of A. Passive and B. Active targeting in oncology. [83]

Magnetic nanoparticles are generally influenced by a magnetic field (Figure 4) which is created by high-field, high-gradient, rare earth magnets, such as neodymium iron boron (Nd-Fe-B) magnets. Nd-Fe-B magnets are the strongest type of permanent magnets which were commercially used during the late 1980s. The fundamental theory of magnetically-guided targeting is based on the placement of a magnet over a targeted site, i.e. a tumor, in order to in situ concentrate and/or retain magnetic nanoparticles [84].

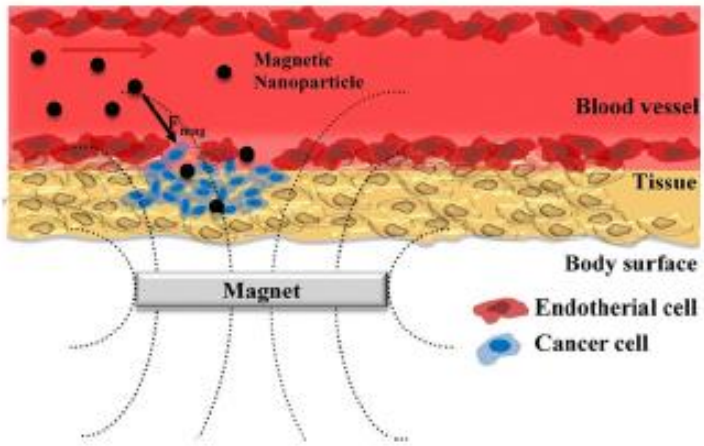

Figure 4: Schematic representation of a magnetic drug delivery system under the influence of external magnetic field. Fmag is the direction of the external magnetic field. [80]

If targeting with an external magnetic field occurs with the combination of a bare magnetic NPs with no loaded therapeutics, the cancer therapeutic method depends on the deliberate blockage of tumor vessels. The first attempt of such a therapeutic method was during the 1970s where blockage of tumor vessels for cancer therapy was carried out with the aid of magnetically guided microparticles composed of carbonyl iron. However this method showed very low in vivo stability as well as below average capability to be guided by the magnetic field [85].

Approximately 20 years later, magnetic NPs were used on animal subjects In vitro via intravenous route preceding the application of the magnetic field of flux density of 200-500 mT (application time = 20 min) above the subcutaneously transplanted colon carcinomas or hypernephromas, causing the overall and permanent tumor diminutions due to tumor blood vessels blockage [86]. Even more according to previously dated research, when active targeting is compared with antibody-bound magnetic NPs methods, results showed that targeting with bare magnetic NPs by suitably long exposure (application time = 6 h) to the magnetic field with a flux density of only 2.5 mT obtained significantly better results for in situ treatment especially in cardio and pneumonal types of cancer [65].

1.2.1 Biodistribution within an organism

As mentioned by Prijic & Sersa (2011) [80] biodistribution of magnetic nanoparticles is based on physicochemical properties they demonstrate, such as size, hydrophilicity and surface charge. Regardless whether nanoparticles possess magnetic behavior or not, an increase in their surface charge and a decrease in their hydrophilicity, the competence of plasma protein absorption is amplified, leading the phagocysitc cells to recognize them faster [87]. However, phagocytic cells recognize NPs with greater ease when renal clearance is omitted, causing their buildup in the liver, spleen and lymph nodes [88]. Different in vivo studies in mice and rats showed that magnetic nanoparticles after intravenous administration predominantly accumulated in the liver and spleen: 55% of the injected iron composing 190 nm magnetic nanoparticles localized in the liver after 6 h, but was reduced to 20% after 24 h. The level of iron in the spleen after 3 weeks corresponded to 25% of the injected dose [80]. Considerably

amplified levels of iron, although lower than these in the liver and spleen, were also identified in the heart and brain [88].

Biodistribution of magnetic NPs distributed through intraperitoneal route in mice yielded the same results obtained from the intravenous administration, with the largest concentrated amounts identified in the liver and the spleen [89]. When magnetic NPs are directed through a magnetic field, they are collected in the area of interest (Figure 5). For instance, when 70 nm magnetic NPs are intravenously or intraperitoneally administered into a mice (most effective route through the tail vein) and directed to the heart and kidneys by means of magnetic field with flux density of only 2.5 mT for 6 h, they are traced in cardiovascular, renal and pneumonal tissues. Biodistribution of magnetic nanoparticles after different administration routes is schematically presented in Figure 5 [80].

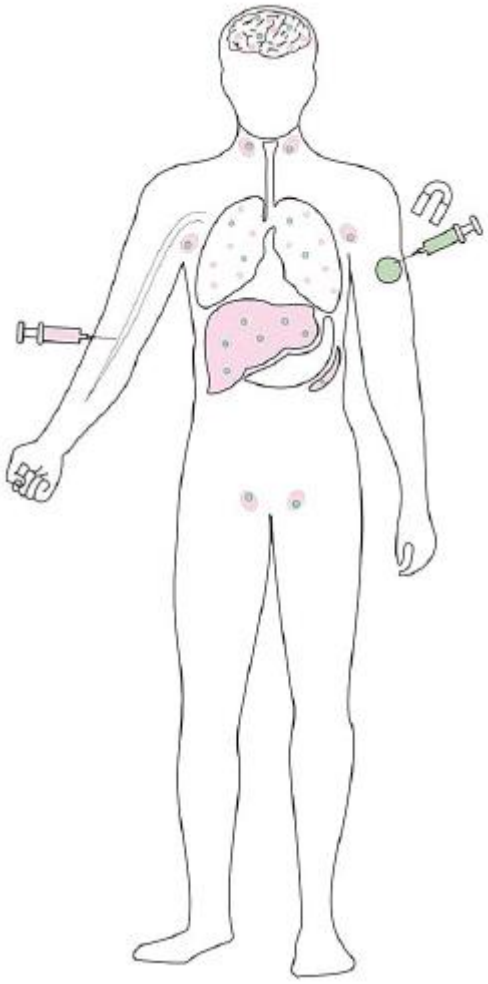

Figure 5: Biodistribution of magnetic nanoparticles within the body after different administration routes. After intravenous administration (pink syringe) magnetic nanoparticles predominantly accumulate in the liver, spleen and lymph nodes (pink areas). However, the blood flow also takes them to other organs, e.g. lungs, brain (pink dots). After intra-tumoral administration and exposure to the magnet (green syringe), magnetic nanoparticles concentrate in the tumor (green area). However, a small quantity can be also found in the organs throughout the body, e.g. liver, lungs, lymph nodes, brain, spleen (green dots), which depends on leakage of the tumoral vasculature. [80]

1.2.2 Toxicity studies

Toxicity of magnetic nanoparticles

Scientific research on the toxicity of magnetic nanoparticles is fairly limited. The pioneer tolerance study with carbohydrate coated magnetic NPs as possible delivery systems was executed in nude mice and showed no median lethal dose (LD), no modification in the blood haematological and biochemical qualities profiles as well as no organomegalies were observed after injection of magnetic nanoparticles. However, according to Kumar, Jena, Behera, Lockey, Mohapatra & Mohapatra (2010) [86] when 10-20% of the blood volume was permeated with the ferrofluid, brief periods of lassitude and resistance of food uptake were observed.

In a recent study Próspero et al., (2017) [90] mention that when tartrate and citrate-coated magnetic NPs were intraperitoneally administered in mice, an acute inflammation in the peritoneal cavity and around the spleen and kidney's helium were observed. This inflammation indicates that carboxylic acids intake at neutral pH and isotonic conditions, tartrate and citrate-coated magnetic NPs are not indicated for use a biocompatible ferrofluid. Prijic & Sersa (2011) [80] referring to the NIEHS Report on Health Effects from Exposure to Power-Line Frequency Electric and Magnetic Fields state that an external layer of dextran on the outer shell of magnetic NPs apart from an approximately 6 month period retention in the liver and spleen of mice caused no other pathologies and damages in the histological samples of these organs were identified. Same research concludes that histological investigation of liver, spleen and kidney following and intravenous administration of oleic acid-coated magnetic NPs, reveal no damages on any of the internal organs. However, lipid peroxidation indicating oxidative stress was over the normal rates but was gradually decreased to normal values within 3 weeks Prijic & Sersa (2011) [80].

Toxicity of an external magnetic field

There are still a lot of answered questions regarding the possible adverse effects of the utilization of electromagnetic fields for medical purposes. According to the research results of Wünsch-Filho et al., (2011) [91] there is a faint connection between magnetic field exposure (flux density as small as 0.0003 mT) and an amplified risk of childhood leukemia. Furthermore a large number of clinical and research trials using MRI examinations reveal that a static magnetic field of flux densities from 0.5 to 2 T cannot be considered harmful as no side effects are reported, making it ideal for patient use with easy compliance on their part [92] [93] [94].

Conversely, in equally numerous researches where ultra-high fields of flux densities of 4 T and 7 T were used, an apathetic and averting behavior was observed [95] [96] [97]. There are some conflicting reports about cell toxicity or unwanted side effects caused by magnetic field exposure which may be because of the cell type's subordinate mechanisms. It seems that cells deriving from mesenchymal descent are more vulnerable to the magnetic field exposure than other normal and malignant cells [80] [98] [99] [100] [101]. Obviously, so as to give confirmation that the magnetic field precisely does not cause any harmful symptoms there is an indispensable need to curry out extra in vitro and in vivo studies.

1.3 The plasma membrane and the lipid bilayer

The biological membrane or cell membrane is found in both eukaryotic and prokaryotic cells and functions as a barrier between the internal and external cell environment. In animal cells, the plasma membrane is found in the external cell layer whereas in plant is just below the cell wall [102].

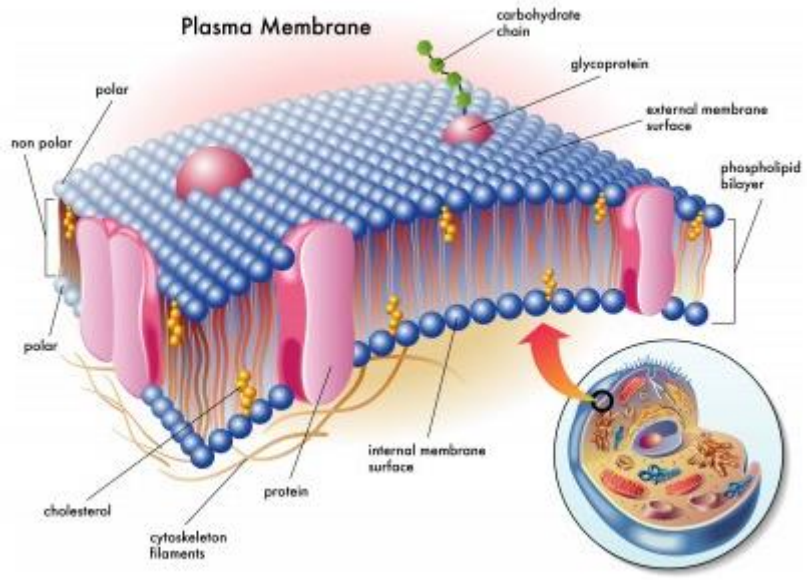

Figure 6: Structure of Plasma Membrane. [103]

The plasma membrane provides the stability of the cell structure and at the same time is keeping cell substances and organelles from spilling out; it is responsible for molecule transportation (ions, nutrients etc.) in and out of the cell and preserves the cell potential. Besides, the cell membrane fills in as a defensive boundary, which averts transport of undesired particles and pathogens into the cell. Molecular recognition mechanisms at the cell layer surface, which enable the cell to recognize a pathogen, likewise it assumes a vital part in cell signaling, and different types of cell-cell connections [102].

The key constituents of the plasma membrane include:

- Proteins like glycoprotein, responsible for cell recognition that also exhibit antigenic and receipting abilities.
- Proteins like glycolipids which connect to the phospholipids along with the saccharose chains.
- Lipids containing short carbohydrate chains connected on the extracellular layers of the membrane.
- Phospholipid Bilayer - which is made from phosphates and lipids, that crate a semi – permeable membrane, functioning as a selective barrier allowing certain types of substances to diffuse the cell membrane.
- Lipids such as cholesterol that provide the fluidity and flexibility of the cellular membrane. [102]

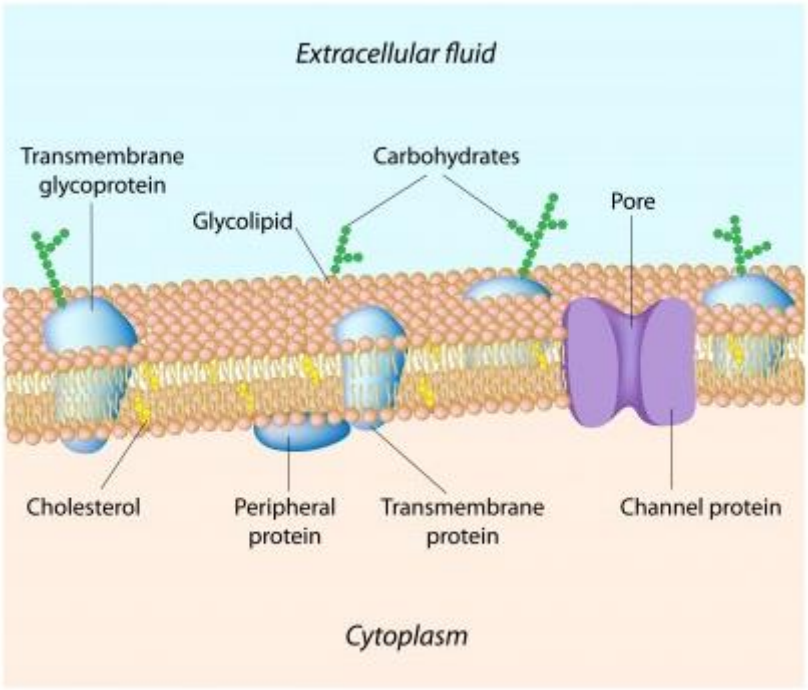

Figure 7: Components of Plasma Membrane. [103]

The lipid bilayer is found in all types of cell membranes. It plays an important role in the detention of the cell organization as its structural components present the barrier that indicates the borders of a cell. It is characterized as a lipid bilayer as it is arranged in two layers of lipid molecules and its typical size is approximately 5 nm thick and it is found in all cells types providing the cell membrane structure [104].

Although the actual cell membrane composition is far more complex, for membrane and membrane-proteins studying purposes it is often simplified and a replica structure of a bilayer consisting of one specific lipid (usually DOPC and DPPC) is employed [104]. A similar approach will be adopted here.

The structure of the lipid bilayer clarifies its function as a barrier. Lipids are fats (oil type molecules), that are impenetrable in water. There are two significant sections of a lipid that present the construction of the lipid bilayer. Each lipid molecule consists of a hydrophilic region, also called a polar head region, and a hydrophobic, or nonpolar tail region [104]. Figure 8 is a diagrammatic representation of a lipid.

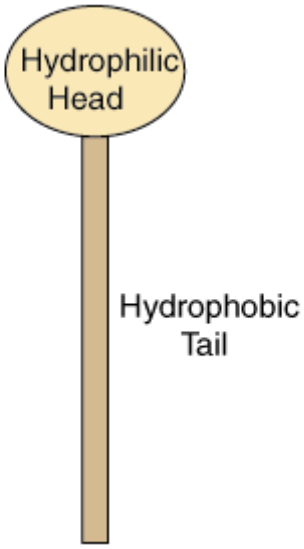

Figure 8: Basic Lipid Structure. [105]

The hydrophilic region (does not dissolve in water environment) is attracted to aqueous water conditions while the hydrophobic region (dissolves in water environment) is repelled from such conditions. A lipid molecule is termed an amphipathic molecule as it contains both polar and nonpolar regions [104]. The most recurrent class of lipid molecules identified in cell membranes is the phospholipid (figure 9). The phospholipid molecule's polar head region contains a phosphate group. It also has two nonpolar tails made from fatty acid chains, composed of chain of carbons and hydrogens and demonstrates a curve in one of the chains (because of its double-bond structure) [104].

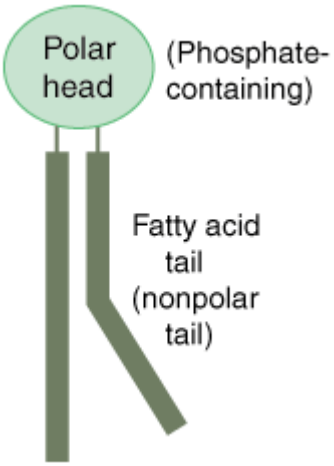

Figure 9: Phospholipid Structure. [105]

The phospholipids are organized in a bilayer scaffold like structure with their hydrophilic heads turned towards the aqueous external and internal environment of the cell, providing this way protection to the hydrophobic tails of the phospholipid structure. This is a spontaneous reaction, i.e. no energy expenditure required as it is a naturally occurring reaction. This structure provides the required cell limits between the internal and external cell environment [104].

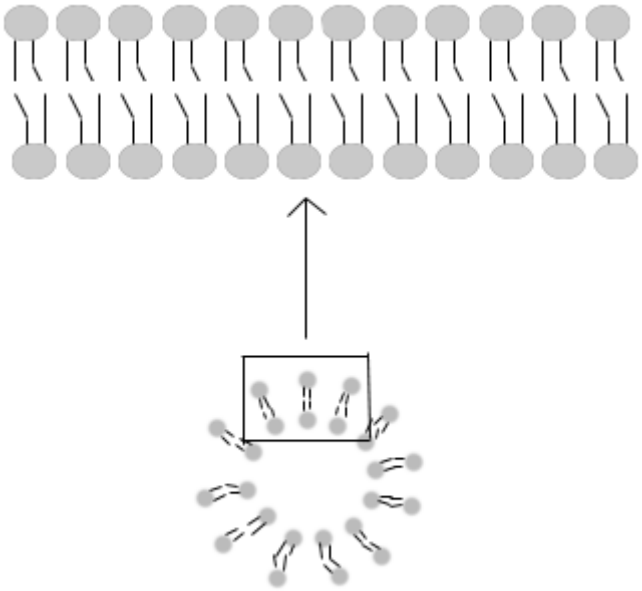

Figure 10: Lipid Bilayer. [105]

As we mentioned above the most crucial property of the lipid bilayer is its highly impermeable structure. Since molecules are prevented from freely entering and/or exiting the cell, the nature and size of the molecules to be transported in either direction is a key factor. Water and gasses are easily transferred through the lipid bilayer with none or very limited energy expenditure. However larger or small polar molecules are not permitted to freely cross the bilayer and subsequently the cell membrane, without the aid of other carrier molecules or structures [104].

Another important function of the lipid bilayer is its fluidity. The lipid bilayer contains lipid molecules and proteins. The fluidic nature of the bilayer allows the movement of the proteins within the lipid bilayer. This fluidity is biologically important, influencing membrane transport. Fluidity depends on the precise organization of the fatty acid chains and temperature (higher fluidity levels observed at lower temperatures). Structurally, the lipid bilayer is asymmetrical: the lipid and protein composition in each of the two layers is different [104].

1.4 Nanoparticle - membrane interactions

A large number of studies indicate that the manufacturing of nanomaterials that acquire maximal loading capacity, precise targeting, controlled release, and nominal toxicity qualities, demands a deep comprehension of the interface between nanomaterials and their host systems. As cells are the fundamental structures of all living organisms, they inevitably end up in the center of attention of the research regarding the interactions of living systems and nanomaterials. Traditionally examination of the nano-safety population has been centered on eukaryotic cells, and especially mammalian cells [106].

From a microscopic and physical aspect, the crossing point of NPs with the cell can be additionally analyzed to a range of detailed physical or chemical interactions at the

nano-bio interfaces, at the organelle or molecular level [107]. The interaction mechanisms could take account of VdW force, hydrogen bonding, electrostatic and chemical reactions. Characteristically the NPs used for biological applications have different sizes, forms, and chemical coatings for improved solubility and biocompatibility, and the biological environment the NPs target is immensely multifaceted, containing proteins, peptides, nucleic acids, and lipids, etc. [108]. When amalgamation occurs, the configuration of the biomolecules endures alterations due to the occurrence of the NPs, and the NP surface chemistry is promptly modified by the biomolecules and enzymes in the host systems (Figure 11).

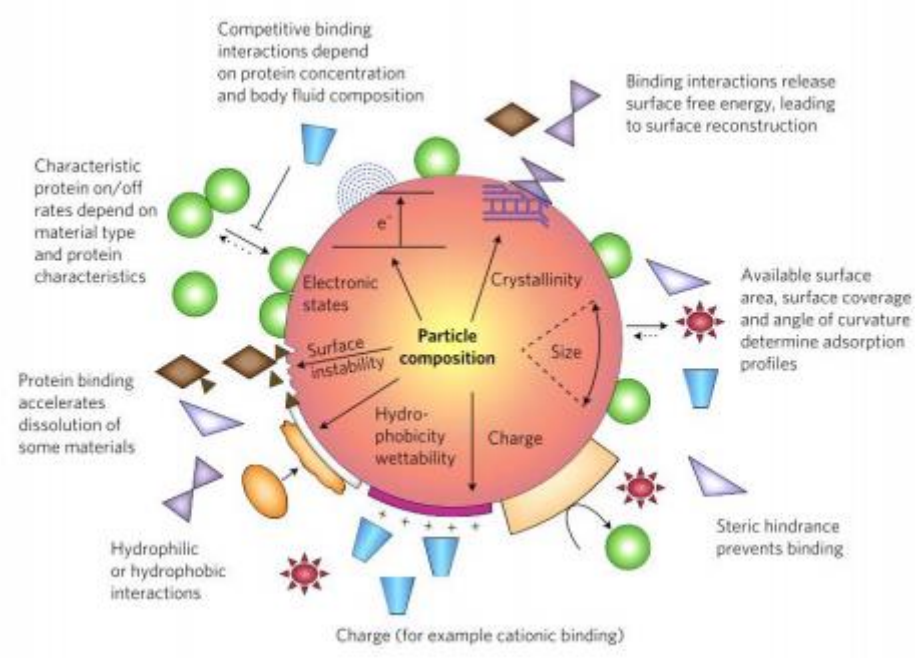

Figure 11: Biological molecules interacting with the surface of a NP. [106]

Additionally, the adaptable, heterogeneous and non-uniform cell membrane undergoes alternations to balance the energy exchange resulting from NP-lipid/protein interactions. If the NP is analogous to membrane lipid rafts in size, their exchanges could become greatly reliant on the precise binding position of the NPs. The unequally dispersed receptors and other membrane proteins also inconvenience the prediction and analysis of the interactions (Figure 12) [108]. The natural activities of the cell create a dynamic interaction, adding an additional aspect of intricacy to the interactions: active transporting of ions, proteins and other biomolecules; adenosine-5'- triphosphate (ATP) dependent endocytosis and exocytosis; cell skeleton protein polymerization; active NP transport, and processes after NP internalization, etc. [108].

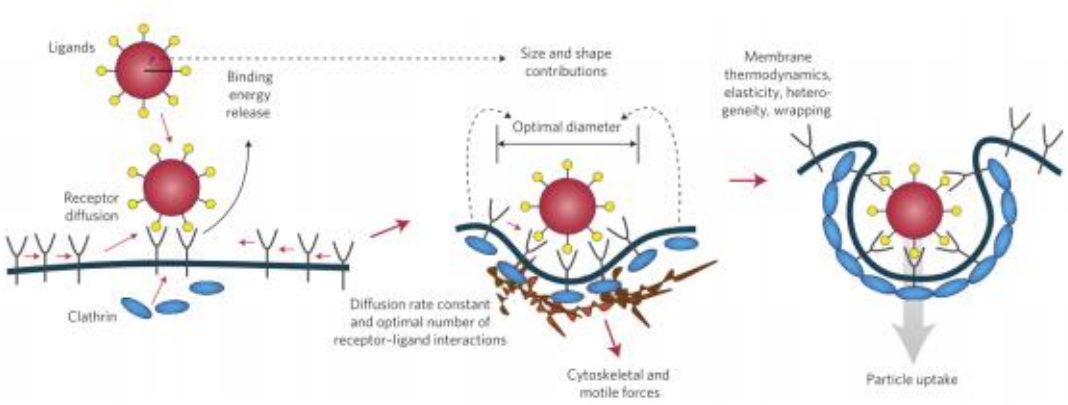

Figure 12: A coated NP interacting with a patch of non-uniform and dynamic cell membrane. [108]

1.5 Study Objectives

The aim of this study is to create tools that will aid us in determining the morphology of crystal nanoparticles and construct them for visualization and simulation in order to systematize how MNP surface attributes, including functional groups that affect their interaction with the cell membrane. In particular, we study two common functionalization groups, Polyvinyl alcohol (PVA) and polyarabic acid (ARA) molecules that are associated with the treatment of many types of cancer cells and especially for breast cancer. As nanotechnology is a relatively new field of scientific research, very little is currently known about the dynamics of the magnetite nanoparticles (MNPs) with cancer cell membranes and its contribution to therapy.

The study objectives can be categorized in the following:

Aim 1. Define the growing planes of the Fe_3O_4 crystal, which are dependent on the minimum surface energies. These planes can be used to extend the size and shape of the magnetite unit cell.

Aim 2. Use computational approaches for the construction and modeling of functionalized magnetite MNPs. Implementation of a script derives a Wulff crystal morphology of Fe_3O_4 using the lowest surface energies for each Miller index.

Aim 3. Develop a computational approach for computing the macroscopic morphology of any periodic crystal by forming different shapes based on Miller indices and the distance measure from a reference point (input parameters) and for visualizing the resulting crystal.

Aim 4. Define ligands attached to the Fe_3O_4 MNP core. Polyvinyl alcohol (PVA) and polyarabic acid (ARA) molecules are used. Also define the length of molecular chains and the number of ligands that can connect to specific Fe octahedral surface atoms.

Aim 5. Build a dipalmitoylphosphatidylcholine (DPPC) lipid bilayer and model the cell membrane.

Aim 6. Implement scripts for creating in a dynamic way the files needed for Molecular Dynamics simulation (for instance, topology and parameter files for the magnetite core and ligands).

Aim 7. Perform Molecular Dynamics (MD) simulations in vacuum and water to ensure the stability of our crystal morphology (cuboctaedron).

Aim 8. Place two model MNPs in the water phase of the lipid bilayer system and perform atomistic MD simulations in order to describe the nanoparticle-membrane interactions in atomic-level detail.

Aim 9. Compare the results from our simulations to available experimental data from our collaborators and derive conclusions from the distinct interactions between the different ligand coating of the NP and the membrane.

2. METHODS AND THEORY

This chapter presents the theoretical foundations of the present work. First, an introduction to Molecular Dynamics (MD) simulations theory is presented and the potential energy function used (force field). The roots of MD lie in statistical mechanics, an area of science, which aims to construct macroscopic properties of a system from basic information about intermolecular interactions. Next, an introduction of the principles of crystallographic techniques is presented, including crystal directions and planes. Finally, the information of the atomic structure of the magnetite is given, which is essential for the analysis of the computational approaches for the construction and modeling of functionalized magnetic nanoparticles (MNPs), presented in the next chapter.

2.1 Molecular Dynamics Simulations

2.1.1 Introduction

With technologically advanced computer systems, a variety of more complicated and more extensive life processes and phenomena may be observed and discovered using computer simulations and modelling compared to previous decades [111].

Molecular dynamics (MD) emerged as one of the principal simulation methods from the revolutionary applications to the dynamics of liquids by Alder and Wainwright and by Rahman in the late 1950s and early 1960s [195]. Because of the progressive advances in computer science and the progression of applied mathematics and algorithmic advances, MD has in turn grow to be an important contrivance in numerous areas in applied sciences such physics and chemistry. In the 1970s MD has entered dynamically the field of natural and life sciences and has since been used in order to scrutinize the structure and dynamics of macromolecules, such as proteins or nucleic acids [112].

MD is a computer simulation method, where the classical equations of motion of atoms or molecules are employed to estimate the time progression of the system. MD systems are employed to explain a multipart molecular system in the matter of a pragmatic atomic model, in an attempt to comprehend and predict macroscopic properties derived from meticulous information on an atomic scale [113].

MD simulations solve Newton's equations of motion for a system of N interacting atoms:

$$mi\frac{d^2ri}{dt^2} = Fi, \qquad i = 1, \dots, N \tag{2.1}$$

The forces are the negative derivatives of the potential function $V(r_1,r_2,r_3,\dots,r_N)$:

$$Fi = -\frac{\mathrm{dV}}{dri} \tag{2.2}$$

The equations are solved concurrently in small time steps. The system is followed for sometime, taking care that parameters such as the temperature and pressure sustain the required values and the coordinates are copied and logged into an output file at regular intervals. The coordinates in regards of time represent a trajectory of the system. After initial changes, the system usually comes to an equillibrium state. The average measures of the equilibrium trajectories for the majority of the macroscopic properties can derive from the output file [113]. This method is deterministic, especially in the cases where the space coordinates (position and velocity) of each atom are known, the state of the system can be predicted at any point, even in past and future states [114]. Molecular dynamics simulations can be prolonged and technologically demanding, none the less these methods are still faster and cheaper than conventional laboratory experimentation. Simulations of solvated proteins are premeditated up to the nanosecond time scale, however, simulations into the millisecond regime have been described [114].

In the present study classical MD simulations were used for the study of coated nanoparticles interacting with lipid bilayers that allowed for the simulation of these systems over time scales of nanoseconds and length scales of nanometers [115].

2.1.2 Setting up and running a Molecular Dynamics Simulation

The steps taken to setup and run a molecular dynamics simulation are presented in this section (Figure 13).

Initialization

To begin an MD simulation, an initial configuration of the system of interest is indispensable, i.e. a starting point, or t=0. In most cases, in biomolecular simulations, use of x-ray crystallography or NMR imaging will provide the require structure (today most structures yielded from these imaging techniques are stored in the Protein Databank and are easily obtained from there to be used as the initial structure). It is also likely a theoretical structure, developed by homology modeling, to be used. The initial configuration choice should be done with great care and consideration as it can interfere with the quality of the simulation [116].

Minimization

The minimization step removes any non-physical van der Waals interactions that may be present, which in any other case may result to local structural distortion and an unbalanced simulation. By using the force field that has been assigned to the atoms of the system, it is crucial to find a minimum on the potential energy surface so as to begin dynamics. At a minimum the net force on each atom vanishes [117]. Under periodic boundary conditions, there should be more than one minimum for a polymer, biopolymer, or a liquid. Hypothetically there might be a global minimum, but this will not likely be found without a conformational search [117].

In order to minimize a function (provided by the force field) an initial hypothesis or a set of coordinates is needed. The magnitude of the first derivative can be used to determine

the direction and magnitude of a step (i.e. change in the coordinates) required to approach a minimum configuration. The magnitude of the first derivative is also a meticulous approach to characterize convergence. A minimum has been congregated when the derivatives are close to zero [117]. To accomplish the minimum, the configuration must be sequentially updated by altering the coordinates (taking a step) and checking for convergence. Each full cycle of differentiation and stepping is termed minimization iteration. Naturally, a large number of minimization iterations are needed for large macromolecules to achieve convergence [117].

Three principal protocols for minimization are available:

- Steepest descent
- Newton-Raphson
- Conjugate gradient

The effectiveness of minimization can be determined by mutually taking into an account the amount of iterations necessary to converge as well as the amount of function evaluations required per iteration [118].

Steepest descent

The steepest descent method uses the first derivative to establish the direction towards the minimum. It is not exceptionally efficient since it must be used in combination of a line search in order to conclude on the step size. The line search utilizes the direction vector attained from the first derivative of the potential function to locate the optimal step size alongside this vector direction [118]. As soon as this restricted minimum alongside the direction of the derivative is established the step can be taken. The subsequent derivative will be orthogonal to the first. A line search demands numerous function evaluations, however, so as to establish the best possible step size. This procedure is robust and is used to minimize initially while the structure is not close to the minimum configuration [118].

Newton-Raphson and Conjugate gradient

More efficient minimization can be attained via the use of the conjugate gradients or the Newton-Raphson algorithms. The conjugate gradient technique makes use of information from preceding first derivatives to conclude the most optimal direction for a line search, whereas the Newton-Raphson method employs the second derivatives as well as the first ones in order to achieve the same result but in more accurate manner. Besides using the gradient information, Newton-Raphson also uses the curvature to foresee the point where on the gradient the function will be diverted into another direction. Storing and manipulating the second derivative matrix is prohibitive for large systems [118].

At this time, explicit water molecules are added for protein solvation to be achieved. If the procedure is starting from an x-ray crystal structure, then it is possible that a few water molecules already exist, although the amount present is not usually sufficient for solvation to occur. The solvating water molecules are typically acquired from a box of previously equilibrated water. The water box covers the total of the protein and any water molecules that overlap the protein are removed. At this point an additional energy

minimization should be carried out with the protein stabilized in its energy minimized position. This allows the water molecules to readjust to the protein molecule [118].

Heating the System

Initial velocities at a low temperature are assigned to each atom of the system and Newton's equations of motion are integrated to propagate the system in time. If an explicit solvent simulation is operating, first the protein positions are fixed and the water molecules move to adjust to the current protein configuration. Once the water molecules are equilibrated, the constraints on the protein can be detached and the whole system (protein-water) can evolve in time. During the heating phase, initial velocities are assigned at a low temperature and the simulation is initiated. Periodically, new velocities are assigned at a slightly higher temperature and the simulation is allowed to continue. This is repeated until the desired temperature is reached [119].

Equilibration

As soon as the preferred temperature is attained, the simulation of protein/water system carries on; for the duration of this stage numerous properties are monitored including the structure, the pressure, the temperature and the energy of the system. The purpose of the equilibration phase is to progress the simulation until these properties become stable with respect to time. If the temperature fluctuates notably, the velocities can be scaled in such way that the temperature returns close to its desired value [119].

Production phase

The last stage of the simulation is to run the simulation in the "production" phase for the appropriate time length. This can be from hundred ps to ns or more. During this phase, the thermodynamic parameters can be computed so the simulation correspond to one of the simulation ensembles [119].

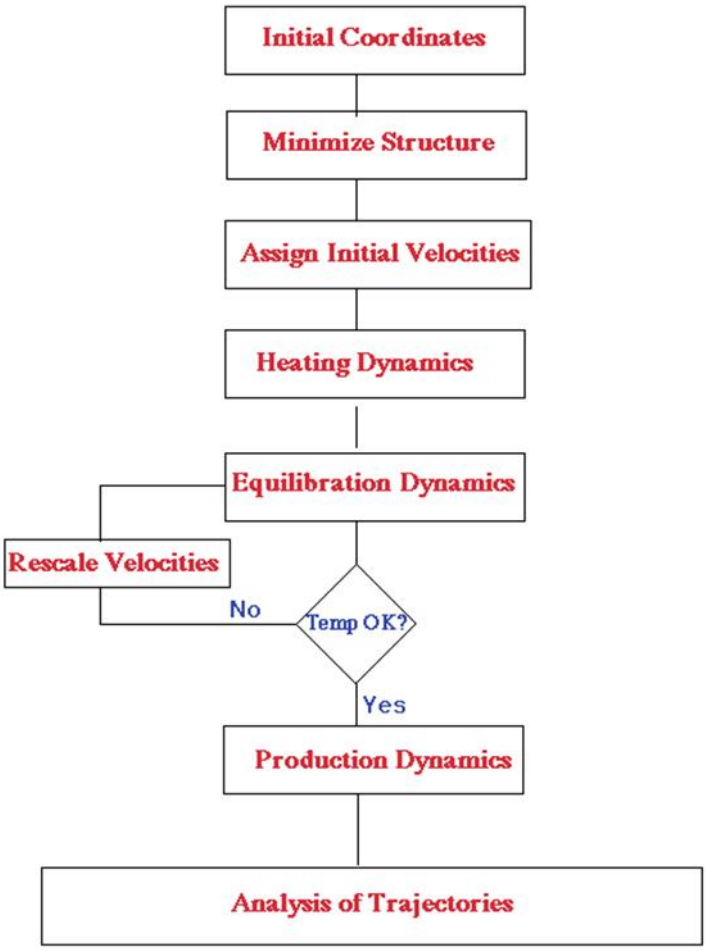

Figure 13: Simplified schematic of the molecular dynamics algorithm. [120]

2.1.3 Molecular Force Field

Force field is an equation scheme that illustrates the fundamental physical interactions in a molecular system. It symbolizes the total potential energy of a system made up from particles and can be explained by the total of intramolecular interactions, pairwise potentials, three-body potentials and so forth. The force field is normally separated into bonded and non-bonded interactions [121]. Non-bonded are the intermolecular van der Waals and Coulombic interactions, and frequently in molecular dynamics simulations, for the convenience of the computational efficiency, only pairwise potentials are taken into account [122]. Several force fields have been set up in such a way as their parameters will be able to embrace other numerous body effects, and consequently occasionally are referred to as effective pair potentials [122]. The bonded terms regroup simple covalent binding in addition to the complex hybridization and π-orbital effects; these are the bonds, angles, dihedrals and improper-dihedrals terms [113]. The potential energy, V(r), can be described as the total of the bonded and non-bonded energy terms in the system [123]:

$$V(r) = V_{bonded} + V_{non-bonded} \quad (2.3)$$

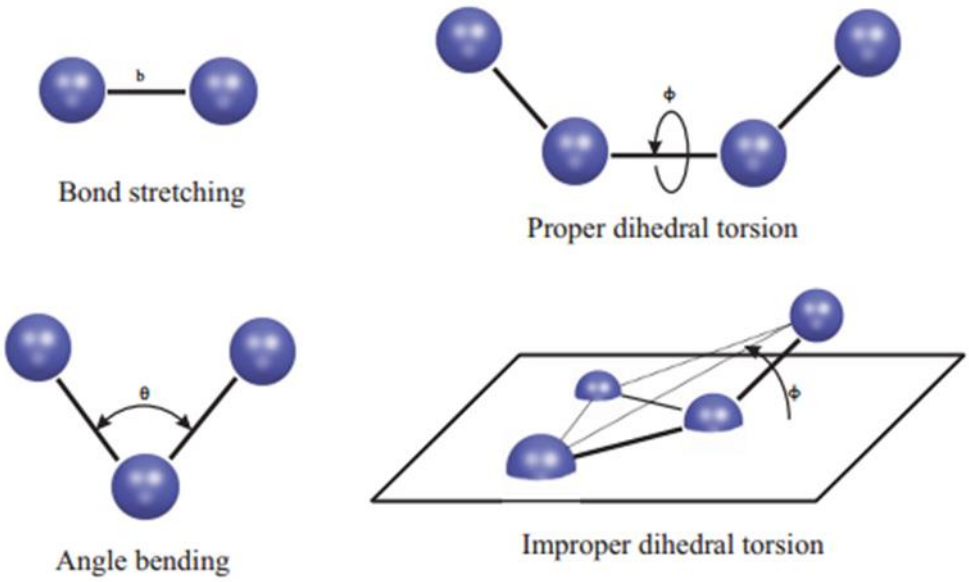

Figure 14: Schematic representation of the bonded interaction terms contributing to the force field: bond stretching, angle bending, proper and improper dihedrals. [113]

BONDED INTERACTIONS

The bonded terms describe simple covalent binding in addition to consideration of more complex hybridization. Simple harmonic terms depict bond stretching and angle bending. Rotation of singe bonds (torsions) is expressed by sinusoidal energies. The planarity of groups (e.g., the planarity of the double bond) can be imposed by harmonic potentials called improper torsions (as shown in figure 14) [124].

$$V_{bonded} = V_{bonds} + V_{angles} + V_{dihedrals} + V_{impropers} \quad (2.4)$$

Bond Stretching

The forces acting between atoms connected by covalent bonds are described as bond stretching. The potential is assumed to be harmonic:

$$V_b = k_b \, (\mathrm{b} - \mathrm{b}_0)^2 \quad (2.5)$$

where b is the distance between the two atoms. Each bonded interaction is characterized by two different parameters: b_0 the average distance between them and a force constant k_b. Values for force constants and bond lengths can be estimated from experimental data, for instance from high-resolution crystal structures, infrared stretching frequencies, theoretically from quantum chemical calculations or microwave spectroscopy data [124].

Angle Bending

The conformational change of the valence angles between three covalently bonded atoms is termed angle bending. The angle bending term is described using a harmonic potential:

$$V_\theta = k_\theta \, (\theta - \theta_0)^2 \tag{2.6}$$

where, θ is the angle between three atoms. Two parameters are used to describe each angle in the system: the reference angle θ_0 and a force constant k_θ. Vibrational motions involving angle bending generally happen at lower frequencies than those of usual bond vibrations and thus a lesser amount of energy is required to disfigure an angle from its equilibrium value than to stretch a bond. For that reason, the angle force constants are anticipated to be lower compared to the bond force constants [124].

Torsional Terms

The torsional terms are more weak than the bond stretching and angle bending terms. They depict the barriers to rotations which are present between four bonded atoms. There are two kinds of torsional terms: proper and improper dihedrals. Proper torsional potentials are described by a cosine function:

$$V_\varphi = k_\varphi[1 + \cos(n\varphi - \delta)], \quad n=1,2,3,4,6 \tag{2.7}$$

where φ is the angle between the planes formed by the first and the last three of the four atoms. Three parameters typify this interaction: δ sets the minimum energy angle, k_φ is a force constant and n is the periodicity.

The improper dihedral term is intended both to sustain chirality about a tetrahedral heavy atom and to preserve planarity about specific atoms. The potential is described by a harmonic function:

$$V_{\omega} = k_{\omega} \, (\omega - \omega_0)^2 \tag{2.8}$$

where ω is the angle between the plane formed by the central atom and two peripheral atoms and the plane formed by the peripheral atoms.

NON-BONDED INTERACTIONS

The input of non-bonded interactions has two constituents in the energy function, the van der Waals interaction energy and the electrostatic interaction energy:

$$V_{non-bonded} = V_{vdw} + V_{elec} \tag{2.9}$$

The calculation of these interactions is the most time-consuming part as they contain long-range interactions of the atoms in the system [119].

Van Der Waals Interactions

The van der Waals interaction connecting two atoms occurs from equilibrium between opposite (attraction) and same (repulsion) forces. Repulsion occurs at small spaces where the interaction between electrons is strong. Attraction, also called dispersion force, is observed as a result of vacillations in the charge distribution in the electron clouds. These fluctuations on a single atom or molecule create an immediate dipole which, sequentially, provokes a dipole in a second atom or molecule creating in turn an attractive interaction [125].

These effects have a zero measurement at infinite atomic separation *r* and turn into more noteworthy values while distance declines. Attraction forces exhibit linger range compare to the repulsive forces, however the more the distance is decreased the stronger the repulsive forces become. This gives rise to a minimum in the energy. Locating the atoms at the best possible distances ensures steadiness of the system. Equally the value of energy at the minimum *E** and the optimal separation of atoms *r** (which is approximately equivalent to the total of Van der Waals radii of the atoms) are subject to the chemical type of these atoms [126].

The interaction is described by the Lennard-Jones potential:

$$\mathrm{V_{VdW}} = 4\varepsilon \left[\left(\frac{\sigma}{r}\right)^{12} - \left(\frac{\sigma}{r}\right)^{6}\right] \tag{2.10}$$

where r is the distance between two atoms. The parameters σ: the collision parameter (the separation for which the energy is zero) and ε the depth of the potential well are influential for the equation. The Lennard-Jones potential model contains an attractive

part that varies with r^{-6} and a repulsive part that varies with r^{-12}. The Lennard-Jones potential is represented in Figure 15 [126].

With the intention of reducing the amount of interaction types and therefore the computation time, the Lennard-Jones potential is frequently abridged. This is completed by setting an appropriate cutoff distance and estimating the pair-wise interactions just for the atoms allocated within this distance. All van der Waals interactions of atoms past this cutoff are set to zero. A number of methods have been created for the truncation of the Lennard-Jones term [127, 128].

The first way available for the truncation of the Lennard-Jones term is to immediately set the potential to zero at the cutoff distance, which unfortunately creates discontinuities in the force at the cutoff distance. A substitute method is to move the sum total of the potential to higher values in order to achieve a zero value precisely at the cutoff distance, which in turn will lead to the manually-induced overestimation of the Lennard-Jones potential [127]. A third available method is to utilize an alternating function to taper the interaction potential over a predefined variety of distances. The potential adopts its standard value up to the first cutoff and is then switched to zero steadily between the first and the second cutoff. This model shows disadvantages due to the intense interaction forces in the switching region [128].

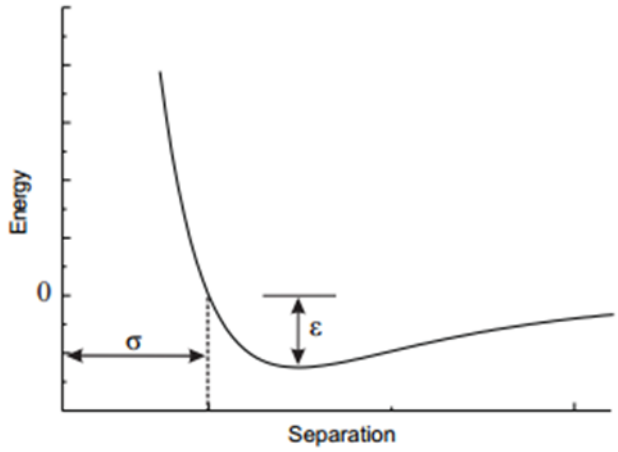

Figure 15: The Lennard-Jones potential. The collision parameter, σ, is shown along with the well depth, ε. [129]

Electrostatic Interactions

Electronegative elements show a preferential attraction to electrons rather than the less electronegative elements, which in turn creates an uneven charge dispersion in a molecule. This charge dispersion can be symbolized in a number of ways, with the most usual tactic being an assembly of fractional point charges all through the molecule. The charges are intended to replicate the electrostatic properties of the molecule and the ones confined to the nuclear centers are named partial atomic charges [130].

Coulomb's law describes the long distance electrostatic interaction between two atoms:

$$\mathrm{V_{Elec}} = \frac{q1q2}{4\pi\varepsilon_0 r_{12}} \tag{2.11}$$

where q1 and q2 are the charges of both atoms and r_{12} the distance between them. ε_0 is the electric susceptibility of vacuum [130].

Finally, the equation for the potential energy describing the force field can be written [121, 124]:

$$\begin{aligned} \mathrm{V} = & \sum_{bonds} k_B(b-b_0)^2 + \sum_{angles} k_\theta(\theta-\theta_0)^2 \\ & + \sum_{\substack{proper \\ dihedrals}} k_\varphi[1+\cos(n\varphi-\delta)] + \sum_{\substack{improper \\ dihedrals}} k_\omega(\omega-\omega_0)^2 \\ & + \sum_{\substack{i,j \\ i<j}} 4\varepsilon_{ij}\left[\left(\frac{\sigma_{ij}}{r_{ij}}\right)^{12} - \left(\frac{\sigma_{ij}}{r_{ij}}\right)^{6}\right] + \sum_{\substack{i,j \\ i<j}} \frac{qiqj}{4\pi\varepsilon_0 r_{ij}} \end{aligned} \tag{2.12}$$

2.1.4 Periodic boundary conditions

As a general rule, simulations are not meant to study separate (*in vacuo*) particles, instead they are meant to study the overall properties of a liquid or solid system. Specifically, as a result of the significance of water in association with the properties of biological macromolecules, these schemes are usually simulated in water/liquid solutions more willingly than in gaseous solutions [131]. Nonetheless, typical simulations can pursue only a restricted number of particles so as not to delay the computation. Consequently, under the given conditions the majority of the molecules would be allocated on or near the perimeters of the system, which in turn results to the observation of unrealistic surface effects [131].

To prevail over the predicament of surface effects, periodic boundary conditions (PBC) are regularly used. Standard biomolecular simulations utilize PBC to preclude unrealistic surface effects and imitate the properties of mass systems. In this method, the system is surrounded by its own duplications in all directions, to generate an infinite periodic lattice of identical cells. Only the *N* atoms, located within the central cell are regarded explicitly; however immediately after one of the atoms exits the cell, an image particle enters from the opposite side to replace it [131].

The nature of the interaction will determine if the system should network with its periodic replicas or not. As far as the short-range interaction is concerned, in case the potential range is not very long (the cutoff radius does not surpass half of the box), the Minimum Image Convention can be adopted in the calculation of short-range terms. In reality, in this condition it can be demonstrated that to ascertain the interaction contribution of particles i and j in the box just the nearest image of particle *j* to *i*, among the infinite periodic replicas, needs to be considered [132].

For simulations of macromolecules in solution, their interactions with their periodic images would be an artifact and should be avoided. Hence, a typical dependable guideline is to build a water box around the solute and the length of each box vector to exceed the length of the macromolecule toward that edge plus double the cutoff radius [132].

2.2 Crystallography

Crystallography is the scientific discipline that deals with the structure and the characteristics of the crystalline state. A crystallographer is a researcher in this scientific discipline who utilizes X-ray or neutron diffraction to build pictorial representations (or models) of a crystalline solid. Every single crystal in a crystalline solid is made out of a unique composition of atoms that is replicated, much like building blocks, all through the 3-D space, where the smallest repeating pattern is called unit cell or the asymmetric unit [133].

The symmetry of the repeating pattern in the crystal is described by the space group of the crystal, which is a way for depicting the arrangement of repeating patterns in a crystal utilizing an standardized notation system. Since X-ray structure establishment is so valuable, it is quite often an essential objective of a scientific research expert to acquire a crystal structure of each compound [133]. Crystallography has advanced radically during the last century. Ever since the configuration of the first crystal ($CuSO_4$), this scientific discipline has been employed for the observation of the structural characteristics of simple inorganic compounds in order to increase the understanding of basic inorganic principles [134].

2.2.1 Crystal structure

Crystal structures are assemblies of atoms possessing translational symmetry. With a specific end goal to depict the structure of a crystal, it is important to know the simplest repeating “motif” and the lengths and directions of the three vectors which together portray its repetition in space. They are expediently described regarding a lattice, an infinite periodic array of points in identical environments [133]. The identical points are called lattice points and an arrangement of atoms (structural pattern) with every lattice point describes the crystal structure. The unit cell is the simplest repeating unit of a crystal. It characterizes the parameters and directions that, when reoccurring in every one of the three dimensions, depict a crystalline solid. The unit cell requires six parameters to be characterized appropriately; three lengths (a, b, c) and three angles (α, β, γ). When lattice points are applied to unit cells, they might be situated differently to permit the characterization of various crystal systems [133].

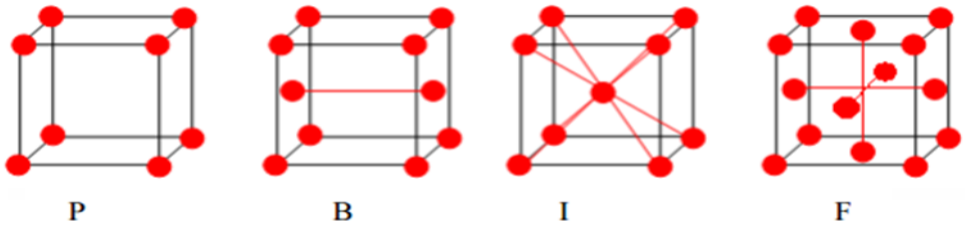

Figure 16: Possible lattice point positions. 'P' is representative of a primitive unit cell, 'B' is showing a lattice point centered on the (010) plane, or B-plane, 'I' is a body centered unit cell and 'F' shows a lattice point centered on all faces. [134]

All crystals might be depicted like subunits that display the same basic symmetry components as the crystal itself. There are seven diverse types of subunits related to the seven crystal systems (as shown in table 4).

Table 4: Seven crystal systems [134]

Crystal system	Lengths	Angles	Defining symmetry
Triclinic	a≠b≠c	α≠β≠γ	None
Monoclinic	a≠b≠c	α=β=90◦, γ≥90◦	Twofold axis or mirror plane or inverse twofold axes
Orthorhombic	a≠b≠c	α=β=γ=90◦	Three orthogonal twofold or inverse twofold axes
Tetragonal	a=b≠c	α=β=γ=90◦	One fourfold or inverse fourfold axes
Trigonal	a=b=c	α=β=γ≤120◦	One threefold or inverse threefold axes
Hexagonal	a=b≠c	α=β=90◦, γ=120◦	One sixfold or inverse sixfold axes
Cubic	a=b=c	α=β=γ=90◦	Four threefold axes

The seven crystal systems described in table 4 can be categorized further contingent on the symmetry components existing in the system. There are 32 diverse manners in which rotation axis, mirror planes, centers of symmetry and rotary inversion axes can be utilized to depict the 7 crystal systems. There are also fourteen particular space lattices refered to as the Bravais lattices which are framed by combination of the lattice and

crystal system. Table 5 demonstrates the simplest combinations which can be used to construct the Bravais lattices sections [135].

Table 5: 14 Bravais Lattice, seven primitive and seven non-primitive [133]

System	Bravais Lattice
Triclinic	P
Monoclinic	P,C
Orthorhombic	P,C,I,F
Tetragonal	P,I
Trigonal	P
Hexagonal	P
Cubic	P,I,F

A blending of the 32 point groups and the 14 Bravais lattices generates 230 unique three dimensional arrangements, called the space group. These 230 compositions are the main routes in which indistinguishable objects can be organized in a three dimensional space [135]. The 32 point groups were inferred without using translation elements of symmetry. A merge of the rotations and the parallel translations create screw axes, which in turn are designed by integers n and m, where n = 1, 2, 3, 4 or 6 and m < n, e.g. 3_1 demonstrates a triple screw axis with an interpretation between equivalent points 1/3 of a unit translation [135].

Merging mirror planes and translations creates a glide plane. Glide planes can be depicted by reffering to vectors a, b and c which characterize the unit cell edges. An α-glide, at a 90 degree angle to the b axis, for instance, consequences a reflection through the plane and translation by ½ α [135].

A space group is represent by a capital letter to identify the lattice form (P, C, F , and so forth) trailed by the point group symbols in which rotation and reflection symmetry is followed by the screw axes and glide planes. The impacts that symmetry has on a unit cell is typically referenced to an arbitrary point x, y, z. The components of symmetry for a particular point group produce a result on the point creating a series of equivalent positions [135].

2.2.2 Miller indices

Miller indices fashion a notation system in crystallography for planes in crystal (Bravais) lattices. Specifically, a category of lattice planes is concluded by three integers *h*, *k*, and *ℓ*, the so called *Miller indices* [136]. They are written (hkℓ), and indicate the category of planes orthogonal to $hb_1 + kb_2 + lb_3$, where bi is the basis of the reciprocal lattice vectors. (The plane is not constantly at a 90 degree angle to the linear arrangement of direct lattice vectors $ha_1 + ka_2 + la_3$, since the reciprocal lattice vectors do not require to be reciprocally orthogonal). By principle, negative integers are

symbolized with a bar. The integers are typically symbolized with lower terms, namely their greatest common divisor should be 1 [137].

There are also a number of associated notations:

- the notation {hkℓ} indicates the set of all planes that are comparable to (hkℓ) by the symmetry of the lattice [138].

As far as crystal directions (not planes) are concerned, the analogous notations are:

- [hkℓ], (notice the use of square brackets as opposed to the previously used round brackets), symbolizes a direction in the basis of the *direct* lattice vectors as an alternative of the reciprocal lattice; and
- in the same way, the notation ⟨hkℓ⟩ symbolizes the set of all directions that are equal to [hkℓ] by symmetry [139].

The Miller indices are described with regard to any alternative unit cell and not just with regard to primitive basis vectors [139].

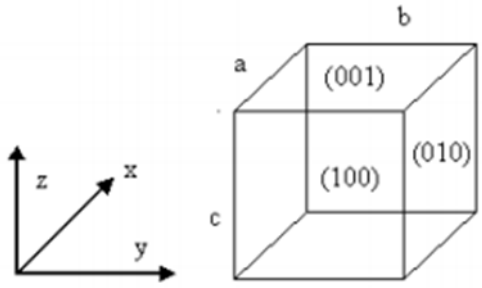

Figure 17: Indexing the three faces of a crystal or a unit cell. If an index is 0 the planes are parallel to the associated axes.

The direction of a surface or a crystal plane may be described by contemplating the way the plane (or in fact any parallel plane) interconnects the main crystallographic axes of the solid [139].

Let's consider a cubic crystal system and examine the procedure used to assign the Miller indices.

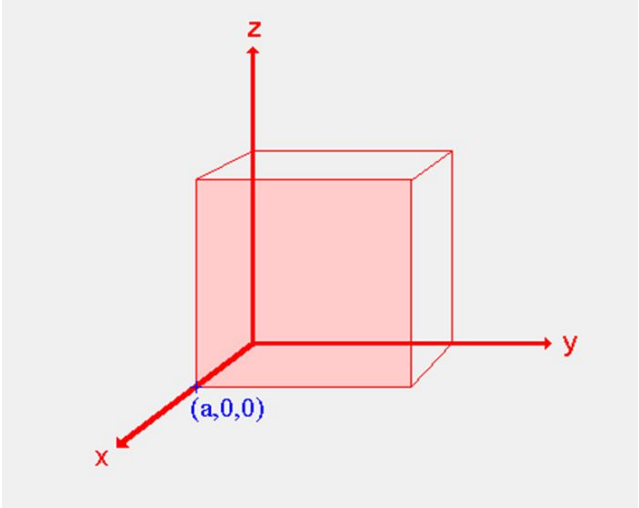

Figure 18: Example of defining miller indices for cubic unit cell. [140]

Phase 1 : *Identify the intercepts on the x- , y- and z- axes.*

In the present case the cutoff point (intercept) on the x-axis is at $x = a$ (at the point (a,0,0)), however the surface is parallel to the *y*- and *z*-axes - precisely consequently no cutoff point is observed in these two axes. Nevertheless we will accept the cutoff point to be at infinity (∞) for the particular case where the plane is parallel to an axis [139, 140, 141]. Therefore the intercepts on the *x*- , *y*- and *z*-axes are

Intercepts : ***a* , ∞ , ∞**

Phase 2 : Specification of the intercepts in fractional co-ordinates

Co-ordinates are adapted to fractional co-ordinates by dividing by the relevant cell-dimension - for instance, in a unit cell of dimensions a x b x c , a point (x,y,z) obtain fractional co-ordinates of (x/a , y/b , z/c). In the instance of a cubic unit cell all co-ordinates will merely be divided by the cubic cell constant , a [139, 140, 141]. This gives

Fractional Intercepts : ***a*/*a* , ∞/*a*, ∞/*a*** i.e. **1 , ∞ , ∞**

Phase 3 : Take the reciprocals of the fractional intercepts

This last exploitation produces the Miller Indices which (by principle) must then be identified without being divided by any commas or other symbols. The Miller Indices are also encircled in standard brackets (….) when we are trying to specify an exclusive surface just as it is shown here [139, 140, 141].

The reciprocals of 1 and ∞ are 1 and 0 respectively, thus yielding

Miller Indices : **(100)**

So the surface/plane illustrated is the (100) plane of the cubic crystal.

2.2.3 Crystallographic planes and directions

The crystallographic directions are conjured links connecting nodes (atoms, ions or molecules) of a crystal. Likewise, the crystallographic planes are conjured *planes* connecting nodes [141, 142]. A number of directions and planes have a larger compactness of nodes which can influence the behaviour of the crystal:

- Optical properties: in compact substance, the light is reflected from one atom to the other with the Rayleigh scattering; therefore the velocity of the light shows a large verification depending on the directions, the proximal distance (i.e. how close together or apart) are the atoms will determine the birefringence [150, 151].
- Adsorption and reactivity: the linkage of particles from a dissolved solid, liquid, or gas to a surface (adsorption) and the chemical reactions ensue on atoms or molecules, therefore adsorption and reactivity are greatly influenced by the node density [142, 143].
- surface tension: condensation of a material occurs when the atoms, ions or molecules are more steady especially when are encircled by other analogous species; therefore the density on the surface can affect the surface tension of an interface [142, 143]
    - the pores and crystallites have a tendency to comprise linear grain boundaries trailing dense planes
    - cleavage [142, 143]

- dislocations (plastic deformation)
    - the deformation core (usually referred to as the dislocation core) has a propensity to extend on dense planes (the elastic perturbation is "diluted"); this decreases the friction (known as the Peierls–Nabarro force), the sliding takes place more often on dense planes [142, 143];
    - the disturbance of motion, course, arrangement, or state of equilibrium (perturbation) resulting from the dislocation (Burgers vector) is along a dense direction: the modification of a single node in a dense direction is a smaller distortion [142, 143];
    - the dislocation line has a propensity to trail a dense direction, the dislocation line is frequently a straight line whereas a dislocation loop is usually a polygon [142, 143].

Considering the above influential factors, it is imperative to establish the planes and subsequently to have a notation system.

2.3 Magnetite Crystal Structure

Of all identified naturally existing minerals on Earth, magnetite is the one with most magnetic qualities as well as one of the most commonly used iron oxides [144]. Magnetite is regarded to obtain an inverse spinel crystal structure, represented by the general formula AB_2O_4. Nonetheless, a large number of latest experimental research results of magnetite are proposing that this is an superlative occurrence and to the contrary the structure is derived from a face–centred cubic array of oxide ions with A ions, in the case of magnetite Fe^{2+}, reside in octahedral holes and the B ions, Fe^{3+}, are similarly dispersed among octahedral and tetrahedral holes [144]. This crystal structure is represented in Figure 19.

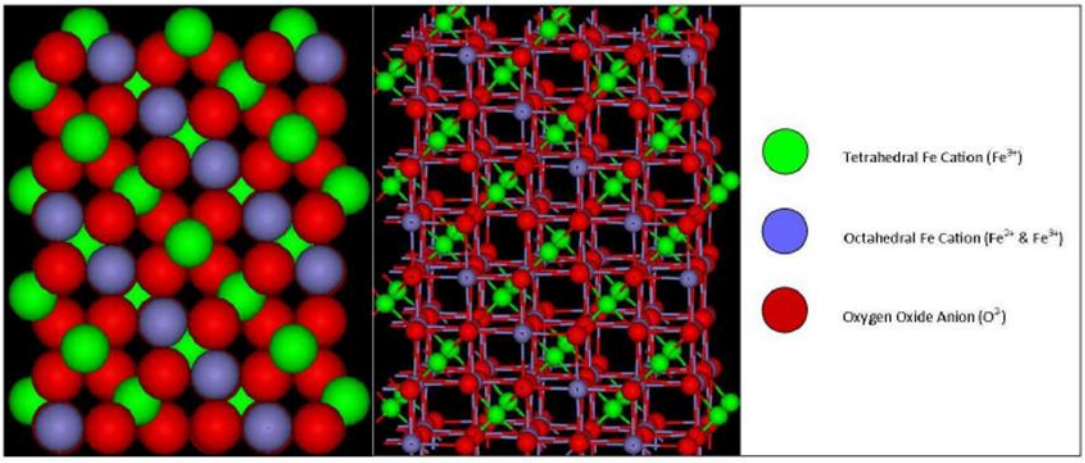

Figure 19: The inverse spinel crystal structure of magnetite. [145]

In magnetite, the Fe^{2+} and Fe^{3+} ions possess single spins, demonstrating several interesting magnetic properties. Fe^{3+} has a d5 electronic organization and five single electrons. The spins of the Fe^{3+} ions are nullified since half of the ions are located on octahedral sites and the other half are located on tetrahedral sites. As a result an antiparallel plane is observed which is formed by the spins of the Fe^{3+} ions in octahedral

and tetrahedral holes (caused by the spins of the ions on the octahedral sites interacting with the ones on the tetrahedral sites via the oxide ions). Even more no net magnetisation results from these ions. The Fe^{2+} ions retain a d6 electronic organization with four single electrons and are accountable for the net magnetisation. These divalent ions are inclined to line up their spins in a parallel manner with the ones of the trivalent ions in neighbouring octahedral holes. This configuration presents a net magnetic moment on the crystal. This all results to the magnetite being ferromagnetic (Figure 20), by which the magnetic moments of the atoms on diverse sublattices are contrasting, nevertheless, simultaneously the opposing moments are uneven and an unstructured magnetisation sustains [146]. Magnetite has been identified as interacting over hundred percent more powerfully with an external magnetic field compared to any other occurring mineral in nature [147]. Consequently, magnetite interrelates powerfully with the Earth's magnetic fields.

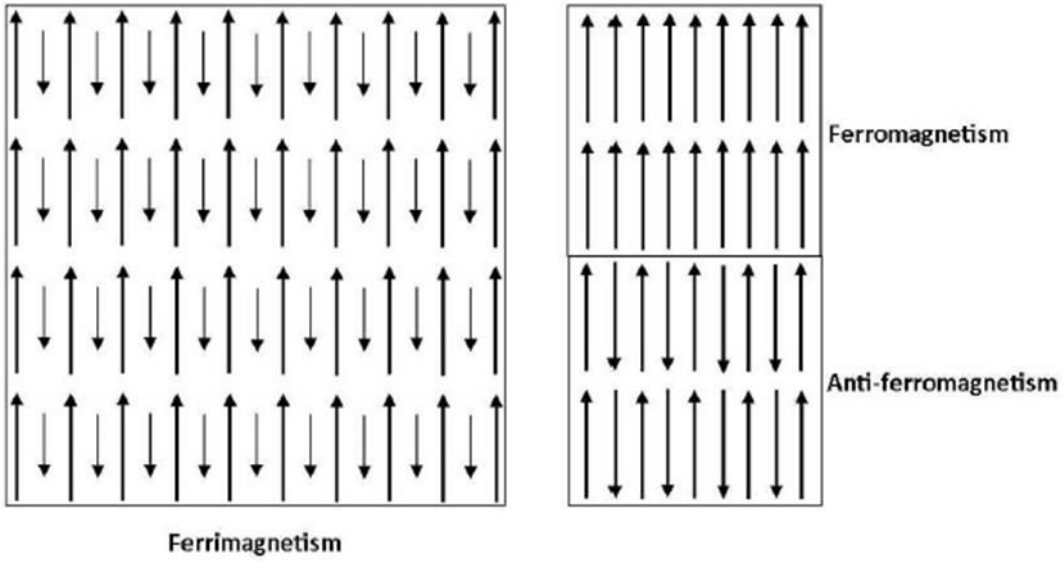

Figure 20: Ferrimagnetism; the magnetic moments of the atoms on different sublattices are opposed and unequal conferring a net magnetic moment. [145]

The unit cell of magnetite is made up from 56 atoms with unit cell parameters a=b=c=8.39 Å and its space group is the Fd-3m. [148]

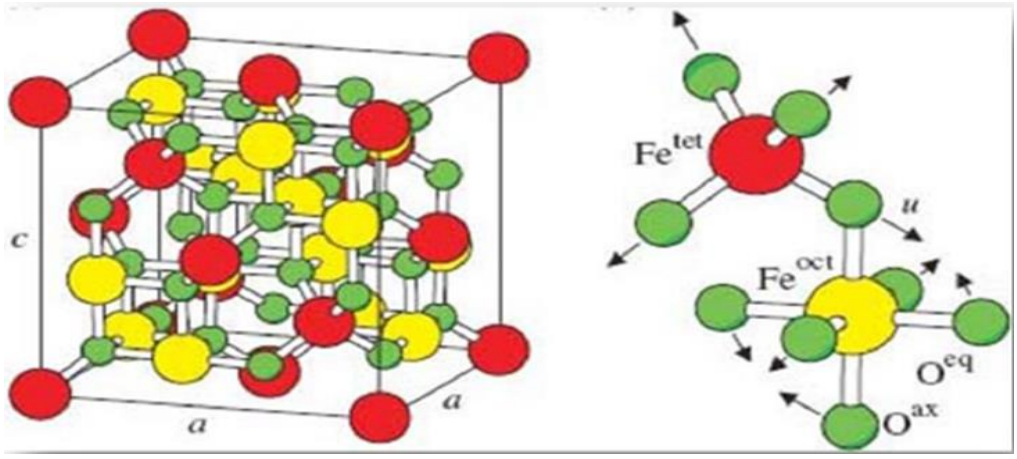

Figure 21: Unit cell of magnetite. [148]

In this research, the {100} and {111} magnetite surfaces were applied. The {111} surface can be terminated either by iron or oxygen. In this case in point, the iron terminated version was utilised as shown in Figure 22.

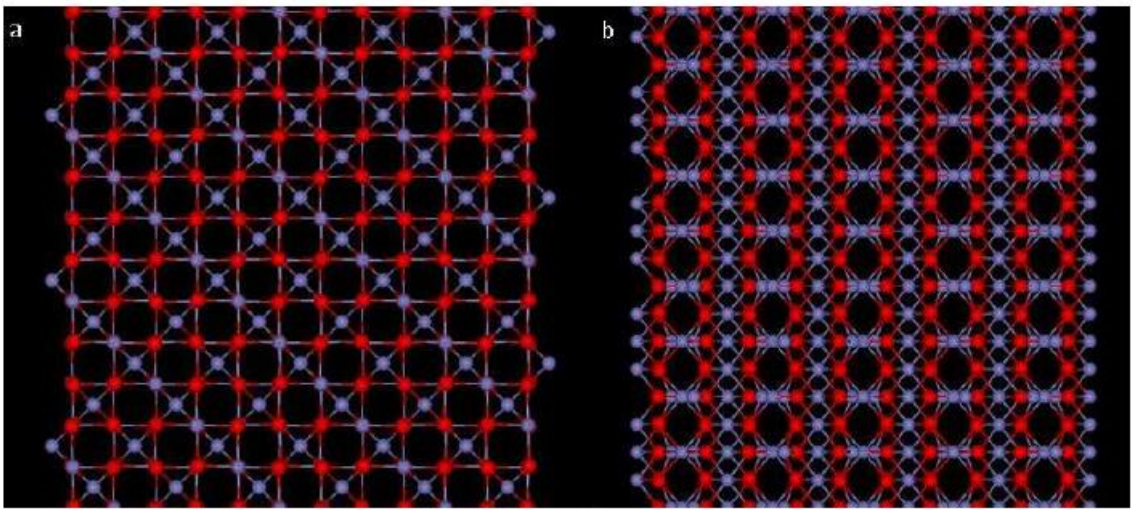

Figure 22: Magnetite surface types modelled in this work. a) {100} and b) {111} Fe terminated surface. [145]

Inorganic magnetite is typically identified in igneous and metamorphic rock, possessing an octahedral crystal habit, as shown in Figure 23. These crystals frequently contain lattice dislocations and other crystal defects, extensive size distributions, and the addition of impurities such as; Mg, Zn, Mn, Ni, Cr, Ti, V and Al. Nevertheless, as pointed out previously, magnetite is sustainable to biological mineralisation [145].

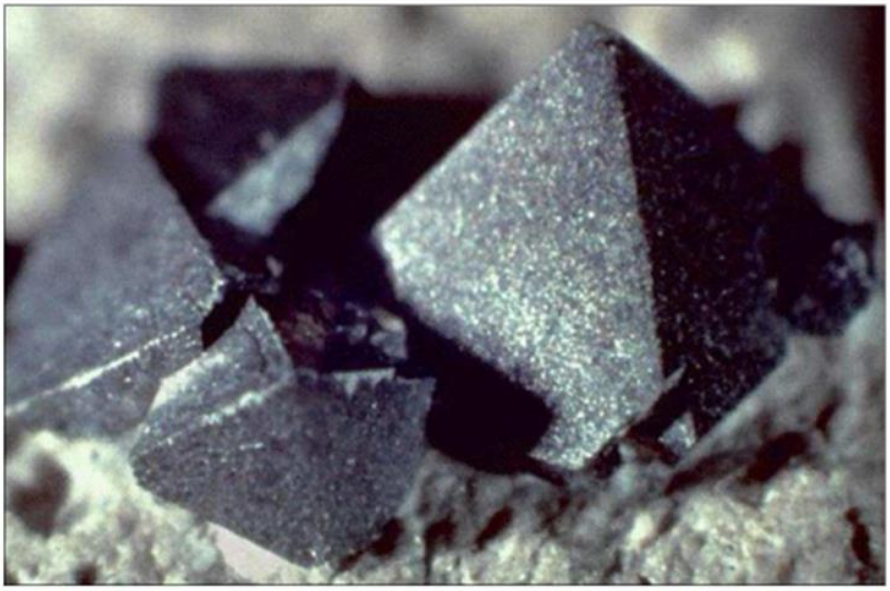

Figure 23: An example of inorganic magnetite. Note the octahedral crystal habit. [149]

3. RESULTS

This chapter presents the computational framework of the present work. There is a presentation of the tools developed during this study for the construction and modeling of magnetite nanoparticles (spherical or truncated MNPs) along with a general code implementation for the computing of the macroscopic morphology of any periodic crystal using its stable growing planes and the distance from a reference point. Additionally, information about the functionalization of the magnetite (two types of ligands attached to the magnetite core) is given as well as details about the construction of the lipid bilayer that is used to model the cell membrane. Next, we describe the dynamic way that the topology and parameter files for the magnetite core and ligands are developed. The chapter closes with a discussion on the simulation setup of the two model MNPs in the water phase of the lipid bilayer and our results.

3.1 Construction of spherical nanoparticles (Spherical Coordinates tool)

The “Spherical Coordinates tool”, which is a web-based tool, is implemented for the construction of spherical nanoparticles of a given radius. More specifically, our goal is to find the number and the Cartesian coordinates of smaller spheres that fit on the surface of the nanoparticle and visualize the output morphology.

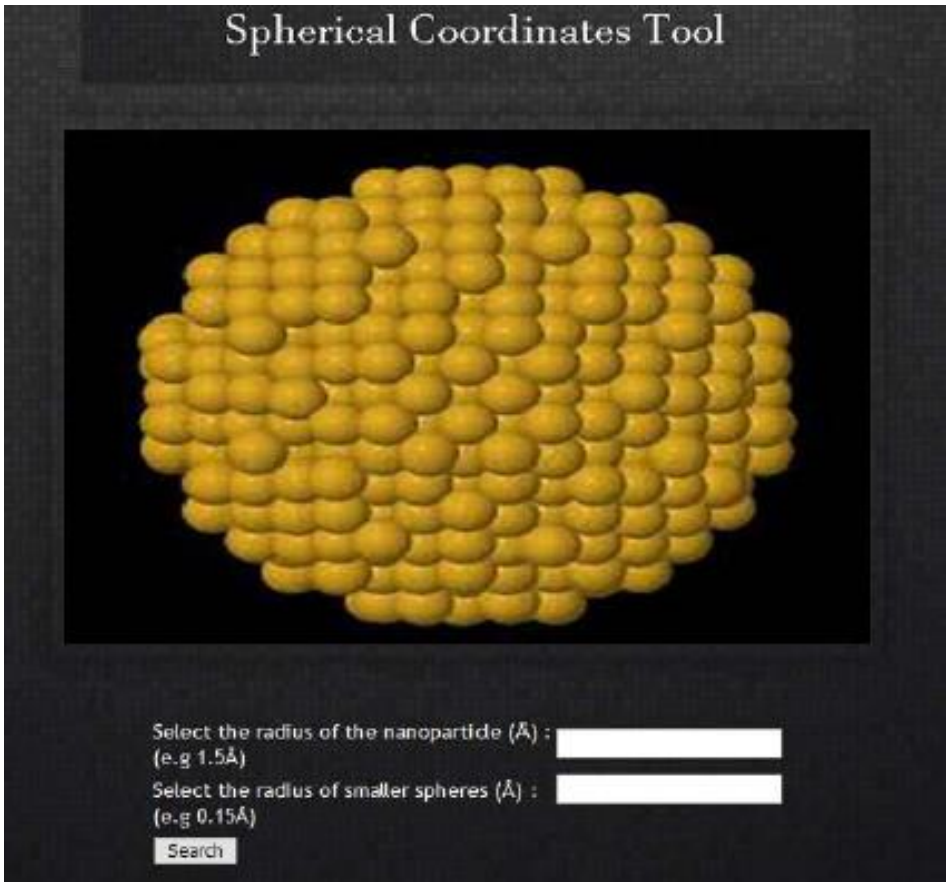

Figure 24: Home page of ‘Spherical Coordinates Tool’.

3.1.1 Program Use

The home page menu (Figure 24), allows two selections for the user:

i) the radius of the nanosphere (Å), and

ii) the radius of smaller spheres (Å), that will cover the surface of the nanoparticle.

The program computes the number of smaller spheres that fit on the bigger surface and the user can download their Cartesian coordinates (output format .xyz).

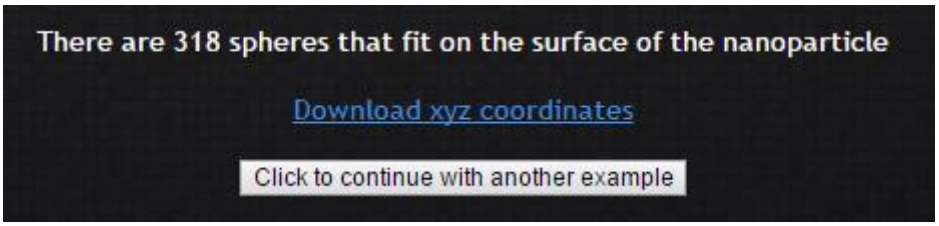

Figure 25: Home page output for 1.5Å and 0.15Å radius of the nanoparticle and the smaller spheres.

3.1.2 Methodology

Similar to a circle, i.e. a two-dimensional object, a sphere is characterized scientifically as the set of points that are all located a same distance r from a specified point, but in a three-dimensional space [150].

First of all, the volume of the nanoparticle and the smaller sphere is computed. In three dimensions, the volume inside a sphere is derived to be:

$$V = \frac{4}{3}\pi r^3 \tag{3.1}$$

In relation to the Kepler conjecture, which is a algebraic conjecture about sphere packing in three-dimensional Euclidean space, the cubic close packing (face-centered cubic) and hexagonal close packing arrangements demonstrate a larger average density compared to any other organization of uniformly magnitude spheres filling space [151]. The density of these arrangements is approximately 74.05%, (a percentage used in the present study for the computing of the number of smaller spheres packed at the surface of the bigger nanosphere).

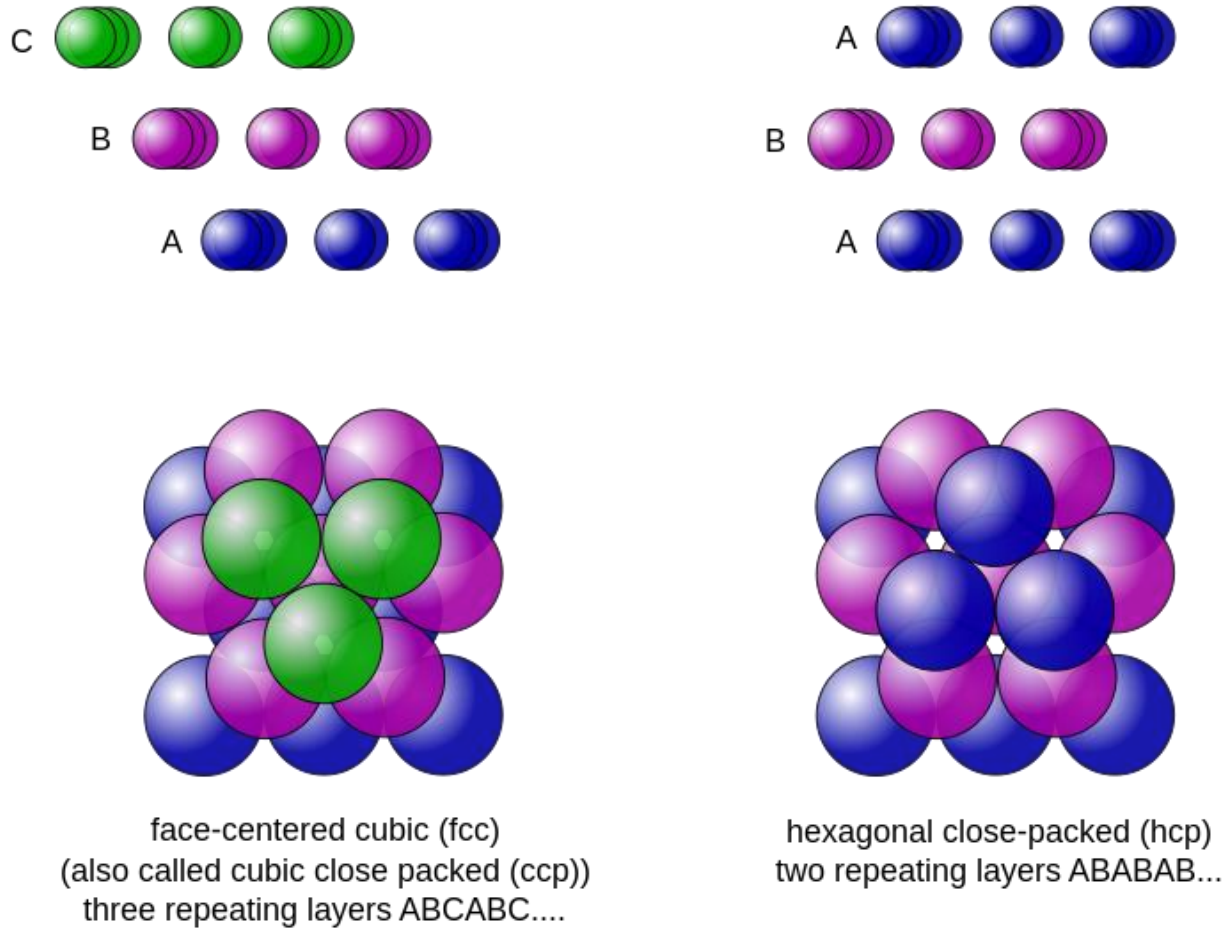

Figure 26: Diagrams of cubic close packing (left) and hexagonal close packing (right). [152]

In geometry, a sphere packing is a composition of non-overlapping spheres contained by a specific space. All the spheres regarded are typically of equal dimensions, and the space is generally three-dimensional Euclidean space. Still, sphere packing exertions can be oversimplified to be regard as unequal spheres, n-dimensional Euclidean space (regardless if the problem occurring refers to the circle packing in two dimensions, or the hypersphere packing in higher dimensions) or to non-Euclidean spaces such as hyperbolic space [153].

A representative sphere packing problem is to locate a planning in which the spheres pack as much of the proportion of the space as possible. The percentage of space packed by the spheres is termed the density of the arrangement. As the local density of a packing in an unlimited space can diverge relying on the volume over which it is calculated, the difficulty is generally to expand the average or asymptotic density, calculated over a large enough volume [153].

For equivalent spheres in three dimensions the most tightly packing takes up about 74% of the volume. An arbitrary packing of equivalent spheres normally has a density around 64%.

Subsequently, two functions are implemented for the computing of smaller spheres' Cartesian coordinates.

Function circle

That function computes the Cartesian coordinates of the spheres that fit at the circumference of the bigger sphere.

```
function function_circle($radius_nanoparticle,$radius_small_spheres,$z)
{
    global $number_of_small_spheres;
    $length=2*pi()*$radius_nanoparticle;
    global $number_one;
    $number_one=round($length/(2*$radius_small_spheres));
    $angle=0.00;
    $angle_increment=(2*pi())/$number_one;
    global $number_two;

    $coordinates=array();
    $coordinates_inverse=array();
    $coordinates_x=array();
    $coordinates_y=array();
    $coordinates_z=array();
    $coordinates_second_layer=array();

for ($i=1; $i<=$number_one; $i++)
{

    $number_two=$number_two+1;
    $x[$number_two]=$radius_nanoparticle*cos($angle);
    $y[$number_two]=$radius_nanoparticle*sin($angle);
    $angle=$angle+$angle_increment;
    $coordinates_x[$i]=number_format((float)$x[$number_two],8,'.','');
    $coordinates_y[$i]=number_format((float)$y[$number_two],8,'.','');
```

Figure 27: Function circle of 'Spherical Coordinates Tool'.

Given the radius of the nanoparticle, the circle circumference is computed (= pi* diameter = 2*pi*radius). Dividing the above with the smaller spheres diameter, the number of spheres that fit at the sphere circumference is computed. We also define an angle increment and polar coordinates are computed and converted to Cartesian coordinates (Equations in Figure 29(i)).

Function sphere

That function computes the Cartesian coordinates of the spheres that fit at the surface of the bigger sphere.

```
function function_sphere($radius_small_spheres, $radius_nanoparticle)
{
    global $number_one;
    global $number_two;
    $number_two=round($number_two);
    $number_three=round($number_one/(4.0));
    $angle = 0.0;
    $angle_increment = (0.5*pi())/$number_three;

  for ($i=1; $i<=$number_three+1; $i++)
  {

   $new_radius = $radius_nanoparticle*cos($angle);
   $new_z = $radius_nanoparticle*sin($angle);
   function_circle($new_radius, $radius_small_spheres,$new_z);
   $angle = $angle +  $angle_increment;

}

}
```

Figure 28: Function sphere of 'Spherical Coordinates tool'.

Similarly, a new angle increment is defined and the function circle is called with parameters such that the spherical coordinates can be computed (Figure 29(ii)) and converted again to Cartesian coordinates in each spherical quadrant.

Polar coordinates:

$$x = r\cos\theta,\ y = r\sin\theta$$

Spherical coordinates:

$$X(u,v) = R * \cos(u) * \cos(v)$$
$$Y(u,v) = R * \sin(u) * \cos(v)$$
$$Z(u,v) = R * \sin(v)$$

$-\pi \le u \le \pi$

$(-\pi/2) \le v \le (\pi/2)$

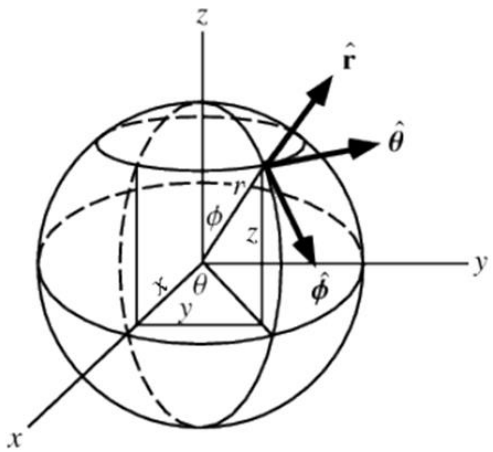

Figure 29: Equations of i) Polar coordinates and ii) Spherical coordinates.

3.1.3 Technologies used

The program code is implemented using PHP server-side scripting language, which is embedded into the HTML and CSS code. JQuery, a cross-platform JavaScript library, is also used. For local host of the webpage tool, the Wamp server is used.

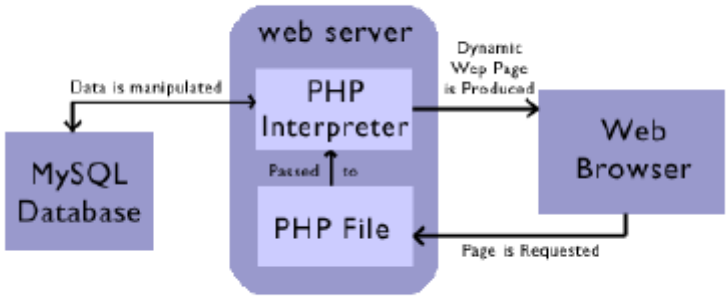

Figure 30: Technologies used for 'Spherical Coordinates tool'.

3.1.4 Results

Radius of the nanoparticle: 1.5 Å

Radius of smaller spheres: 0.15 Å

- There are 317 spheres that fit on the surface of the nanoparticle

Output visualization (.xyz file format):

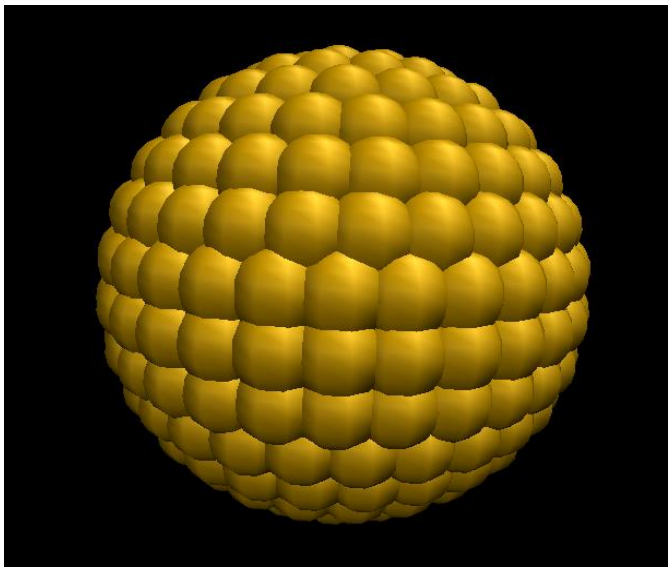

Figure 31: Output visualization of 'Spherical Coordinates tool', 1.5Å nanoparticle-0.15Å smaller spheres.

```
317

C   1.50000000  0.00000000  0.00000000
C   1.46929491  0.30194778  0.00000000
C   1.37843672  0.59153378  0.00000000
C   1.23114516  0.85690232  0.00000000
C   1.03345038  1.08718918  0.00000000
C   0.79344602  1.27296639  0.00000000
C   0.52095788  1.40662820  0.00000000
C   0.22714167  1.48270249  0.00000000
C   -0.07597375 1.49807476  0.00000000
C   -0.37597880 1.45211568  0.00000000
C   -0.66059123 1.34670681  0.00000000
C   -0.91815897 1.18616361  0.00000000
C   -1.13813718 0.97705872  0.00000000
C   -1.31151992 0.72795294  0.00000000
C   -1.43120888 0.44904468  0.00000000
C   -1.49230399 0.15175248  0.00000000
C   -1.49230399 -0.15175248 0.00000000
C   -1.43120888 -0.44904468 0.00000000
C   -1.31151992 -0.72795294 0.00000000
C   -1.13813718 -0.97705872 0.00000000
C   -0.91815897 -1.18616361 0.00000000
C   -0.66059123 -1.34670681 0.00000000
C   -0.37597880 -1.45211568 0.00000000
```

Figure 32: Sample of the xyz output file of 'Spherical Coordinates tool'.

Note that the equation $x^2+y^2+z^2=r^2$ is satisfied by the Cartesian coordinates of the smaller spheres that are packed at the surface of the bigger sphere.

Radius of the nanoparticle: 3 Å

Radius of smaller spheres: 1.5 Å

- There are 14 spheres that fit on the surface of the nanoparticle

Output visualization (.xyz file format):

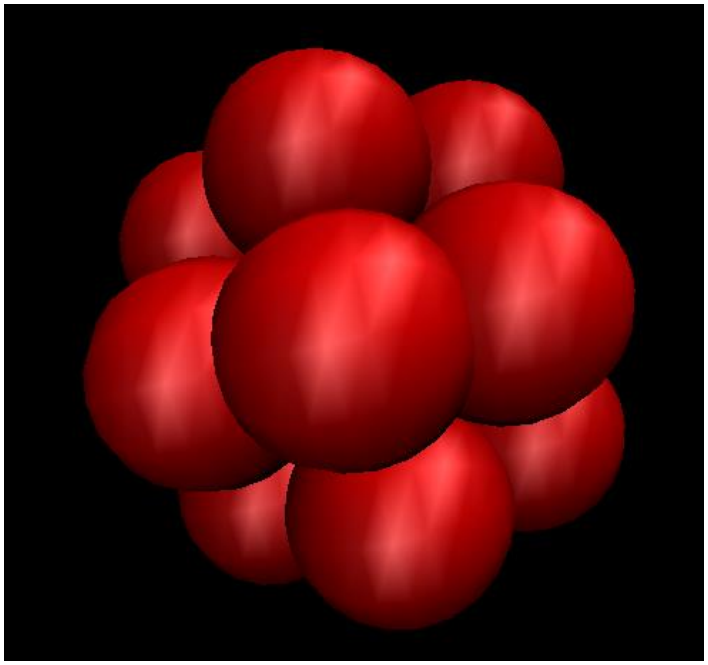

Figure 33: Output visualization of 'Spherical Coordinates tool', 3Å nanoparticle-1.5Å smaller spheres.

3.2 Construction of the magnetite nanoparticle (MNP) core

3.2.1 Magnetite unit cell

Crystallographically magnetite procures a cubic inverse spinel form. The oxygen ions form a close-packed cubic network with the iron ions situated at interstices among the oxygen ions. Two variations of interstices that the metal ions are able to form are identified, the tetrahedral (A) sites and the octahedral (B) sites (Figure 34) [154].

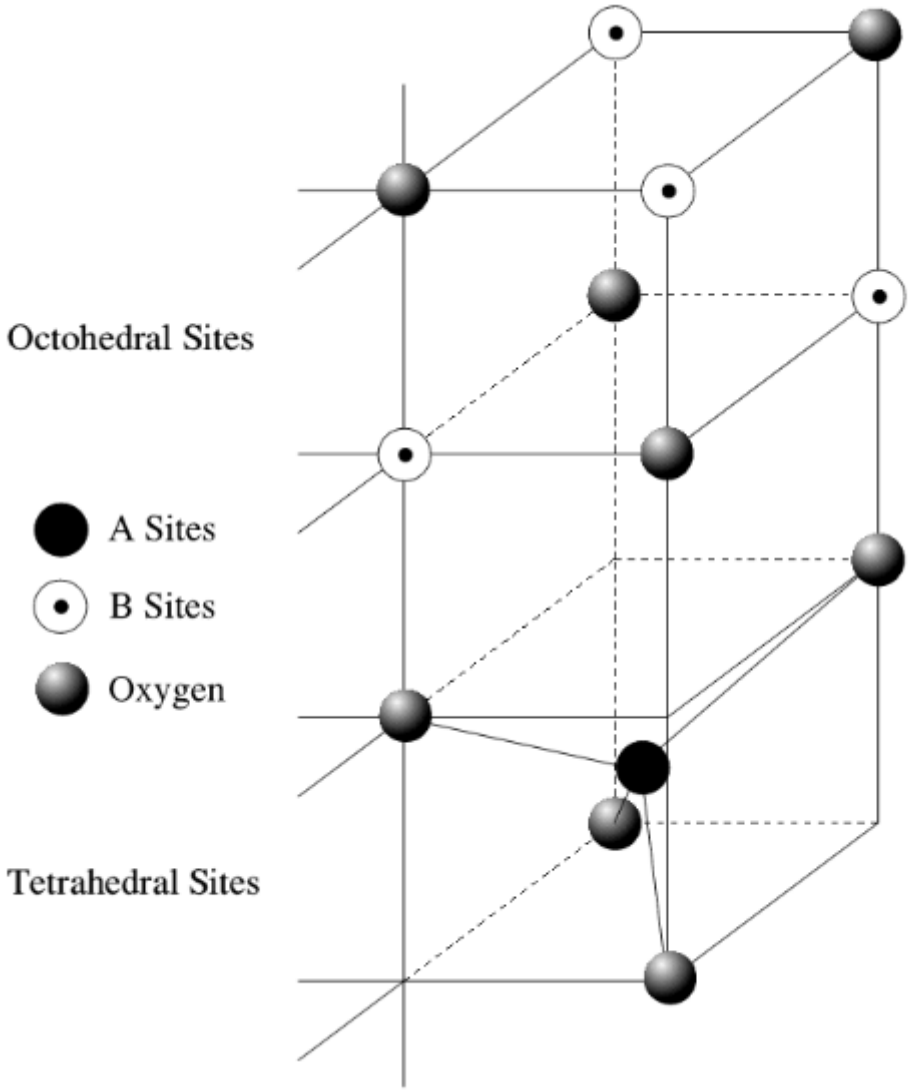

Figure 34: Diagram of the two different iron ion sites in magnetite. [155]

Higher than 120K A sites are occupied by Fe^{3+} ions only and the B sites by both Fe^{3+} and Fe^{2+} ions, with double the B sites occupied than A sites. At any given moment (in the scale of 1 nanosecond) the B sites are occupied by either a Fe^{3+} or a Fe^{2+} ion. This procedure of electrons transferring from one ion to the other is the reason that magnetite exhibits such a large conductivity at these temperatures, ~0.07 Wm at 800K [156].

When temperature decreases, at the point of the Verwey temperature (119K) an abrupt modification in behavior is observed. At temperatures of 120K and 119K a sudden ninety-fold drop in electrical conductivity is measured and it is related to an alteration of the crystal structure from cubic with lattice constant a_0=8.3963 Å, to a lower symmetry ordering, probably orthorhombic, with tetramolecular units a_0=5.912 Å, b_0=5.945 Å, c_0=8.388 Å (at 119K) [156].

The iron ions on the B sites divide into either Fe^{3+} or Fe^{2+} ions (as the thermal energy for electrons to move between ions is no longer adequate), therefore A sites with Fe^{3+} ions, B sites with Fe^{3+} ions and B sites with Fe^{2+} ions are now formed [154, 156].

In this study, the unit cell of the magnetite crystal is downloaded from the crystallography open database (http://www.crystallography.net/) with CIF number 1011032 [157] (Figure 35). It consists of 56 atoms with unit cell parameters a=b=c=8.39 Å and its space group is the Fd-3m.

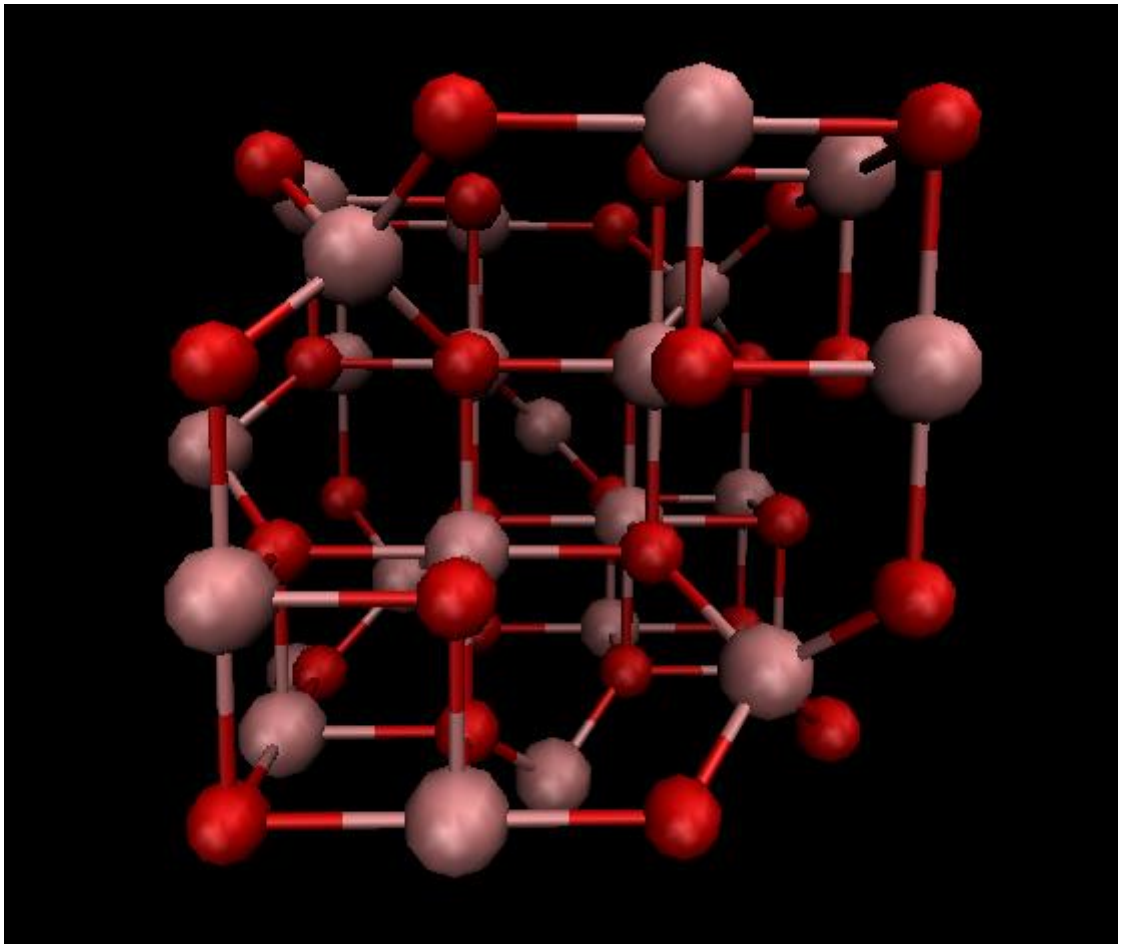

Figure 35: Unit cell of magnetite visualized in VMD.

3.2.2 Methodology

- Our objective is to build the magnetite core of the nanoparticle, with a diameter of 3nm deriving an appropriate shape for the nanoparticle.

The growing planes of the Fe_3O_4 crystal, which correspond to its minimum surface energies, can be used to extend the size and shape of the nanoparticle (NP). These planes are generated by calculations based on the density functional theory (DFT) that calculate the geometries and surface free energies of a number of surfaces at different compositions, including the stoichiometric plane, and those with a deficiency or excess of oxygen atoms [158]. The planes that dominate the magnetite morphology are the (001), followed by the (111) surface, which truncates the corners of the cube [158]. This method is followed and a Wulff crystal morphology [159], which represents the core of the Fe_3O_4 NP, is derived dynamically with our in-house implementation using the lowest surface energies for each Miller index.

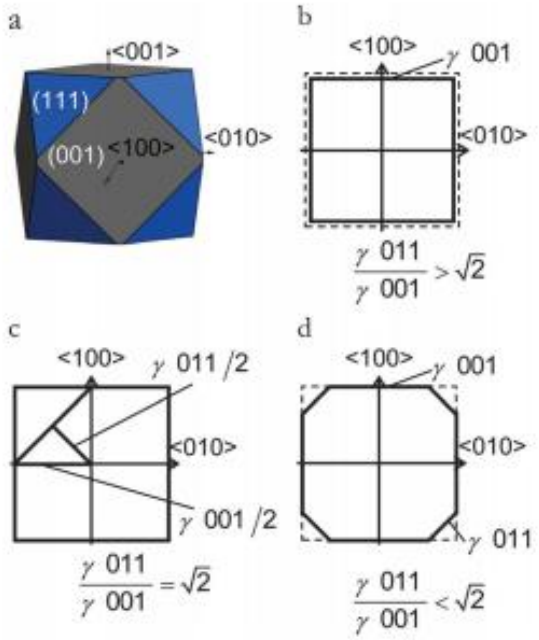

Figure 36: (a) Equilibrium morphology for a Fe_3O_4 crystal derived from a Wulff construction. (b–d) Schemes of the crystal cross-sectional planes along the <100> and <010> axes for different ratios of stabilities of the lateral surfaces, which illustrate why the (011) surface is absent in the equilibrium morphology. [158]

The first step, after visualizing the unit cell of the magnetite, is to replicate it three times in the xyz direction by using the buildCluster module of MAPS [160] so that the size of the replicated crystal to be 24 Å in each dimension (Figure 37b). Its calculated equilibrium morphology is then expressed as a cubic shape of 3-nm (30 Å) diameter with truncated corners (cuboctaedron) (Figure 37c) based on the geometric approach that follows.

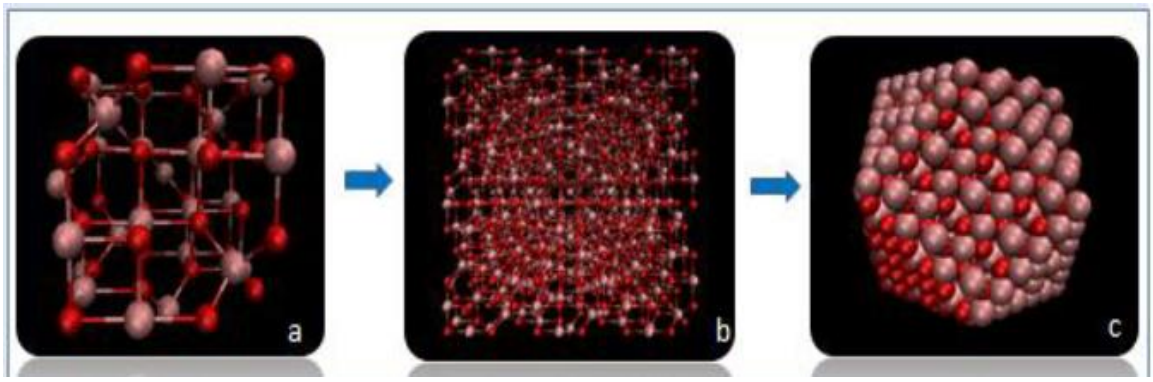

Figure 37: (a) The unit cell of magnetite that is used for the construction of a (b) crystal cluster. (c) The output structure from our code implementation (cuboctaedron), represents an appropriate morphology for magnetite nanoparticles based on stable growing surfaces of the magnetic crystal.

In geometry, a cuboctahedron is a polyhedron with 8 triangular faces and 6 square faces. A cuboctahedron has 12 identical vertices, with 2 triangles and 2 squares meeting at each, and 24 identical edges, each separating a triangle from a square.

The area A and the volume V of the cuboctahedron of edge length α are:

$$A = (6 + 2\sqrt{3})\alpha^2 \approx 9.4641016\,\alpha^2 \tag{3.2}$$

$$V = \frac{5}{3}\sqrt{2}\alpha^3 \approx 2.3570226\,\alpha^3 \tag{3.3}$$

As the derived crystal cluster is a cubic structure and the (001) plane represents the edges of the cube (including the symmetric planes) and the (111) truncates the corners (similarly including the symmetric planes), the equations of all planes have to be expressed and conditions to be formed so that the atoms that are inside the cuboctaedron to be included in the structure and the others to be excluded.

More specifically, the cubic dimensions are normalized such that the starting point is the (0,0,0) and each cubic edge has a length of 1 (Figure 38a). This is a normalization that is helpful for expressing general plane equations. At the end of the computing, the coordinates are converted to their initial values. For each corner of the cube, we form triangles (111 planes) and the Cartesian coordinates of the triangles vertices are computed (Figure 38b) so that their plane equations are formed. Next, equation conditions are expressed for atoms included to cuboctaedron (inside the truncated cubic structure) (Figure 38c). Every atom of the crystal cluster system is examined and if all the equation conditions are true for the specific atom, then it is kept to our final structure (Figure 41), otherwise it is rejected.

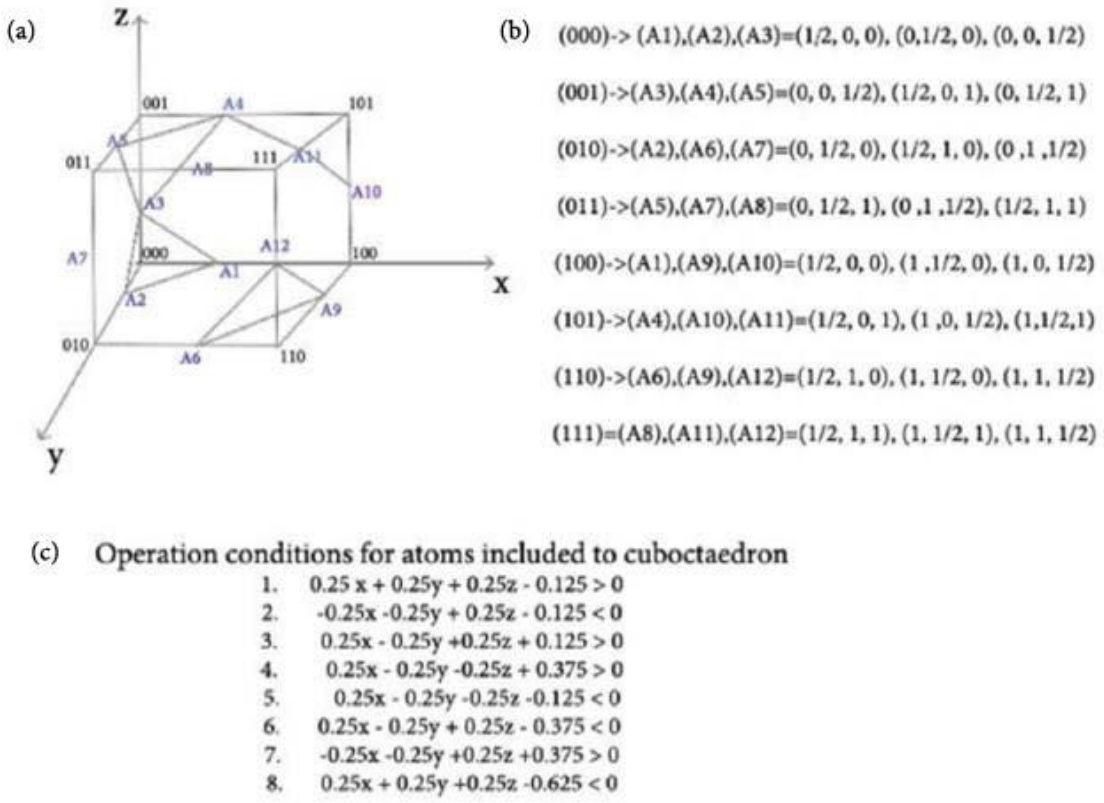

Figure 38: Geometric approach, (a) input crystal cluster structure, (b) expressed coordinates of the triangles and (c) the plane equation conditions for atoms included to cuboctaedron are shown.

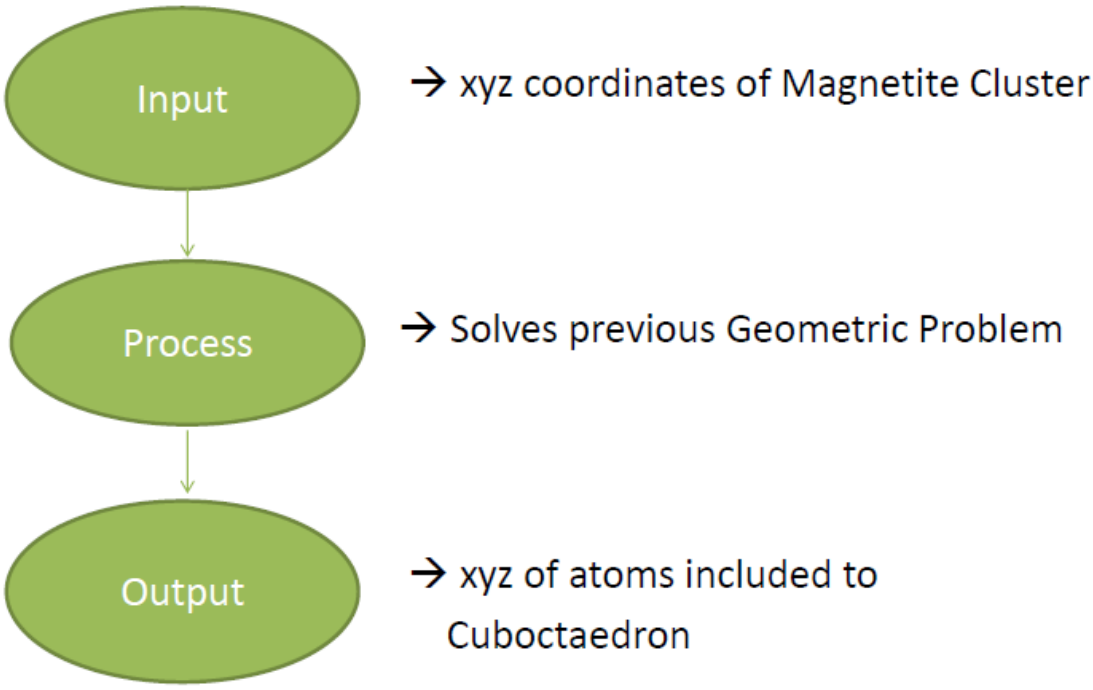

Figure 39: Computational approach workflow for building the magnetite core (cuboctaedron).

3.2.3 Technologies used

The program code is implemented using Matlab language [196]. The same procedure is implemented also in Python 3.6 [197].

3.2.4 Results

The derived morphology for magnetite nanoparticles core of a diameter of 3-nm based on stable growing surfaces of the magnetic crystal as it is visualized in VMD software [161], is shown in Figure 40.

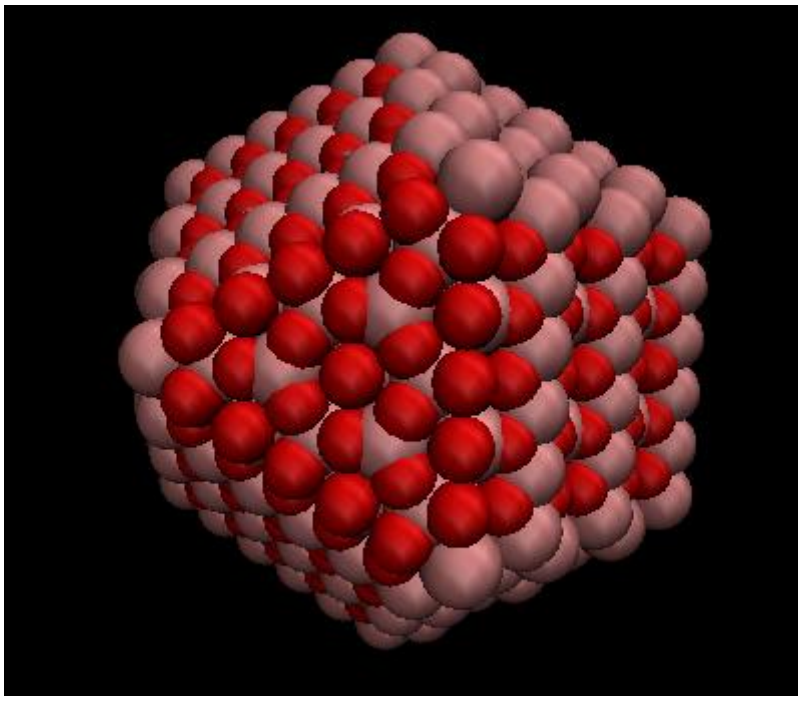

Figure 40: The derived morphology for magnetite nanoparticles core of a diameter of 3-nm based on stable growing surfaces of the magnetic crystal.

3.3 Crystal morphology tool

The past decades, significant attempts have been made to calculate accurately the growth morphology of crystals, although, it is still proven to be a difficult mission. The complexity of comprehending the crystal growth phenomena occur as a result of multifaceted interactions between diverse processes, observed on the different wide scales of time and length [156]. The procedures implicated throughout the crystal growth are exceedingly intricate, concerning multifaceted interactions for precise portrayal of the predicament. Crystals expose a great assortment of shapes, based on the chemical composition, their structure and growth requirements. The crystal shape directly imposes on the parting efficiency and the stability of crystalline chemicals, the

bioavailability, their function in biomedical applications (efficient delivery of drug molecules etc.) [162]. Therefore, the understanding of the growth behavior and morphological qualities of the molecular crystals is of vital significance in the comprehension and use of a variety of their physicochemical properties [156, 162].

Using crystallographic tools for measurement and computational image analysis, one might be able to identify the atomistic structure of a crystal. This process might work also in the reverse direction. Theoretically one might start from the atomistic structure of a crystal and try to predict the characteristic macroscopic morphology of the crystal, even before attempting to crystalize it in the laboratory.

A computational toolbox, able to make a link between macroscopic morphology and atomistic structure for a periodic crystal, would be a valuable tool for scientists. Our objective is the development of a crystal computational morphology toolbox for predicting and visualization of different crystal shapes. We use computational approaches for computing the macroscopic morphology of any periodic crystal by forming different shapes based on Miller indices and the distance measure from a reference point and visualizing the resulting crystal. That crystal is a polyhedron that is created as the intersection of multiple polyhedra and individual planes via the steps that follows.

3.3.1 Methodology

Listing of the intersecting planes

The first step is to keep a list of the intersecting planes. For each hkl triplet and the desired distance d from a reference point that have been provided by the user, the xyz coordinates for three points on the miller plane are estimated. Next, the coefficients A,B and C are computed and the corresponding plane equation P is defined (Figure 41). We apply the distance d from the reference point provided by the user and we calculate the coefficient D with the origin to be placed on the negative side (D<0). The last is a convention that is helpful for calculating the vertices of the polyhedron at the next steps.

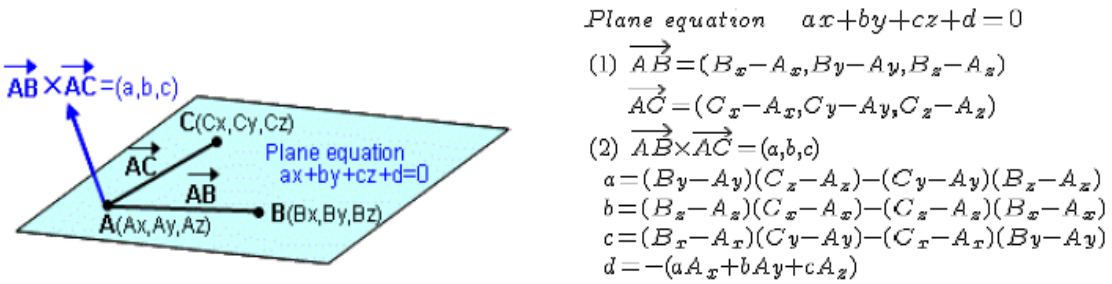

Figure 41: Defining the plane equations.

Furthermore, it is optional for the user to select if the symmetric planes would be included to the calculation. For that case, the original hkl triplet is rotated with respect to the unit cell that is used, their plane equations are calculated and they are also added to the list. The rotation is in 3 directions ([0,0,1] , [0,1,0], [1,1,1]) and in 4 angles (0^0, 90^0, 180^0, 270^0) (4^3 possible symmetric indices) and duplicates are removed. If not the symmetric option is selected, only the original miller plane is used.

Calculating polyhedron vertices

The second step is the calculation of the polyhedron vertices. To do so, an exhaustive search is performed to find all the intersection points by taking all possible combinations of three planes. For each group of 3 planes, we separate in couples. The intersection of each couple (if non parallel) is a line and the intersection of these lines (if non parallel) is a point (Figure 42).

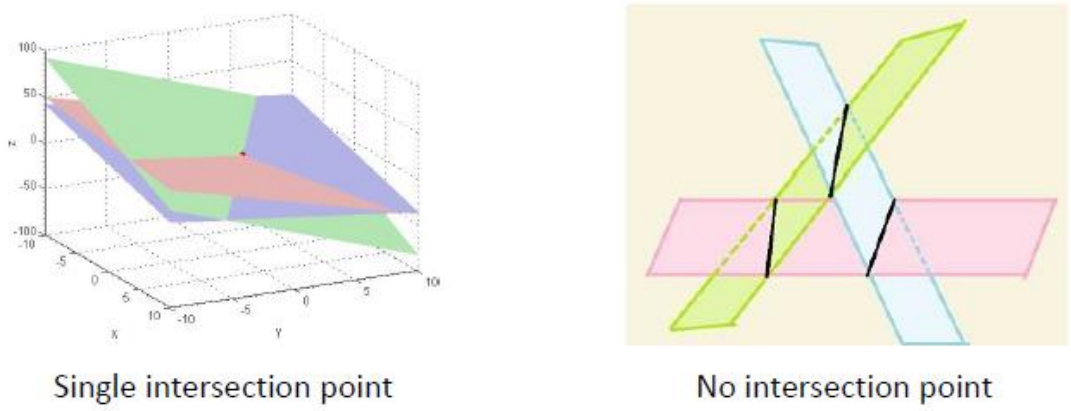

Figure 42: Example of a single intersection point from three planes (each two non-parallel) and a case of no intersection point.

These points are considered as potential vertices of the polyhedron. The polyhedron is the intersection of multiple polyedra, therefore the vertices are the vertices that lie on the "inner" planes (our convention is that the origin [0 0 0] is always on the negative side of all planes). So, the points that fall outside the polyhedron are discarded (it is checked using the plane equations); the rest form the set of the polyhedron vertices V (Figure 43).

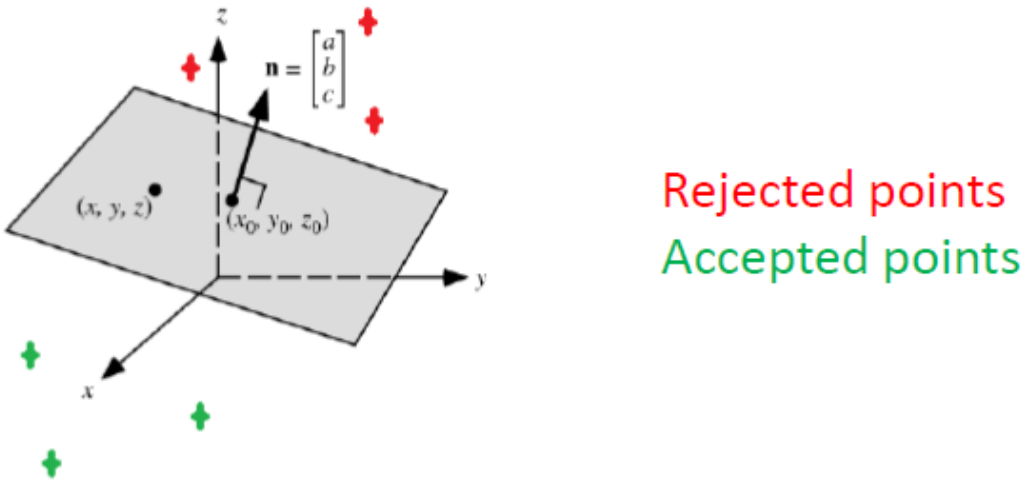

Figure 43: Calculating polyhedron vertices (rejected and accepted points).

Defining polyhedron faces

The third step is the definition of the polyhedron faces. In principle, we note that each face is a polygon that lies on one of the planes, it is defined by a subset of V and by a set E of ordered edges, i.e. line segments that connect vertices. For each plane, all vertices that lie on it (satisfies the plane equation) are first defined. The vertices are arranged in a sequential manner so that the line segments that constitute the edges of the polygon are indicated. Then, a polygon is created given these vertices using the Quickhull algorithm [163]. With the Quickhull algorithm, the convex hull of a set of points (in our case, the subset of the vertices) is defined.

- The convex hull of a geometric object (such as a point set or a polygon) is the smallest convex set containing that object (Figure 44). There are many equivalent definitions for a convex set S. The most basic of these is that a set S is convex if whenever two points P and Q are inside S and then the whole line segment PG is also in S.

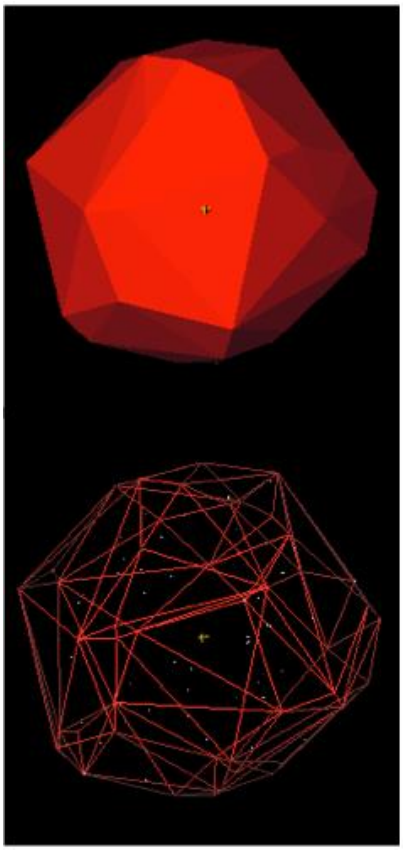

Figure 44: 3D convex hull of 120 point cloud. [164]

The Quickhull algorithm, uses the divide and conquer approach and its average case complexity is considered to be O(n*log(n)), whereas in the worst case it takes $O(n^2)$. In our implementation of the algorithm, the most distant points are connected with a (double) line segment, which initializes the set E. Then, in each of the iterative steps, the most distant point from any of the line segments in E is found; that line segment is replaced with two new ones, connecting the most distant point. The iterative steps of the

algorithm stop when all points have been included in the convex hull (Figure 45). This way, for each plane we obtain an ordering of the edges that form a closed chain, making it easy to display each face as a polygon in 3D space with the use of the libraries of the Development Environment.

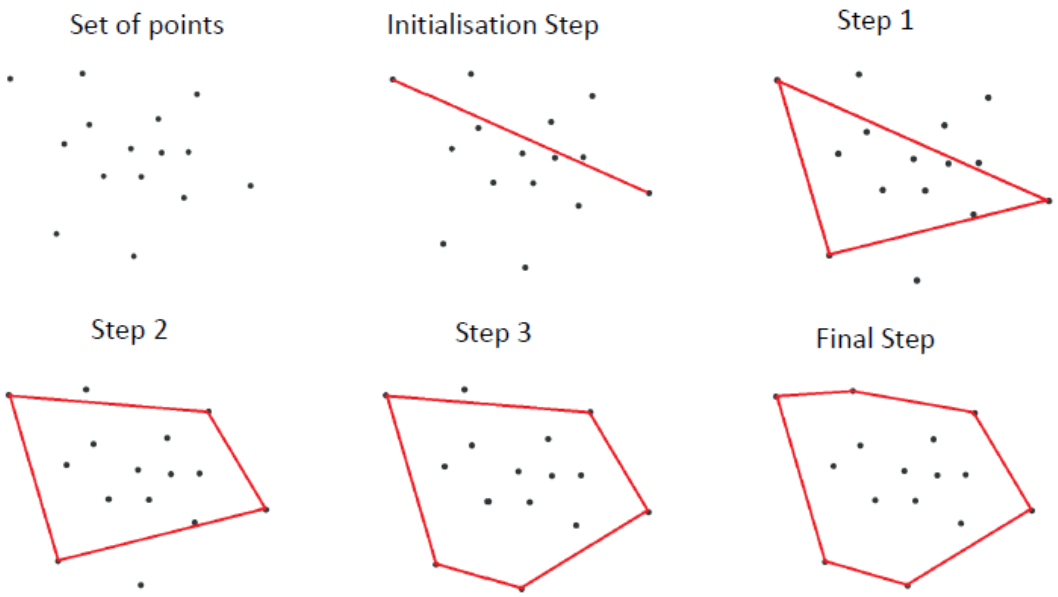

Figure 45: Quickhull algorithm steps.

3.3.2 Technologies used

This approach is implemented in both MATLAB [196] and C++ [198] (using OpenGL libraries for the visualization of the polygons and Qt 4.8.6 [199] for the graphical interface), the latter being an extension plugin to be included in a later version of MAPS 4.0.1 software [160].

```
#include "math.h"
#include "PolyhedronUtils.h"
#define PI 3.14159265358979323846

PolyhedronUtils::PolyhedronUtils(){
    functionCalls=new std::vector< std::string >();
}
PolyhedronUtils::~PolyhedronUtils(){}

void PolyhedronUtils::GeneratePlanes(vectArray Planes, const vectArray hklStruct, const vect distances, const std::vector<bool>* symmetric, std::vector<size_t>* colorIdx){
    functionCalls->push_back("GeneratePlanes");
    // This function creates an array of planes that correspond to the hkl indices, their respective distances and the symmetry indicators that are provided.
    // Note: The center of mass of the polyhedron is the origin (0,0,0)
    // Input:
    //      - vectArray Planes: an empty array that is filled with the coefficients of the planes (A,B,C,D) (let size M)
    //      - const vectArray hklStruct: the array of hkl triplets (let size N)
    //      - const vect distances: the array of the corresponding distances (also size N)
    //      - const std::vector<bool>* symmetry: the array of the symmetry indicators (also size N)
    //      - std::vector<size_t>* colorIdx: an empty array that is filled with the indices of the hkl triplets from where the planes were generated (size M)

    vect hkl;
    size_t i,j;
    bool useSymmetric;
    vect millerPlane;
    vectArray tempPlanes;  // a temporary struct of planes
    vectArray til;

    for (i=0; i<hklStruct->size(); i++){  // for each hkl triplet in hklStruct
        hkl=hklStruct->at(i);
        millerPlane=DefinePlane(hkl, (*distances)[i]);  // calculate the original plane  ****MillerPlane
        useSymmetric=symmetric->at(i);
        if (useSymmetric==true){
            til=new std::vector< vect >();  // a temporary array for holding symmetric hkl triplets
            tempPlanes=new std::vector< vect >();  // a temporary array for storing the planes that are generated for this triplet
```

Figure 46: GeneratePlanes function sample that creates an array of planes corresponding to hkl indices, their respective distances and the symmetry indicators that are provided.

```
void PolyhedronUtils::Face(const vect P, const vectArray Vp, vectArray polygon){
    functionCalls->push_back("Face");
    // This function implements the Quickhull algorithm in 3D space for forming a polygon.
    // The hull is defined by a sequence of line segments (LSeg) that form a closed shape; the start of the first LSeg is the end of the last LSeg.
    // It starts by connecting the most distant vertices in the set of vertices with a (double) line segment.
    // Then, in each iteration, the largest distance of one of the rest of the vertices to one of the line segments is found; the vertex is included in the hull and new LSegs are form
    // The iterations stop when all vertices are included in the hull.
    // Input:
    //      - const vect P: the plane where the face lies on.
    //      - const vectArray Vp: the subset of the vertices that lies on the plane.
    //      - vectArray polygon: the resulting polygon, where the vertices have been arranged in circular order.

    size_t i,j,k;
    double smallNumber = 0.001;  // a small number for checking equalities between double numbers. Should not be set to a lower value.

    double max=0;
    int imax=-1;
    int jmax=-1;
    double dist;

    // First, find the most distant vertices, let K and L.
    for (i=0; i<Vp->size(); i++){
        for (j=i+1; j<Vp->size(); j++){
            dist=EuclideanDistance(Vp->at(i),Vp->at(j));
            if (dist>max){
                max=dist;
                imax=i;
                jmax=j;
            }
        }
    }
```

Figure 47: Function sample for implementing the Quickhull algorithm in 3D space and forming a polygon.

3.3.3 Results

Display on screen

Some examples of the visualization of the output crystals derived from different combinations of Miller indices and distances from the center [0,0,0] are presented below. Different colors represent different individual or family of planes.

Matlab Implementation

- Miller indices {0 0 1}, {1 1 1}
- Distance from the center: 2Å

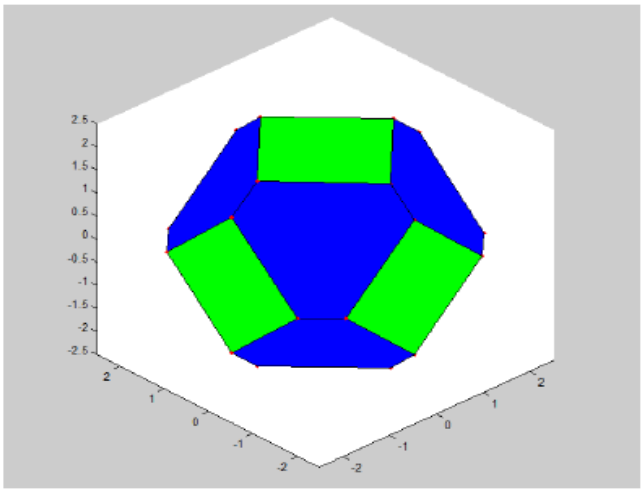

Figure 48: Matlab implementation first example (crystal morphology tool).

- Miller indices {0 0 1}, {1 1 1}
- Distance from the center: 2Å,1Å

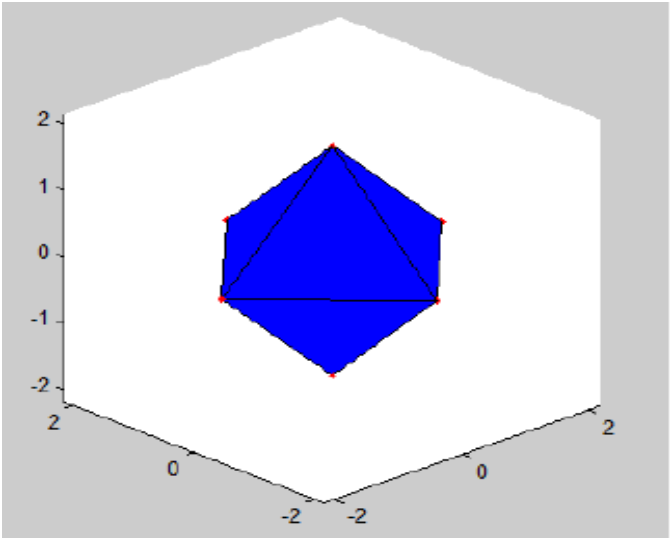

Figure 49: Matlab implementation second example (crystal morphology tool).

- Miller indices {0 0 1}, {1 1 1},{0 1 1}
- Distance from the center: 2Å

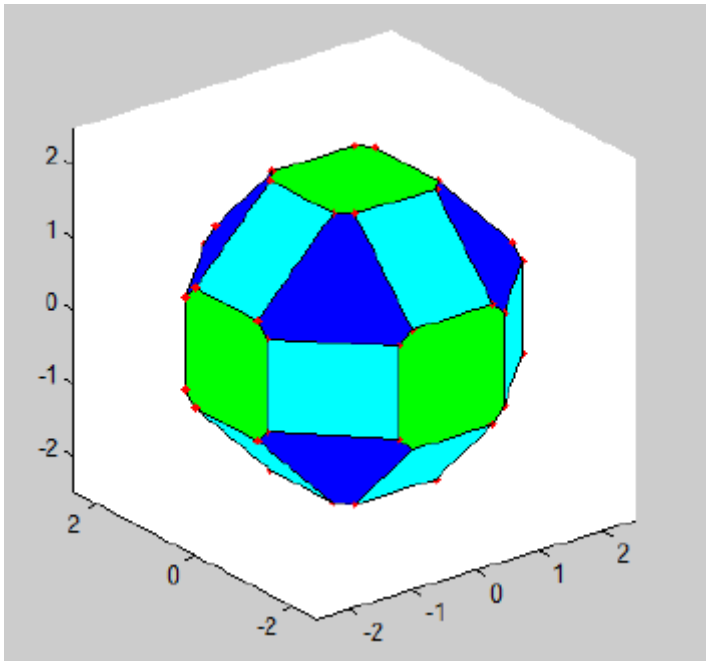

Figure 50: Matlab implementation third example (crystal morphology tool).

- Miller indices {001}, {111},{213},{357}
- Distance from the center: 2Å

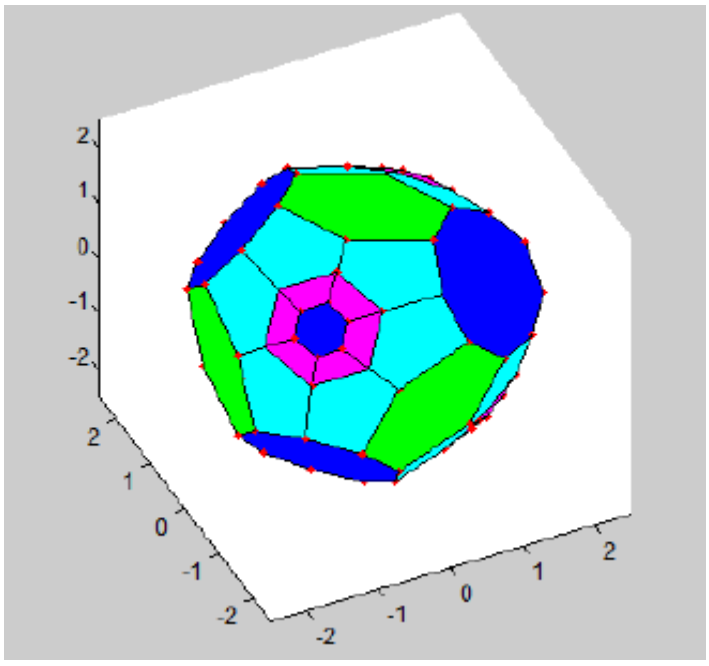

Figure 51: Matlab implementation fourth example (crystal morphology tool).

Implementation in MAPS [160]

Graphical Interface

The Qt add-on is used for the creating of an interactive Graphical User Interface. The user can define the hkl parameters using the menu as well as the distance from the origin and the color that will represent each plane or family of planes. There is also an option for including the symmetric planes or not (Figure 52).

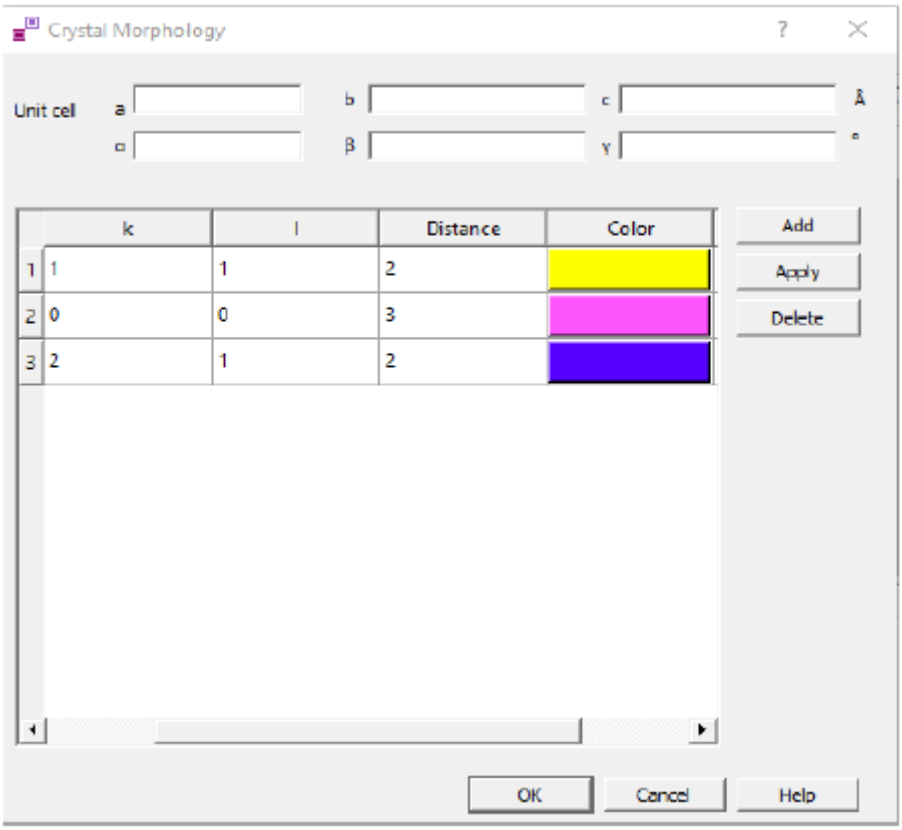

Figure 52: Graphical Interface (GUI) of Crystal Morphology Tool implemented in MAPS [160].

Some examples of the visualization of the output crystals are following. Features include also 360 view of the crystal using simple keyboard commands.

- Miller indices {001}, {111},{213},{357}
- Distance from the center: 2Å

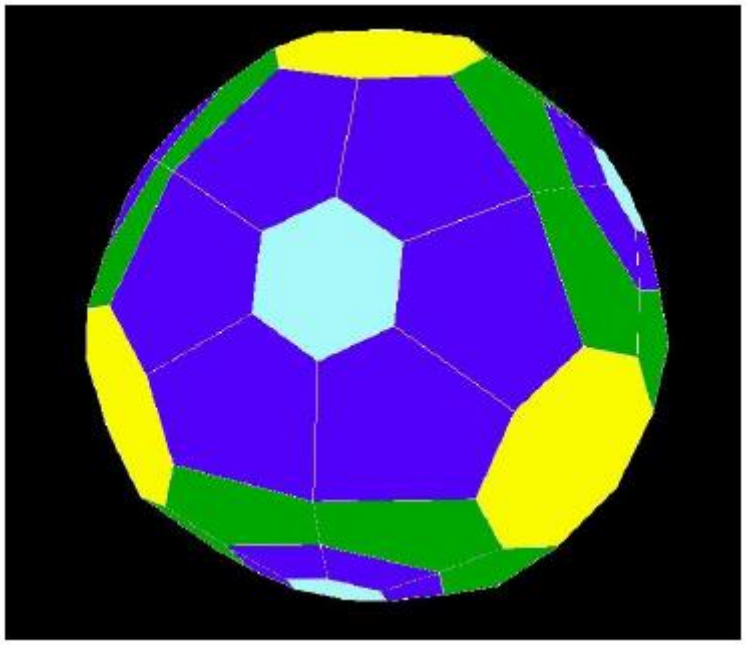

Figure 53: Maps [160] implementation first example (crystal morphology tool).

- Miller indices {001}, {111}
- Distance from the center: 2Å

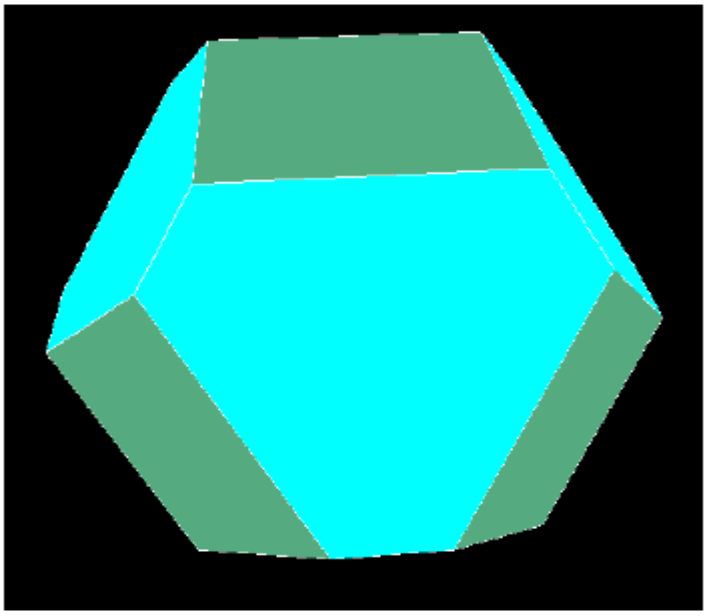

Figure 54: Maps [160] implementation second example (crystal morphology tool).

- Miller indices {001}, {111}, {011}
- Distance from the center: 3Å

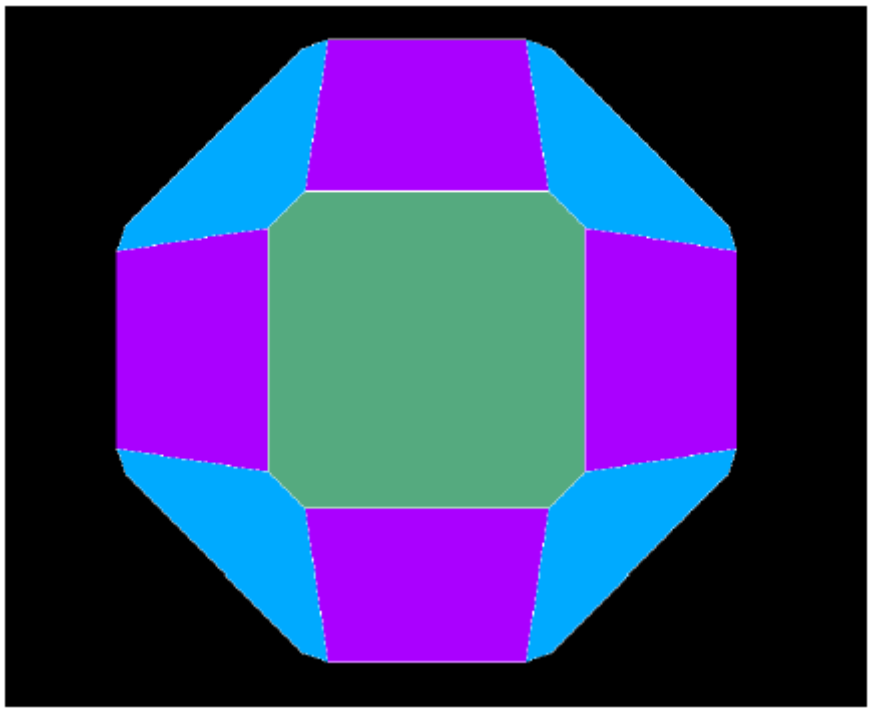

Figure 55: Maps [160] implementation third example (crystal morphology tool).

Figure 48 and Figure 54 represent the same crystal morphology that we created, in the subsection 3.2, for the magnetite nanoparticle (MNP) core. It represents a cuboctaedron with the (001) plane to dominate the morphology followed by the (111) plane that truncates the corners of the cube. Accordingly, the developed computational approach provides the computing of the macroscopic morphology of any periodic crystal by forming different shapes based on Miller indices and more particularly on the stable growing planes of any crystal structure.

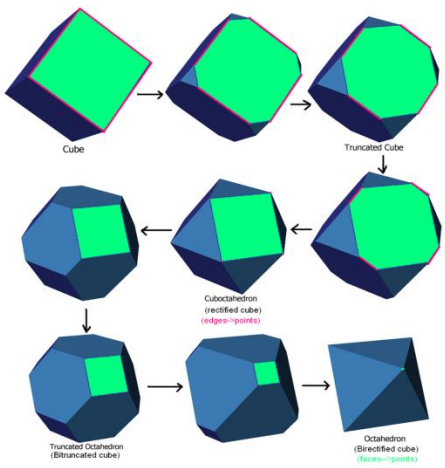

Figure 56: Truncation sequence from a cube to cuboctaedron and its dual octahedron. [165]

3.4 Functionalization of magnetite nanoparticle (MNP)

For functionalizing the magnetite core, two types of ligands are constructed, polyvinyl alcohol (PVA) and polyarabic acid (ARA).

PVA is a polyhydroxyl polymer (with a 1, 3 glycol structure) capable of undergoing both intra and intermolecular hydrogen bonding. It has the idealized formula $[CH_2CH(OH)]_n$. The small size and the strong hydrogen bond interactions of the hydroxyl groups force the polymer chains into a crystal lattice resulting in PVA being partially crystalline. Consequently PVA has excellent mechanical and thermal properties; excellent oxygen barrier properties; oil, grease and organic solvent resistance; low moisture permeability; high heat resistance and UV and IR radiation stability. In addition to this, it is biodegradable and non-toxic. Likewise fibers derived from PVA have similar properties and in addition, they have high tensile and compressive strengths, high tensile modulus and high abrasion resistance.

As a result of these unparalleled properties PVA has found usage as drug delivery systems in medicines and cancer cell-killing embolic material [166-170]. The major contributory factor towards the wide application of PVA is its water solubility. Water solubility is dependent upon the degree of hydrolysis, molecular weight, crystallinity and temperature [171]. The aqueous solubility of fully hydrolyzed PVA is brought about by its hydroxyl groups which have a high affinity to water resulting in strong hydrogen bonding [166].

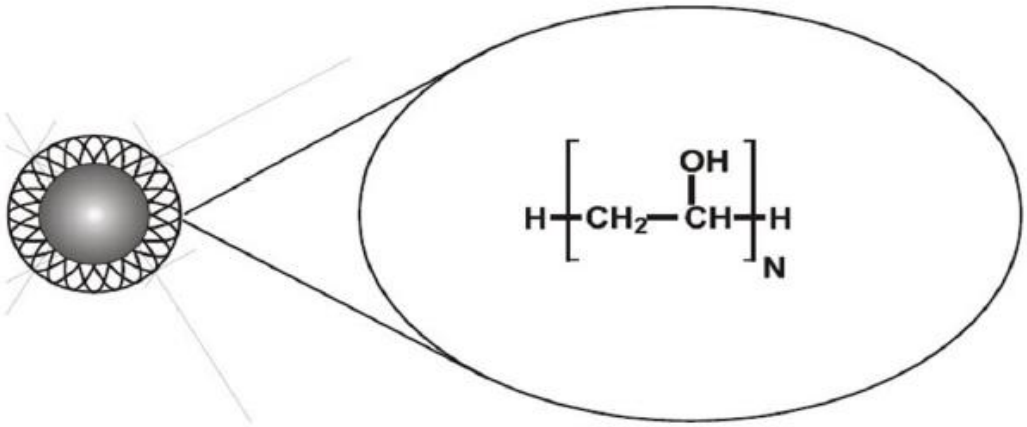

Figure 57: Magnetite nanoparticle core linked with PVA molecule chains.

There is no covalent bond between Fe_3O_4 and PVA. The most important bonding type is hydrogen bond. The interaction between PVA and magnetite is: $Fe^{2+} + H_2O \rightleftarrows Fe^{2+} \rightarrow OH_2$ (no covalent bond), the $Fe^{2+} \rightarrow OH_2$ can in turn form a hydrogen bond to an OH group of PVA.

The second functional group is the Polyarabic acid (ARA) or Arabic gum, a branched polysaccharide consisting of L-arabinose, D-galactose, L-rhamnose and D-glucuronic acid (Figure 59) in the ratio 3:3:1:1. Polysaccharides and glycoproteins in gum Arabic give it's glue and binder characteristics and it is used widely in pharmaceutical drugs or cosmetics.

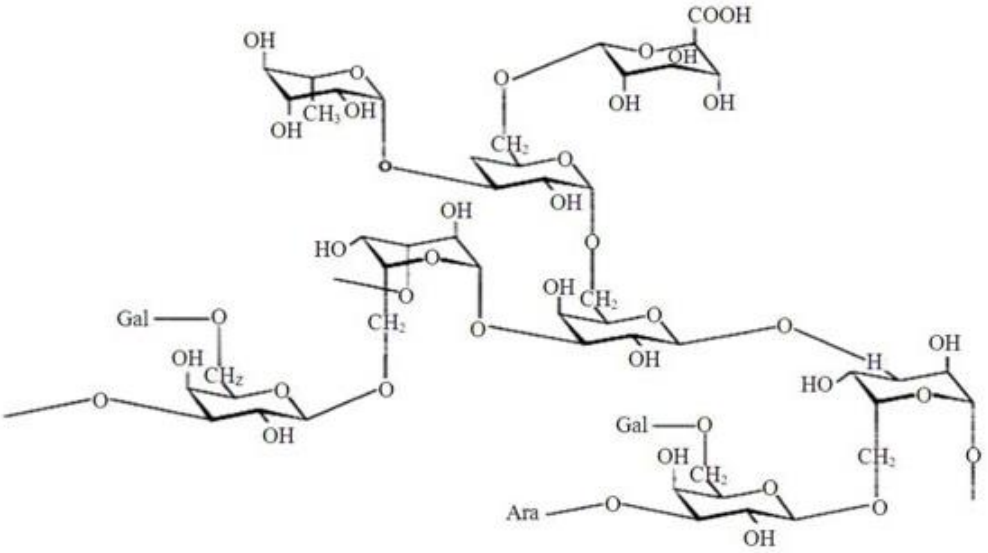

Figure 58: Structure of Gum Arabic. [172]

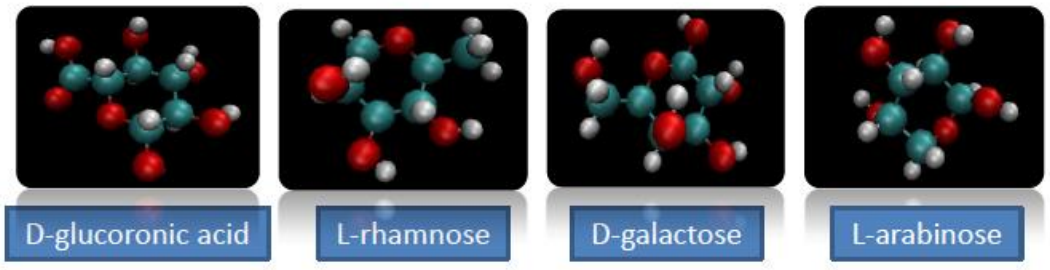

Figure 59: Structure of D-glucoronic acid, L-rhamnose, D-galactose and L-arabinose, sugar molecules covalently attached, visualized in VMD.

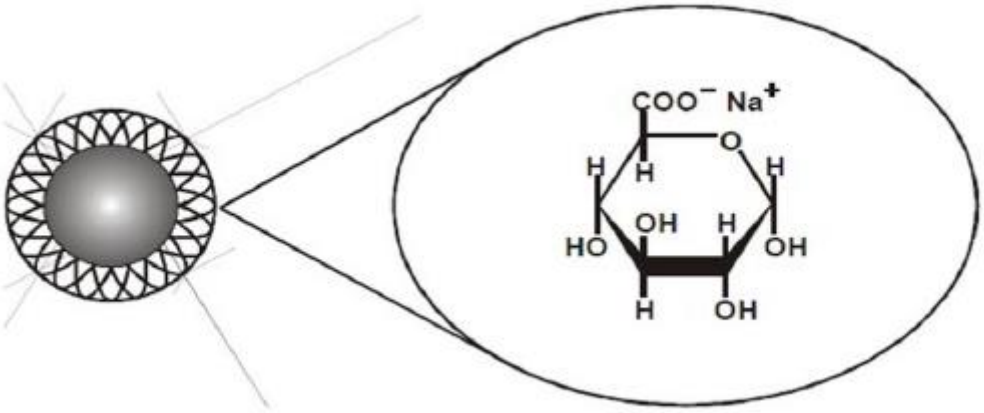

Figure 60: Magnetite nanoparticle core linked with Polyarabic acid (ARA) molecule chains.

The bonding between magnetite nanoparticle (MNP) core and ARA is caused by ionic interaction (Fe^{2+} and COO^- of D-glucoronic acid), hydrogen bonds and other weak bond types.

3.4.1 Methodology

In both cases, the interaction is between the Fe^{2+} octahedral surface atoms with the specific functional groups. Before constructing the chains, it is necessary the candidate surface Fe atoms of the magnetite core to be extracted using a computational automatic way.

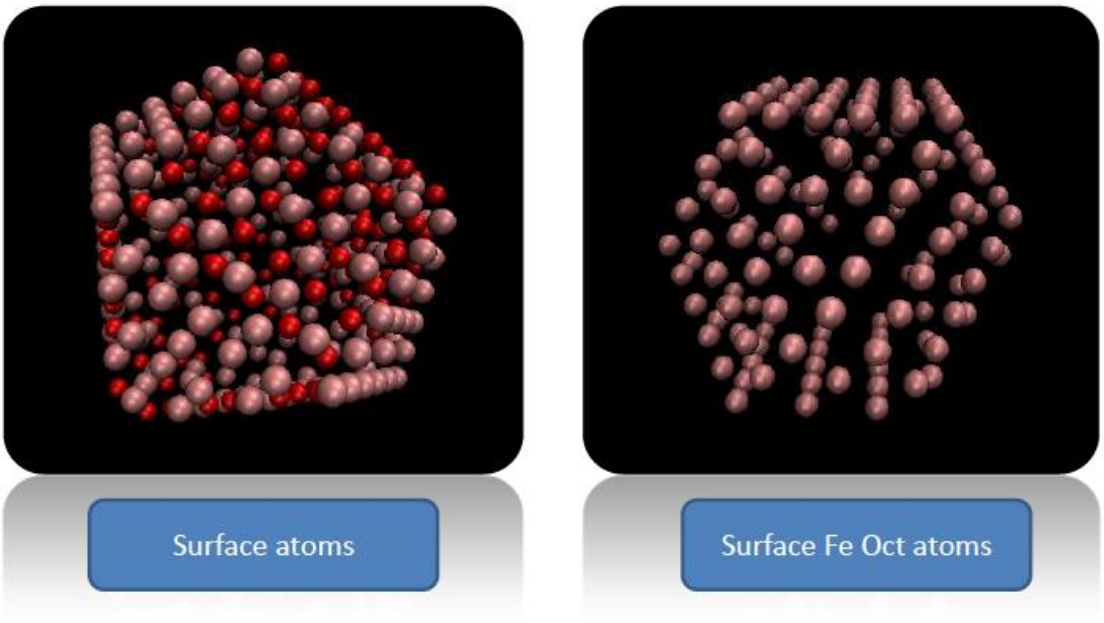

Figure 61: Extracting all surface Fe^{2+} atoms.

At previous steps, the plane equations of the magnetite core were defined. In order to extract atoms from the surface (Figure 61), the equation conditions are formed such that Ax+By+Cz+D=0 or very close to zero. All surface atoms are selected and then only the iron surface atoms that belong to octahedral sites (Fe^{2+}) are extracted. Next, the final selection continues with those Fe^{2+} atoms that are non-adjacent with each other. This is done using a cutoff for their Euclidian distance (~3 Å). Two configurations are derived with the second to be used in our study (Figure 62b).

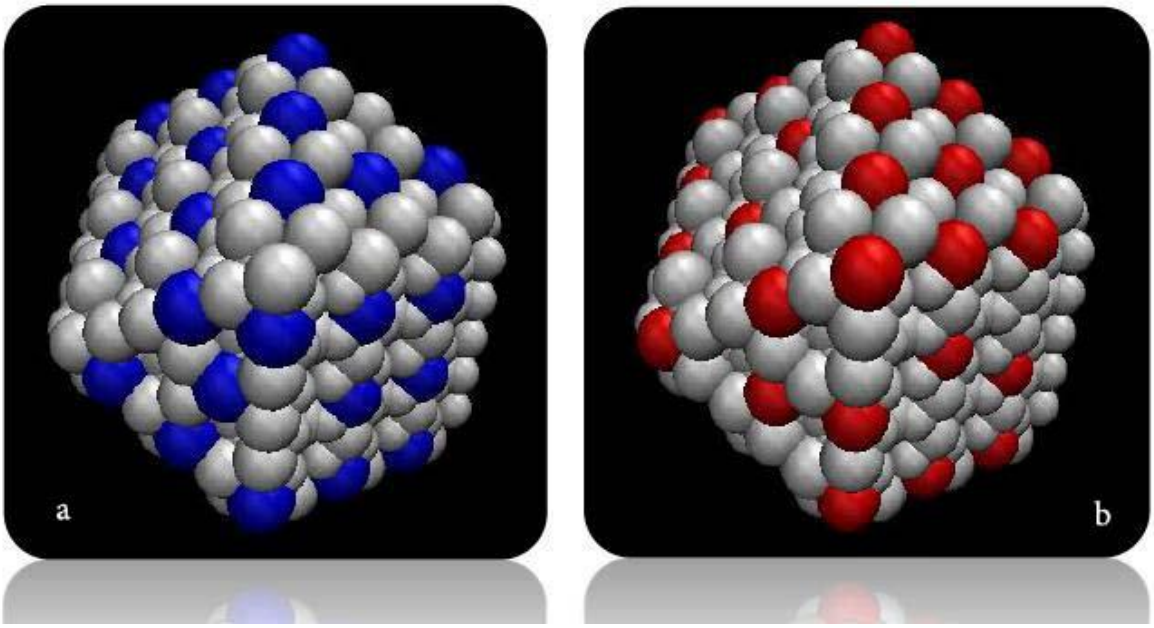

Figure 62: Fe^{2+} octahedral and non-adjacent surface atoms.

Subsequently, a dynamic code implementation allowed the ligand chains to be attached to selected surface octahedral Fe atoms of the MNP core with the option for the user to define the length of the chains used. The first chain is created manually and visualized in VMD software [161] and the atom names, bond lengths, angles and atom combinations were defined. Next, this information is used as a fundamental base for the code implementation, which builds automatically for every selected Fe atom all the PVA chains in all 3-dimensions (xyz). The same procedure is followed for the ARA molecule chains, with that system to be more complicated as it contains four different molecules in different ratios and angles between them. The user can define the length of the chains attached to the magnetite core and download the final output structure (.xyz file format).

```
function []=points()
%%

erwthsh = {'Select the number of PVA repeat units:'};
def = {'6'};
value = inputdlg(erwthsh,'Parameter Selection',1,def);
n=str2double(cell2mat(value(1)));

format longG
%load xyz file format
fid = fopen('c_1.xyz');
out = textscan(fid,'%s%f%f%f','HeaderLines', 2);
fclose(fid);
x=out{2};
y=out{3};
z=out{4};
array2=[out{1}];
%store xyz values to an array
array=[x y z];
array3=[];
array4=[];


names=['H', 'O', 'H', 'H', 'C', 'C', 'H', 'H', 'H']';
name=[];
for i=1:size(array,1)
```

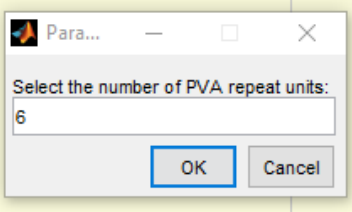

Figure 63: User option for selecting the number of PVA repeat units.

3.4.2 Technologies used

The program code is implemented using the Matlab (R2016b) [196] programming language.

3.4.3 Results

The two derived systems of magnetite core attached with different number of molecular chains for PVA and ARA are represented in Figures 64-65. In this study, the number of 30 repeat units is selected for our final system of magnetite core attached with the Polyvinyl alcohol (PVA) and the number of 2 repeat units for the Polyarabic acid (ARA).

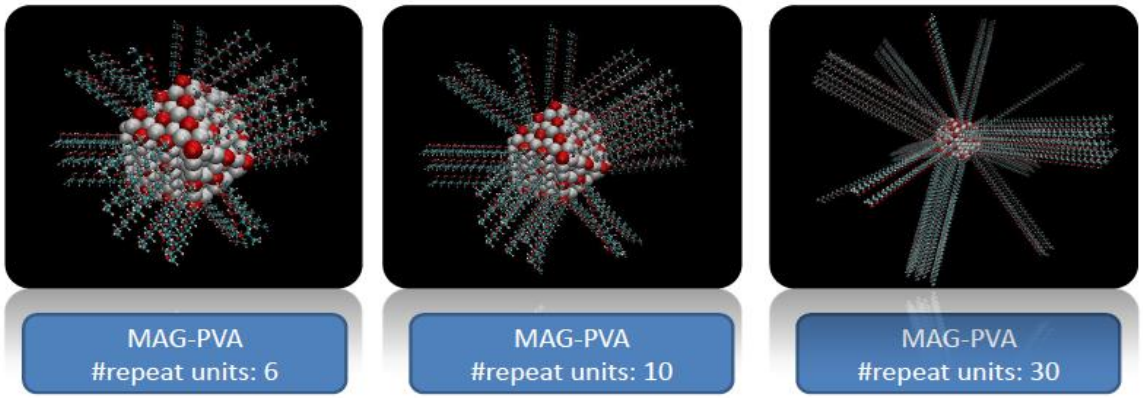

Figure 64: Magnetite core attached with different number of PVA repeat units as derived from our computational approach.

The first MNP was covered with 64 PVA chains with a length of 7.5 nm for each chain having a grafting density of 3 chains/nm^2. The second one was covered with the same number of ARA chains and same grafting density with a length of each chain to be 6.5 nm.

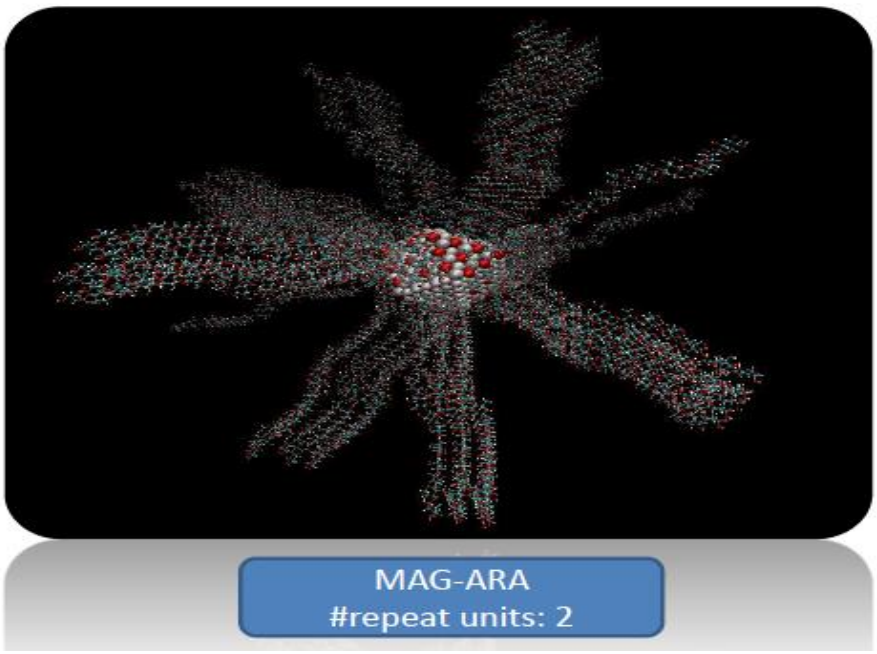

Figure 65: Magnetite core attached with Polyarabic acid (ARA) with number of repeat units 2 as derived from our computational approach.

3.5 Building the cell membrane

A dipalmitoylphosphatidylcholine (DPPC) lipid bilayer is built and used to model the cell membrane using the charmm-gui platform (http://www.charmm-gui.org/) [200]. CHARMM-GUI membrane builder as a web graphical user interface, automates the building process of heterogeneous lipid bilayers, with or without protein structures, maintaining a database of up to 140 different lipid types (pure or mixed bilayers). In parallel with other tools for protein/membrane model construction [173-177], Membrane Builder is used worldwide as it produces simulation inputs compatible with the most used simulation packages, various user options, lipid types and usable packed systems.

As shown in Figure 66, six subsequent steps generalize the process of building a protein/membrane or membrane only system.

Through a web browser, user's specific options are incorporated in each step and CHARMM input files are derived and run. Individual input and output files including generated structures as well as an archive of all the created files are available in each step. One can visualize the generated system in each step so that, if necessary, one can go back to the previous step and modify the options interactively.

As a lipid bilayer is needed in our study, we start from step 3 of the building process (Figure 66).

System Size Determination

For building homogeneous lipid bilayers, there are three types of lipid molecules, such as DMPC, DPPC, and POPC [104]. Membrane Builder facilitates the process by defining the system size based on users' inputs for (1) number of lipid layers, (2) number of lipid molecules, or (3) system dimensions. The total number of lipid molecules can promptly estimated by the number of lipid layers; this number corresponds to the number of lipid molecules from a protein to the closest edge in the system. The system size along the z-axis is determined by the thickness of bulk water from the protein dimension along the z-axis.

After the previous step is completed, Membrane Builder provides an inclusion of the determined system size and a lipid-packing image to help users to check if the system size is suitable. If the system is smaller or larger than expected, users can go back and specify the numbers of lipid molecules (option 2) or system dimensions (option 3) to enlarge or reduce the system size.

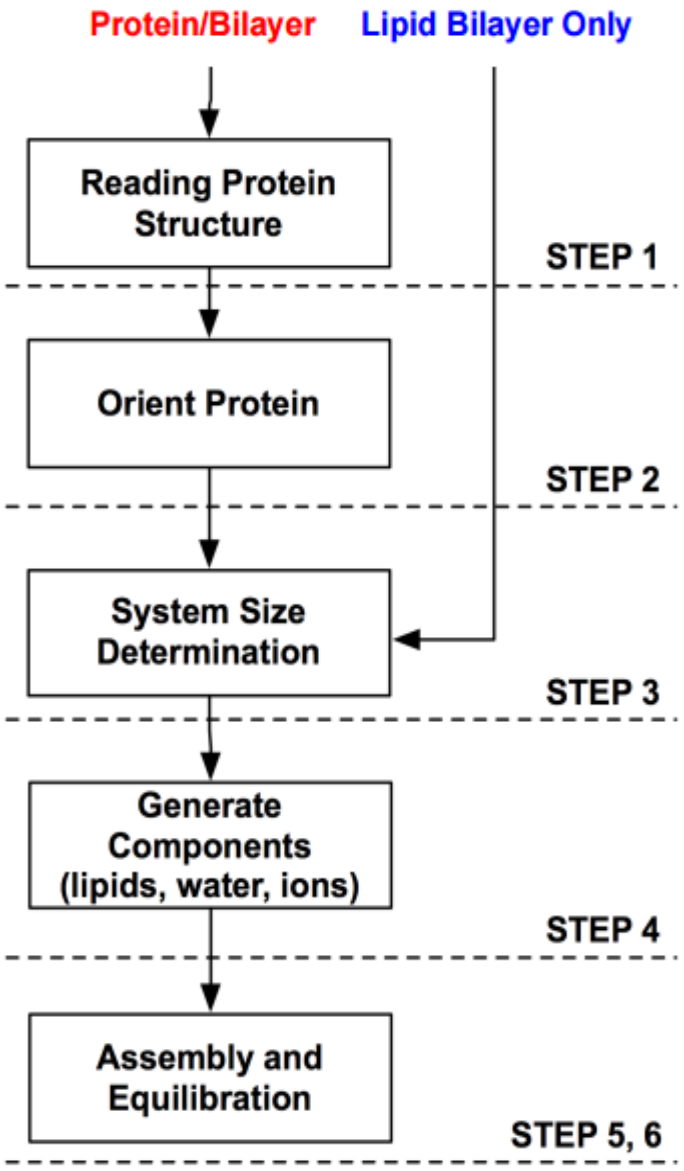

Figure 66: Overview of generalized process of building protein/membrane or membrane only complex system [178].

The determined system size for the DPPC lipid bilayer is shown in Figure 67. The option heterogeneous lipid is selected, a rectangular box type, water thickness 120 Å, the length of XY is based on lipid components and the number of 249 is selected for lipids at the upper and lower leaflet. Next, the replacement method is used as a system building option. In this method, lipid like pseudo atoms are first distributed and then replaced by lipid molecules one at a time [179–181]. Individual lipid molecules are randomly selected from a lipid library that contains various conformations of lipid molecules. This method allows one to easily control the system size and the number of lipid molecules while it generates a lipid bilayer.

Determined System Size:

Box Type	Rectangle		
Crystal Type	TETRAGONAL		
System Size	A	125.247754	Dimension along the A (X) axis
	B	125.247754	Dimension along the B (Y) axis
	C	274	Dimension along the C (Z) axis
Crystal Angle	Alpha	90.0	Angle between the axis B and C
	Beta	90.0	Angle between the axis A and C
	Gamma	90.0	Angle between the axis A and B
# of Lipids	on Top	249	
	on Bottom	249	
Z Center	0		Center of the system along the Z axis

Figure 67: Determined System Size provided by charm-gui membrane builder (DPPC lipid bilayer).

Generate Components

Based on the system size information, Membrane Builder generates individual components such as bulk water, and counter ions. In our system ions are included with ion concentration 0.15M of NaCl (332 positive ions and 332 negative ions are generated). The initial configuration of ions is then determined through Monte Carlo simulations using a primitive model, i.e., scaled Coulombic and van der Waals interactions.

Assemble and equilibration

Each component that has been generated in the previous step will be assembled in this step. One of the most significant advantages of using the web environment is that, if a problem is found, users can go back and re-generate the whole system again before quitting the browser. Therefore, the visualization of the initially assembled structure is important to verify if the system is reasonable.

After the membrane complex is assembled (Determined Final System Size- Table 6), the equilibration must be performed to relax the uncorrelated initial system before MD production simulations (Figure 69). However, due to the significant amount of computing power, Membrane Builder provides six consecutive CHARMM input files for equilibration, which can be modified for continual production simulations. As shown in Figure 68, to assure gradual equilibration of the initially assembled system, various restraints are applied to the protein (if used), water, ions, and lipid molecules during the equilibration [182]: (1) harmonic restraints to ions and heavy atoms of the protein, (2) repulsive planar restraints to prevent water from entering into the membrane hydrophobic region, and (3) planar restraints to hold the position of head groups of membranes along the Z-axis. These restraint forces are slowly reduced as the equilibration progresses. To warrant the successful equilibration, i.e., to avoid instability of dynamics integrations during equilibration, the NVT dynamics (constant volume and temperature) is used for the first and second steps, and the NPAT (constant pressure, area, and temperature) dynamics for the rest at 303.15 K (DMPC and POPC) and 323.15 K (DPPC).

Step	Ensemble[1]	Timesteps	Equilibration Time	Force Constants for Harmonic Restraint[2]				
				Protein Backbone[3]	Protein Sidechain[3]	Water[4]	Lipid[5]	Ion[3]
1	NVT	1 fs	25 ps	10.0	5.0	2.5	2.5	10.0
2	NVT	1 fs	25 ps	5.0	2.5	2.5	2.5	0.0
3	NPAT	1 fs	25 ps	2.5	1.0	1.0	1.0	0.0
4	NPAT	2 fs	100 ps	1.0	0.5	0.5	0.5	0.0
5	NPAT	2 fs	100 ps	0.5	0.1	0.1	0.1	0.0
6	NPAT	2 fs	100 ps	0.1	0.0	0.0	0.0	0.0

[1] NVT stands for constant volume and temperature, and NPAT for constant pressure, area, and temperature.
[2] Force constants are in kcal/(mol·Å^2).
[3] Positional harmonic restraints.
[4] Harmonic restraints to keep water molecules away from the membrane hydrophobic region.
[5] Harmonic restraints to keep the lipid tail in −5 Å<Z<5 Å, and lipid head groups close to the membrane surface (Z = ±17 Å for DMPC and Z = ±19 Å for DPPC and POPC).
doi:10.1371/journal.pone.0000880.t001

Figure 68: Detailed information on each equilibration step (charm-gui membrane builder).

Table 6: Determined Final System Size (charmm-gui membrane builder)

#of Atoms	**412150**	
Crystal Type	Tetragonal	
System Size	A	125.248
	B	125.248
	C	274
Crystal Angle	Alpha	90.0
	Beta	90.0
	Gamma	90.0
Lipid		
#of Lipids	On Top	249
	On Bottom	249
#of Water	115.582	
#of POT Ion	332	
#of CLA Ion	332	
Z Center	0.0	

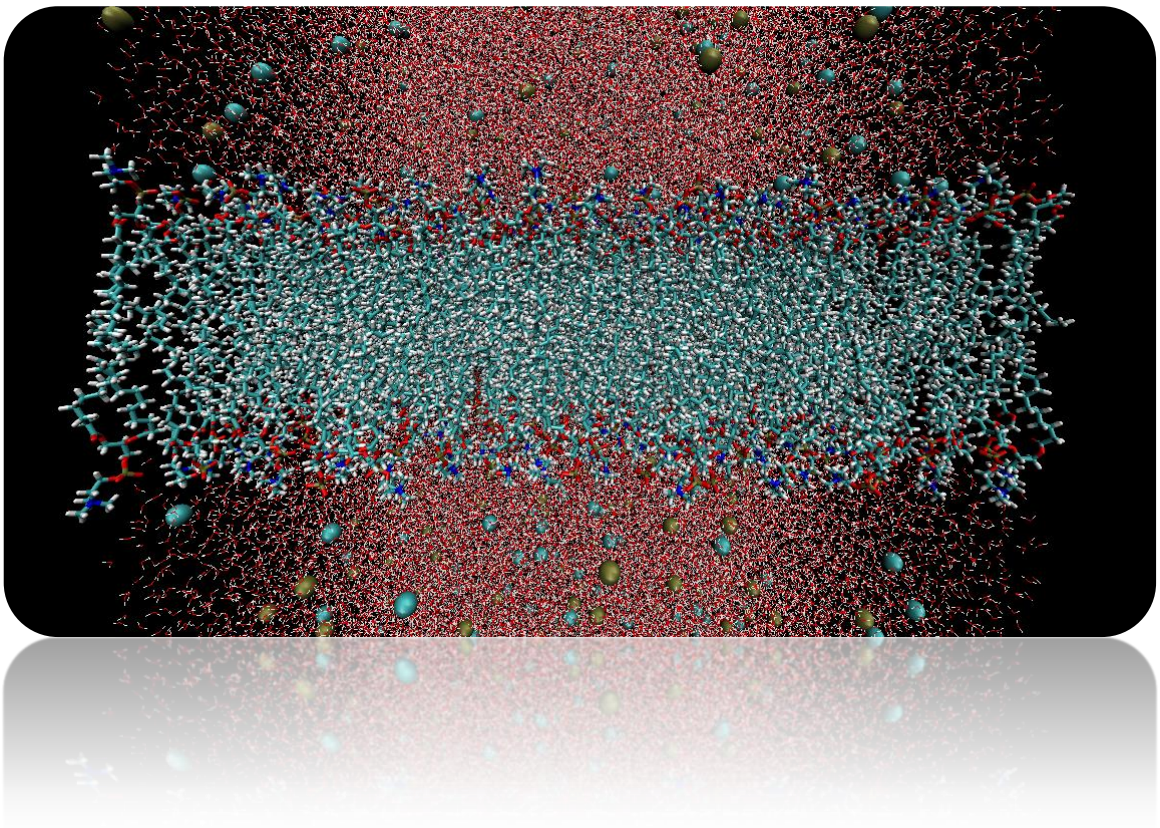

Figure 69: Representation of our DPPC lipid bilayer created by the Membrane Builder of charm-gui (412,150 atoms) during equilibration.

3.6 Gromacs Topology Tool

For running our Molecular Dynamics Simulations using Gromacs simulation package, version 5.0.6 [183], topology files including information for the magnetite core and the two types of molecular chains are needed. In Figure 70, a topology file example in Gromacs is given.

```
;
;       Example topology file
;
[ defaults ]
; nbfunc        comb-rule       gen-pairs       fudgeLJ fudgeQQ
  1             1               no              1.0     1.0

; The force field files to be included
#include "rt41c5.itp"

[ moleculetype ]
; name  nrexcl
Urea         3

[ atoms ]
;   nr    type   resnr  residu    atom    cgnr  charge
     1       C       1    UREA      C1       1   0.683
     2       O       1    UREA      O2       1  -0.683
     3      NT       1    UREA      N3       2  -0.622
     4       H       1    UREA      H4       2   0.346
     5       H       1    UREA      H5       2   0.276
     6      NT       1    UREA      N6       3  -0.622
     7       H       1    UREA      H7       3   0.346
     8       H       1    UREA      H8       3   0.276

[ bonds ]
;  ai    aj funct           c0           c1
    3     4     1 1.000000e-01 3.744680e+05
    3     5     1 1.000000e-01 3.744680e+05
    6     7     1 1.000000e-01 3.744680e+05
    6     8     1 1.000000e-01 3.744680e+05
    1     2     1 1.230000e-01 5.020800e+05
    1     3     1 1.330000e-01 3.765600e+05
    1     6     1 1.330000e-01 3.765600e+05

[ pairs ]
;  ai    aj funct           c0           c1
    2     4     1 0.000000e+00 0.000000e+00
    2     5     1 0.000000e+00 0.000000e+00
    2     7     1 0.000000e+00 0.000000e+00
    2     8     1 0.000000e+00 0.000000e+00
    3     7     1 0.000000e+00 0.000000e+00
    3     8     1 0.000000e+00 0.000000e+00
    4     6     1 0.000000e+00 0.000000e+00
    5     6     1 0.000000e+00 0.000000e+00

[ angles ]
;  ai    aj    ak funct           c0           c1
    1     3     4     1 1.200000e+02 2.928800e+02
    1     3     5     1 1.200000e+02 2.928800e+02
    4     3     5     1 1.200000e+02 3.347200e+02
    1     6     7     1 1.200000e+02 2.928800e+02
    1     6     8     1 1.200000e+02 2.928800e+02
    7     6     8     1 1.200000e+02 3.347200e+02
    2     1     3     1 1.215000e+02 5.020800e+02
    2     1     6     1 1.215000e+02 5.020800e+02
    3     1     6     1 1.170000e+02 5.020800e+02
```

Figure 70: Topology file example in Gromacs.

Topology information include partial charges, bond lengths of bonded atoms and their force constants along with their atomic indexes. The same information is needed for their angles and the dihedral angles that are formed.

For the magnetite core, the partial charges are selected from the table 4 of [184]. The Fe^{2+}, Fe^{3+} and O^{2-} have partial charges 1.54, 1.76 and -1.21 respectively. In order all lengths and angles of bonded atoms to be defined, the magnetite unit cell is the starting point as its values are repeated for the whole structure. In Figure 71, these values are presented. As a result, that atomic combinations along with their bond distances and angle degrees are used as a “motif” for finding the atomic indexes of the whole structure.

In Figure 72, the workflow of this computational approach is shown. The Cartesian coordinates of the initial structure (magnetite core) are given as input, the computation that belongs to the main process starts including atomic information criteria for bonds and angles (Figure 71). The Euclidian distance between atoms and their angles are

computed. The atoms that satisfy the atomic criteria are included to the output file, otherwise they are rejected. The output file format is compatible to the Gromacs simulation package (.itp file format).

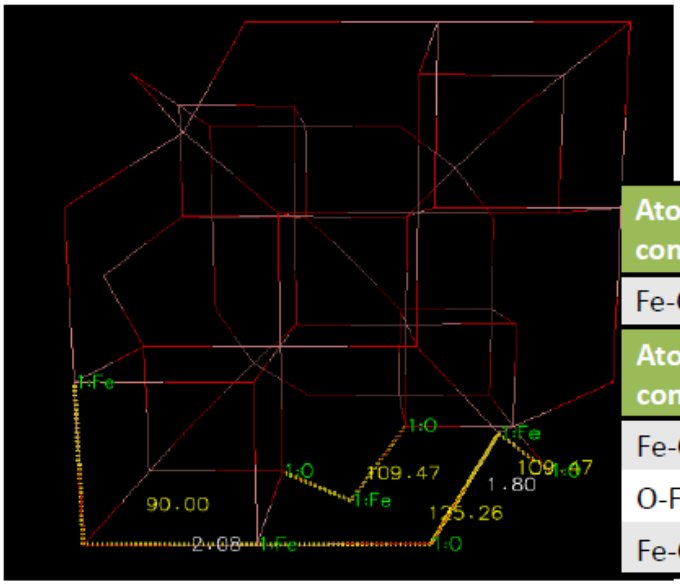

Atom combinations	Bond Distance (Å)
Fe-O	2.08Å || 1.80Å
Atom combinations	**Angle (degrees)**
Fe-O-FE	90◦
O-Fe-O	109.47◦
Fe-O-Fe	125.26◦

Figure 71: Bond distances and angle degrees for magnetite unit cell bonded atoms.

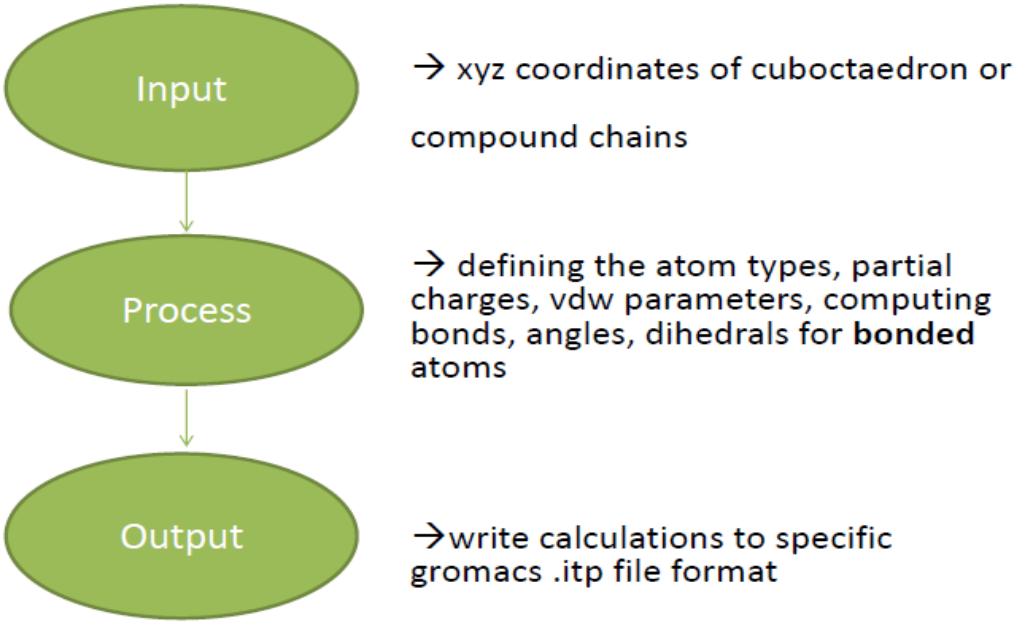

Figure 72: Computational approach workflow for creating topology files for Gromacs simulation package.

Similarly, for the molecular chains of Polyvinyl alcohol (PVA) and Polyarabic acid (ARA), the bond lengths and angles are defined for one repeat unit of the chain, which is used again as “motif” for defining dynamically the indexes of all the atoms. The average number of combinations for bonded atoms (bonds/angles/dihedrals) is 45,000. For Polyarabic acid (ARA), the procedure is more advanced as it consists of 4 different molecules in different ratio and angles between them. The average number of

computed combinations for bonded atoms (bonds/angles/dihedrals) is 60,000. The total number of atoms examined is 14,969 for the first system (MAG-PVA) and 20,968 for the second system (MAG-ARA).

Technologies used

The program code is implemented using the Matlab [196] programming language.

3.7 Molecular dynamics (MD) simulations

All simulations are carried out using the GROMACS simulation package, version 5.0.6 [183]. The CHARMM36 force-field [185] is used, with the non-bonded epsilon parameter for van der Waals interactions added for magnetite Fe^{2+} atoms from [186]. For the modeling of the waters, the TIP3P water model is employed [187].

Regarding the membrane system, after the membrane complex is assembled by the charmm-gui membrane builder, the equilibration is performed to relax the uncorrelated initial system before MD production simulations. However, due to the significant amount of computing power that cannot be hosted in charmm-gui server, Membrane Builder provides six consecutive CHARMM input files for equilibration, which can be modified for continual production simulations.

At first, 5,000 minimization steps using the steepest descent method are performed for the system of lipid bilayer (DPPC) membrane. Equilibration of 225,000 steps of the system is performed in the NPT ensemble using constant number of particles, temperature and pressure, using a time step of 2fs. Furthermore, Molecular Dynamics (MD) simulations are carried out for 10ns of the whole system using the same ensemble.

For the system of the magnetite core, 50,000 minimization steps using the steepest descent method are performed. Molecular Dynamics (MD) simulation for 1 ns of the system is performed in the gas phase using constant number of particles, volume and energy (NVE ensemble), without periodic boundary conditions (PBC) and thermostat and barostat control. Our results indicate that our morphology of the magnetite core (cuboctaedron) leads to a stable structure.

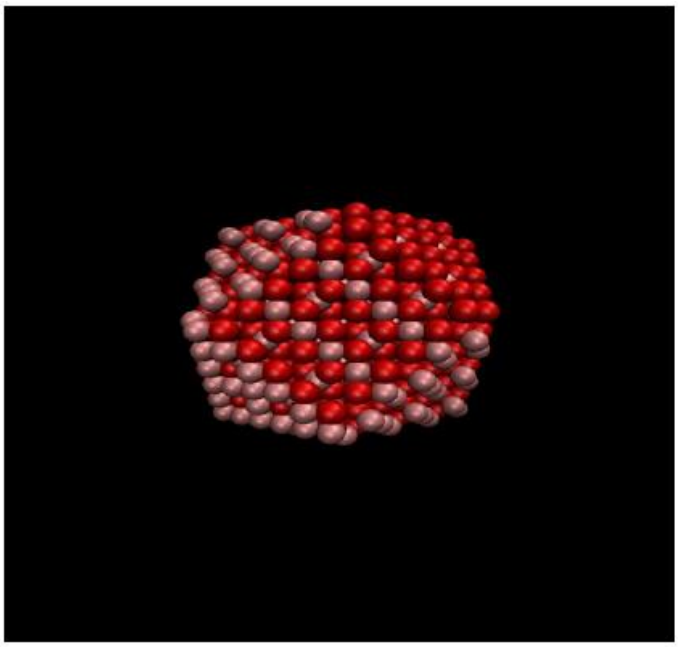

Figure 73: Magnetite core in vacuum (NVE) molecular dynamics simulation.

Subsequently, Molecular Dynamics (MD) simulations are carried out for 1 ns of the whole system using constant number of particles, volume and energy (NVE ensemble) (Figure 74- 75) and for 30 ns in the water phase using constant pressure, temperature, and number of particles (NPT ensemble) with periodic boundary conditions (PBC) (Figure 76). We obtain that the chains during the two types of simulations are gathered close to the surface of the magnetite core due to their attraction with the nanoparticle iron and oxygen atoms and their hydrophobic interaction with the water molecules.

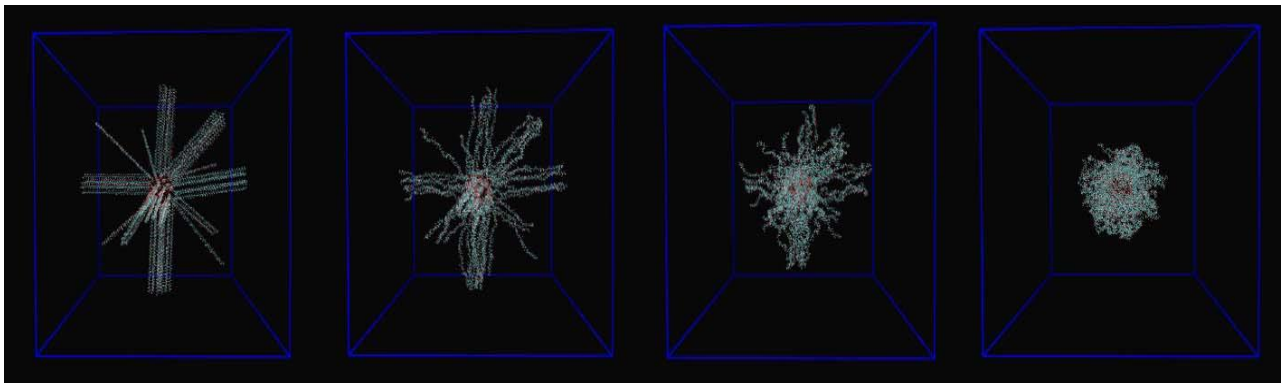

Figure 74: Magnetite core attached with PVA during vacuum simulation for 1ns (NVE).

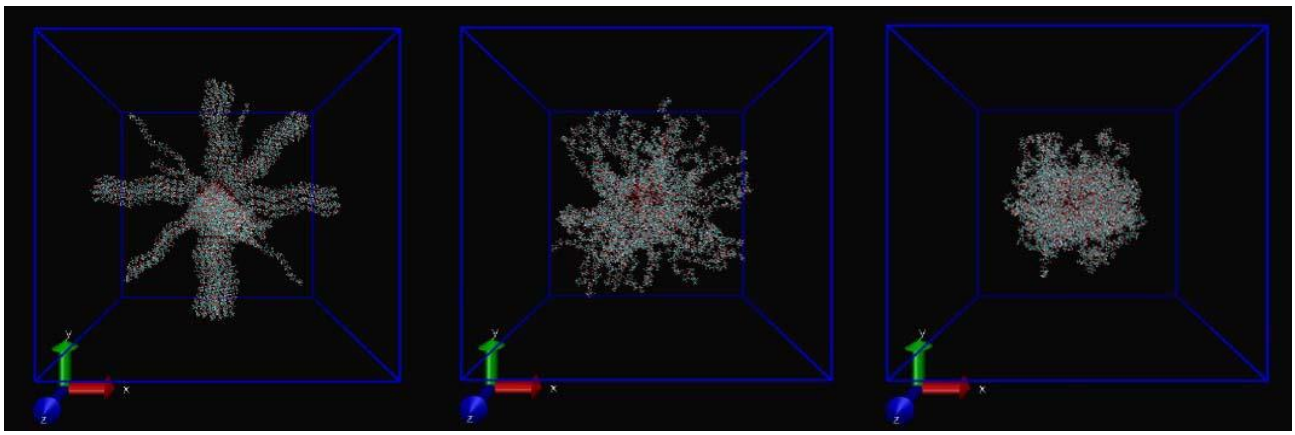

Figure 75: Magnetite core attached with ARA during vacuum simulation for 1ns (NVE).

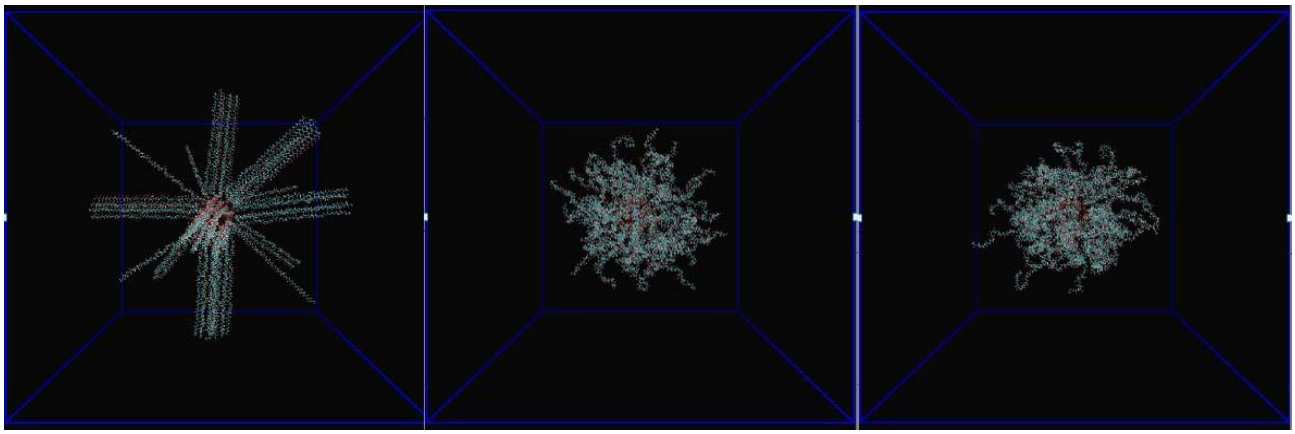

Figure 76: Magnetite core attached with PVA in water for 30ns (NPT).

Insertion of functionalized magnetite nanoparticle to the cell membrane

After running the above simulations, the two systems of magnetite core attached with PVA and ARA chains, are used in order to be inserted to the cell membrane. The configurations of gathered chains are selected and placed at the water phase of the lipid bilayer using VMD software [161]. After positioning the two systems (MAG-PVA and MAG-ARA), overlapping water molecules and ions are removed and the topology file is updated containing information for the whole system configuration. For the MAG-ARA system, which has a bigger diameter, the lipid bilayer is replicated containing 489 number of lipids on each side of the membrane. The first system contains 300,110 atoms (Figure 77) and the second 619,500 atoms (Figure 78).

Finally, Molecular Dynamics (MD) simulations are performed for 50 ns of the whole system in the water phase of the lipid bilayer using constant pressure, temperature, and number of particles (NPT ensemble). The temperature is kept constant at 310 K using the Nose-Hoover thermostat with a relaxation time of 1ps [188]. The Parrinello-Rahman algorithm is used to maintain constant pressure. Electrostatic interactions are calculated with particle mesh Ewald [189]. The real-space electrostatic and van der Waals cutoff distances are set at 12 Å, with smooth truncation starting at 10 Å. A simulation time step of 1 fs and periodic boundary conditions are employed.

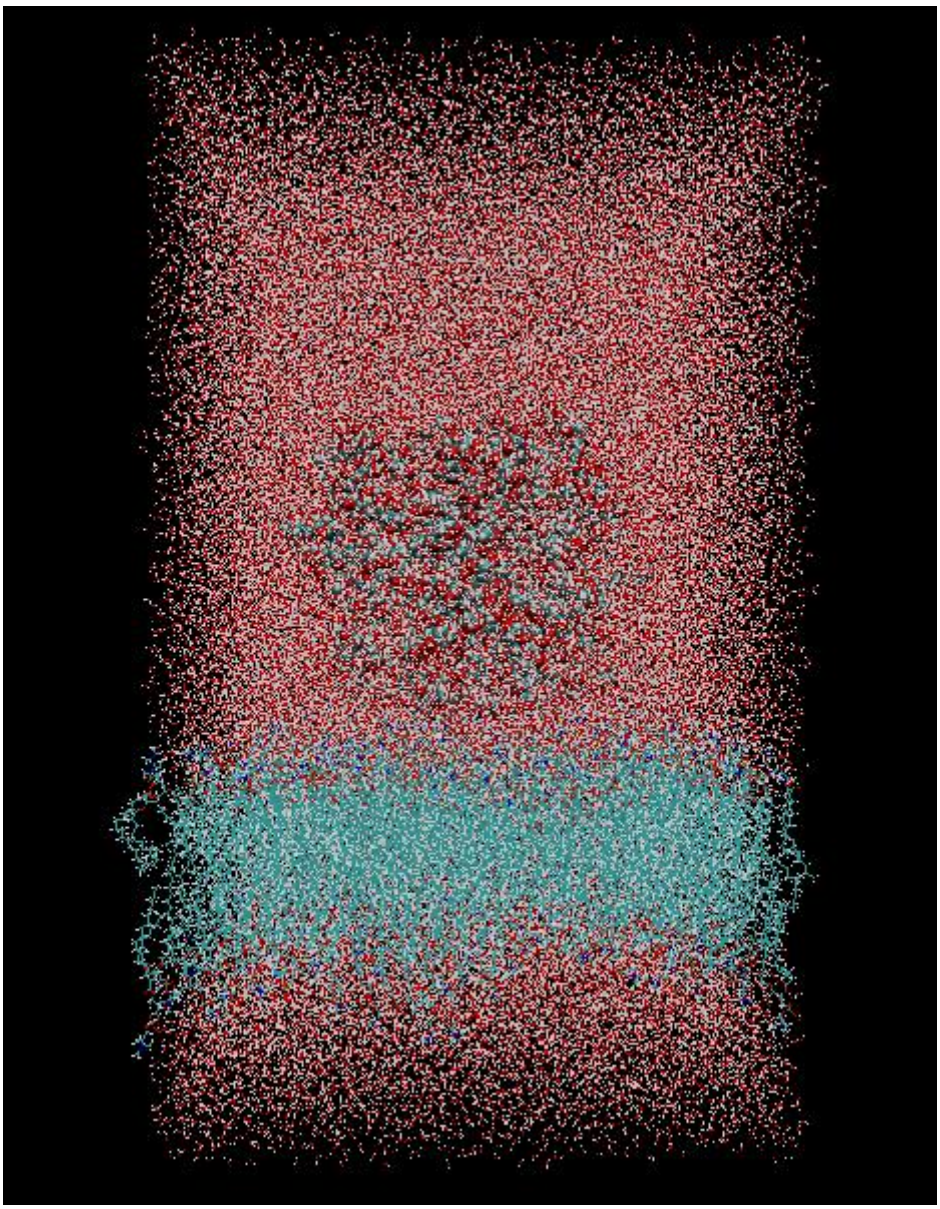

Figure 77: MAG-PVA at the water phase of the lipid bilayer (total #of atoms 300,110).

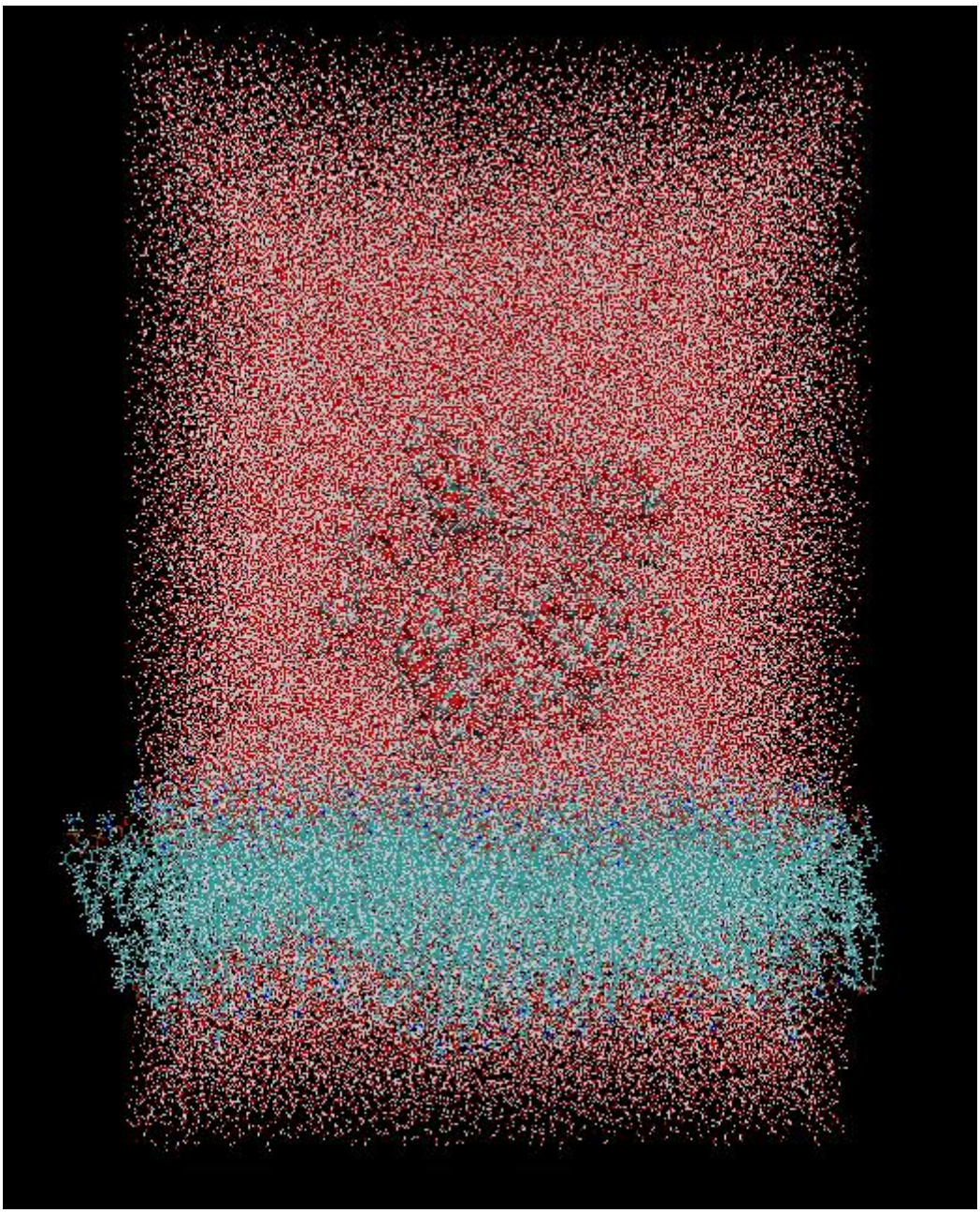

Figure 78: MAG-ARA at the water phase of the lipid bilayer (total #of atoms 619,500).

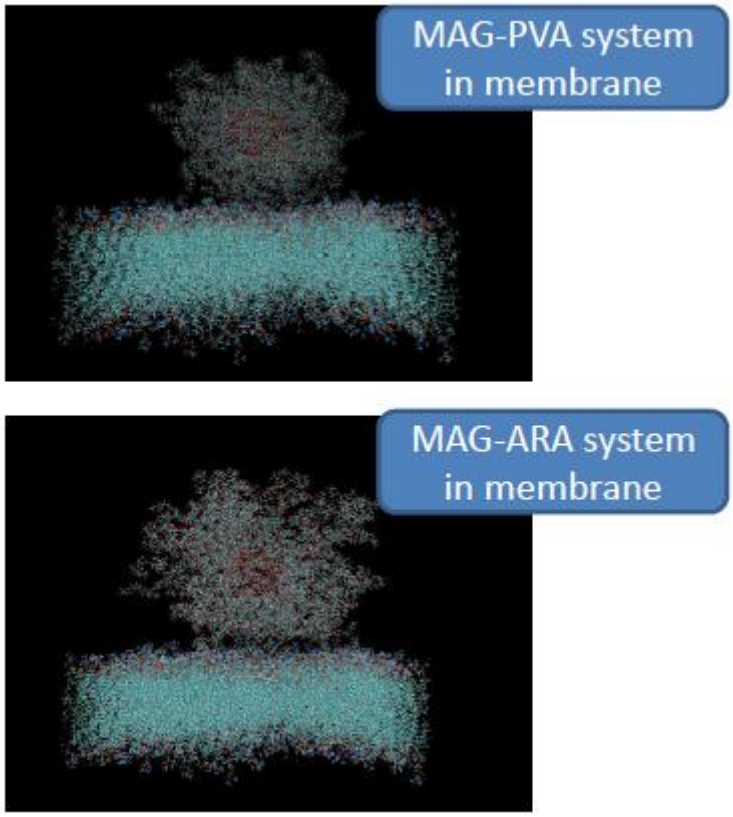

Figure 79: MAG-PVA and MAG-ARA in membrane.

MD analysis - Hbonds

A hydrogen-bond is considered as an attractive interaction between a hydrogen atom connected to an electronegative atom and an electronegative atom or group of atoms in the same or a different molecule in which there is evidence of bond formation [190].

MD simulations of the MAG-PVA system are first performed for 50ns in the presence of a DPPC lipid bilayer in order to study the positioning of the nanoparticle in the bilayer and the interactions of the hydroxyl (OH) group of the PVA with the membrane in atomic-level detail. MAG-PVA was initially placed in the water phase at 2-3 Å away from the lipid bilayer. It is evident from the simulations that MAG-PVA shows a medium preference (compared with the MAG-ARA system) for the membrane environment and within the first 10 ns it starts interacting with the polar headgroups of the lipid bilayer. Analysis of the hydrogen bonds between the MAG-PVA and bilayer shows that PVA hydroxyl groups interact preferentially with the phosphate than choline and perform 1-2 hydrogen bonds on average during the simulation time. It also shows preferential solvation (Figure 82) from the water phase than the MAG-ARA system (Figures 91-94). No internalization is observed during the simulation time. Our conclusions are consistent with the experimental results.

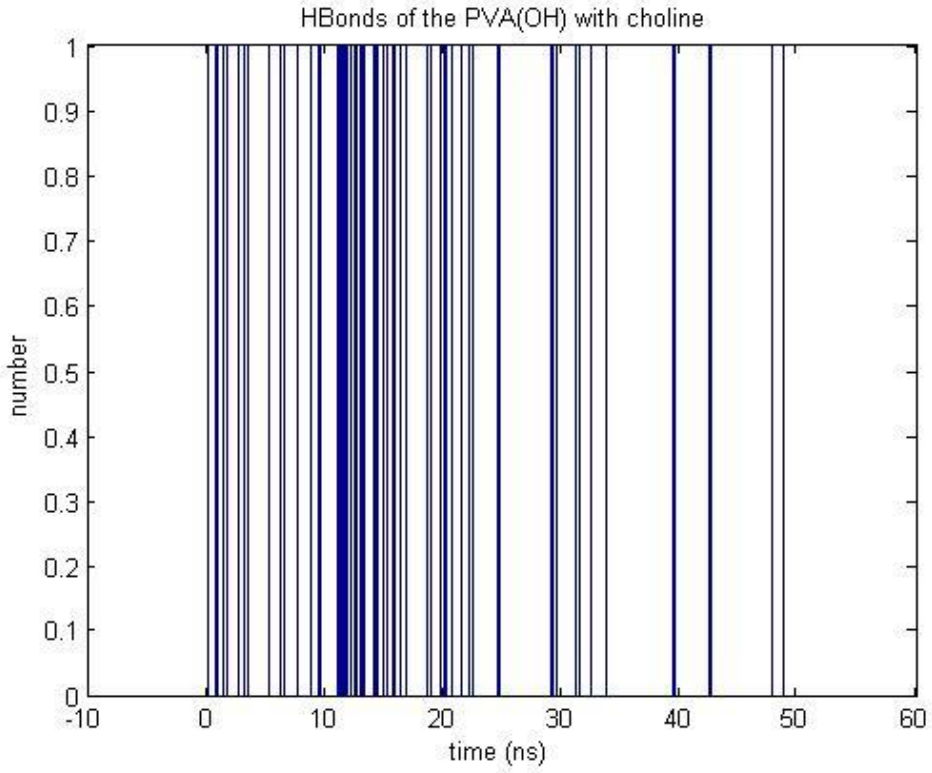

Figure 80: Hydrogen bond analysis between PVA (OH) and choline group of the DPPC lipid bilayer for 50ns.

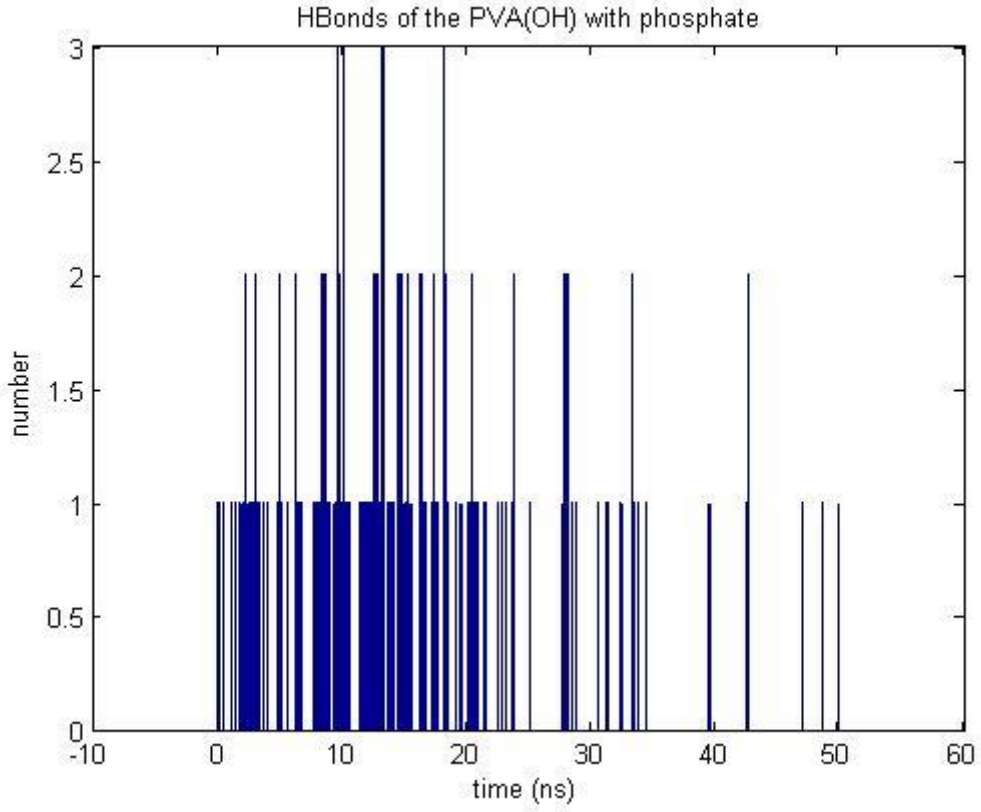

Figure 81: Hydrogen bond analysis between PVA (OH) and phosphate group of the DPPC lipid bilayer for 50ns.

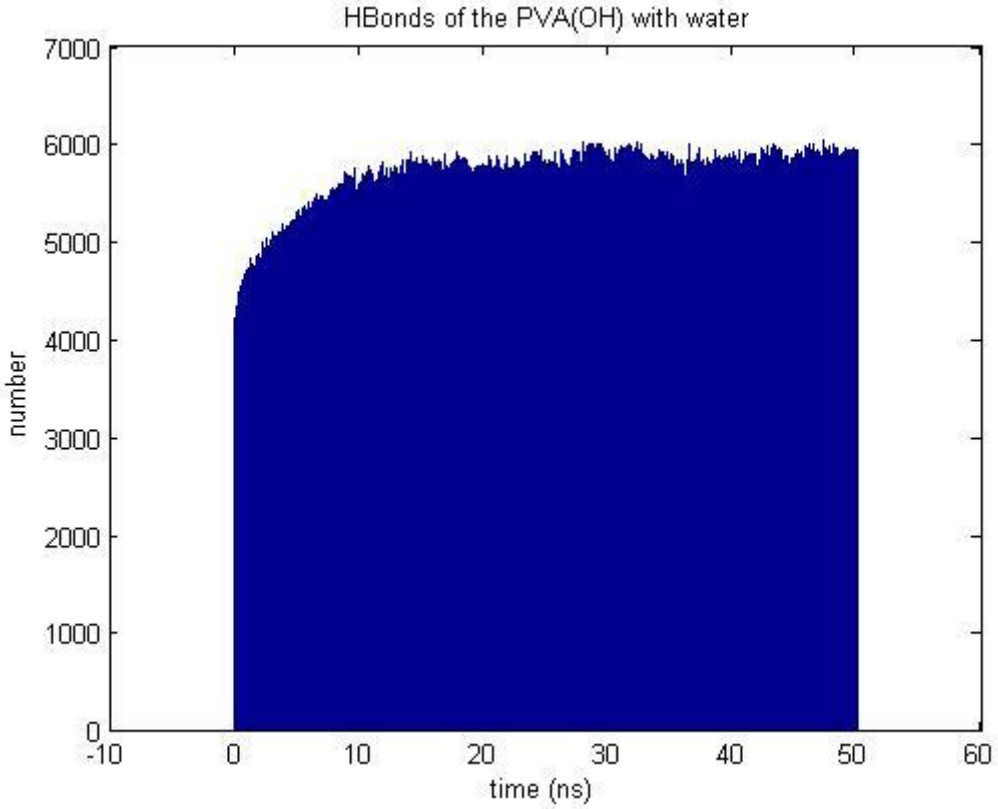

Figure 82: Hydrogen bond analysis between PVA (OH) and water phase of the DPPC lipid bilayer for 50ns.

MD simulations of the polyarabic-coated magnetite nanoparticle (MAG-ARA) are also performed for 50ns in the presence of a DPPC lipid bilayer in order to study the positioning of the nanoparticle in the bilayer and the interactions of polyarabic acid in atomic-level detail. MAG-ARA was initially placed in the water phase at 5 Å away from the lipid bilayer. Polyarabic acid is a branched polysaccharide consisting of L-arabinose, D-galactose, L-rhamnose and D-glucuronic acid in the ratio 3:3:1:1. It is evident from the simulations that MAG-ARA shows a strong preference for the membrane environment and within the first 10ns it starts interacting with the polar headgroups of the lipid bilayer. However, not all saccharides are equally interacting with the phospholipid headgroups. Analysis of the hydrogen bonds between the MAG-ARA and the phosphate groups shows that D-galactose and L-arabinose interact preferentially with the phosphate and choline groups and perform 2 and 1 hydrogen bonds on average during the simulation time, respectively. No internalization is observed during the simulation time. Our conclusions are consistent with the experimental results.

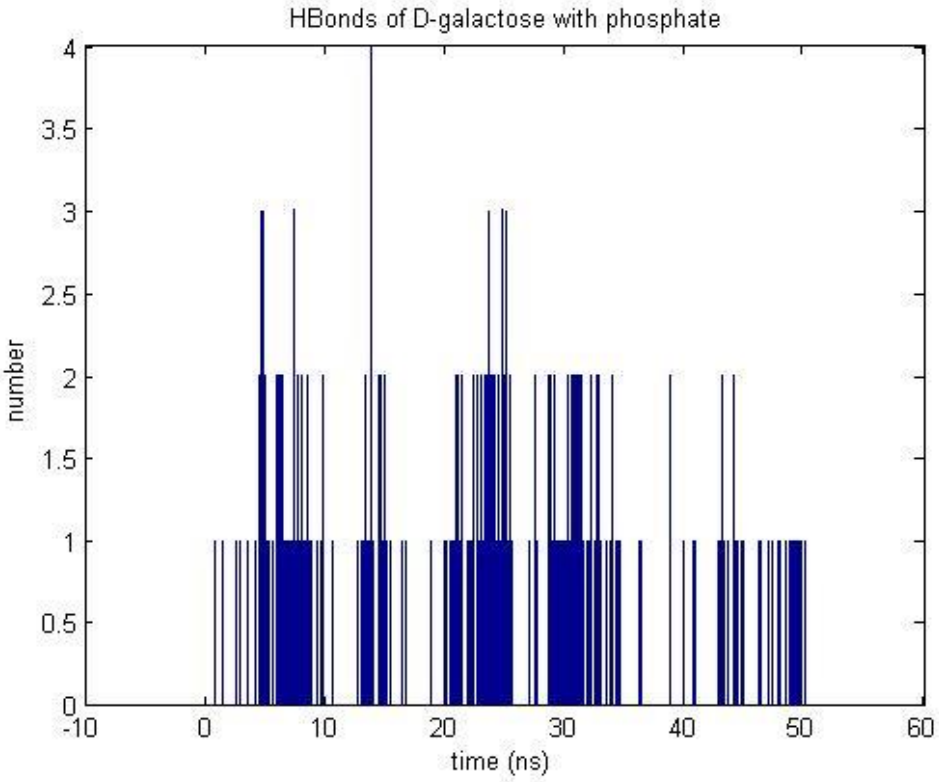

Figure 83: Hydrogen bond analysis between D-galactose and phosphate group of the DPPC lipid bilayer for 50ns.

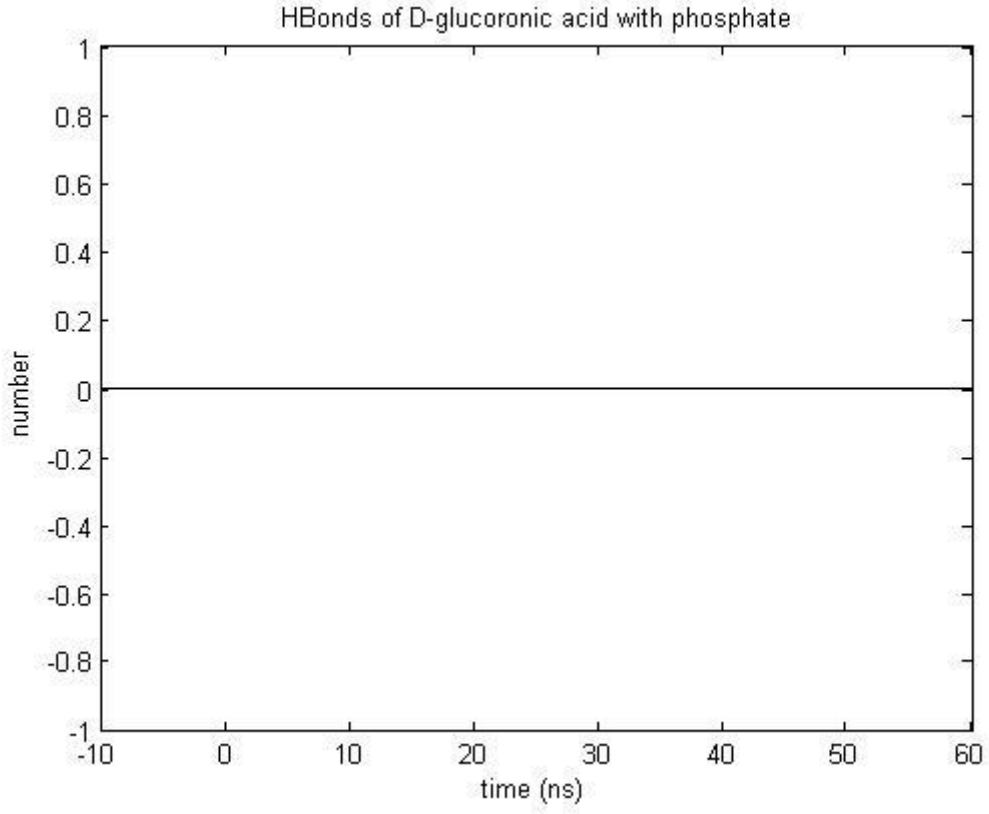

Figure 84: Hydrogen bond analysis between D-glucoronic acid and phosphate group of the DPPC lipid bilayer for 50ns.

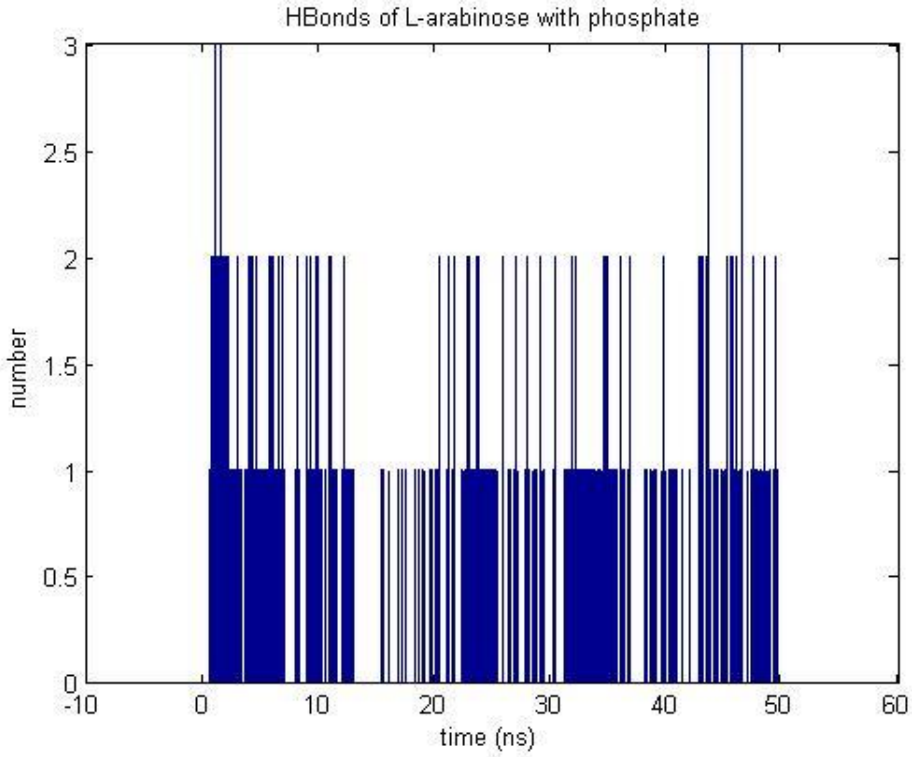

Figure 85: Hydrogen bond analysis between L-arabinose and phosphate group of the DPPC lipid bilayer for 50ns.

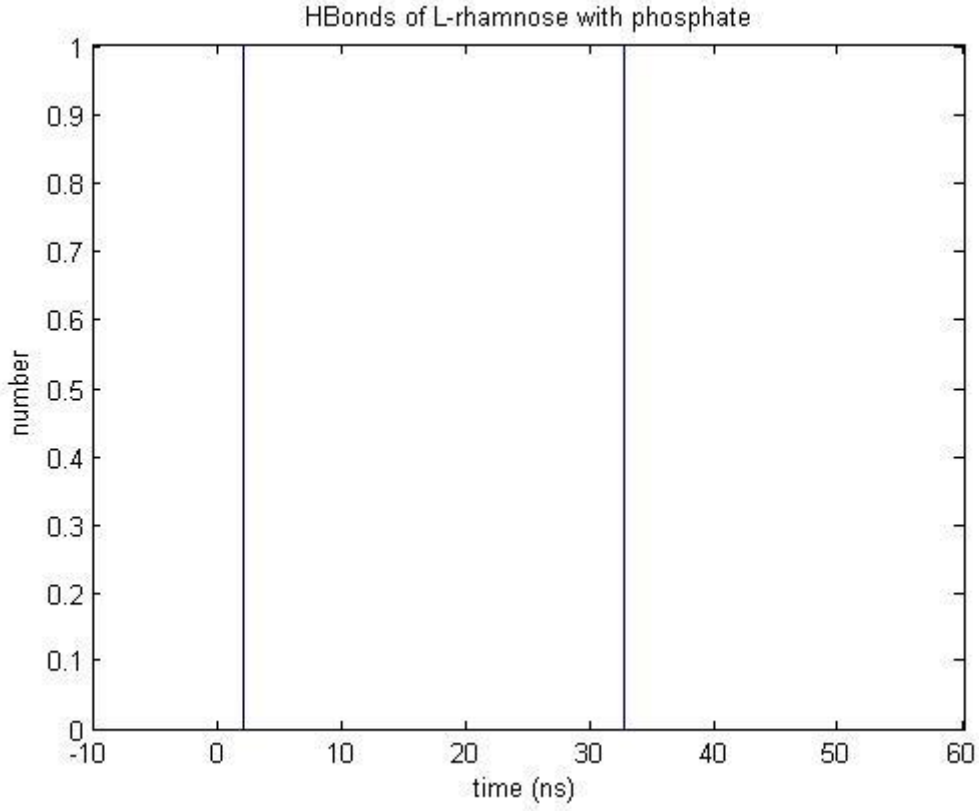

Figure 86: Hydrogen bond analysis between L-rhamnose and phosphate group of the DPPC lipid bilayer for 50ns.

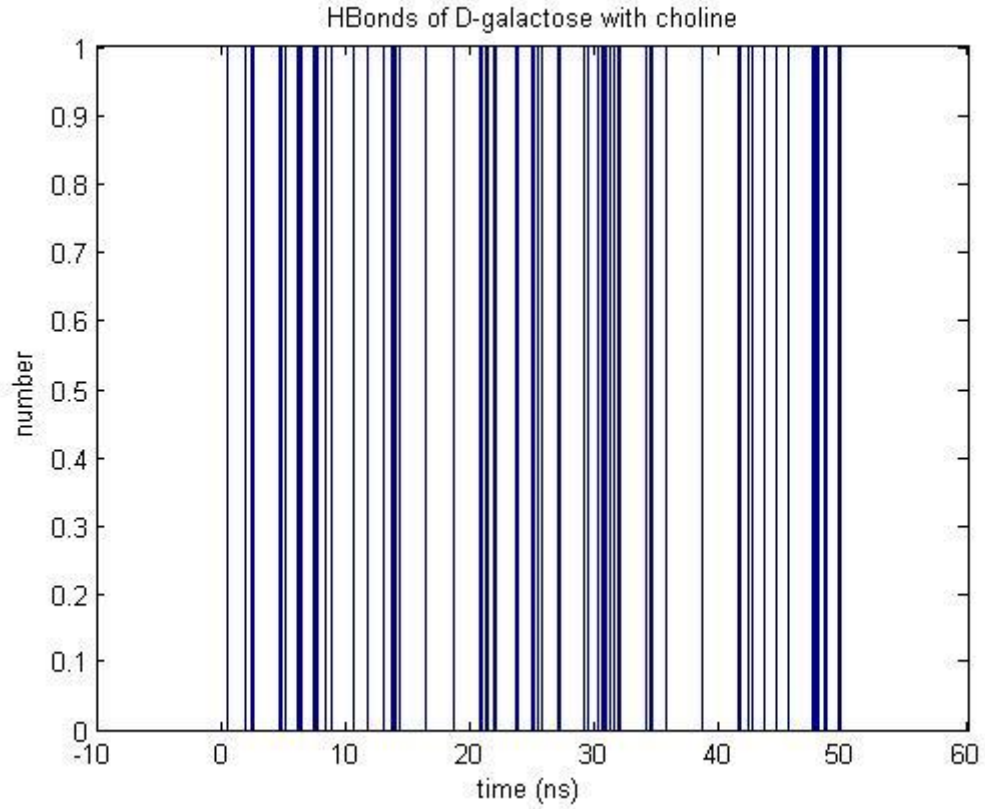

Figure 87: Hydrogen bond analysis between D-galactose and choline group of the DPPC lipid bilayer for 50ns.

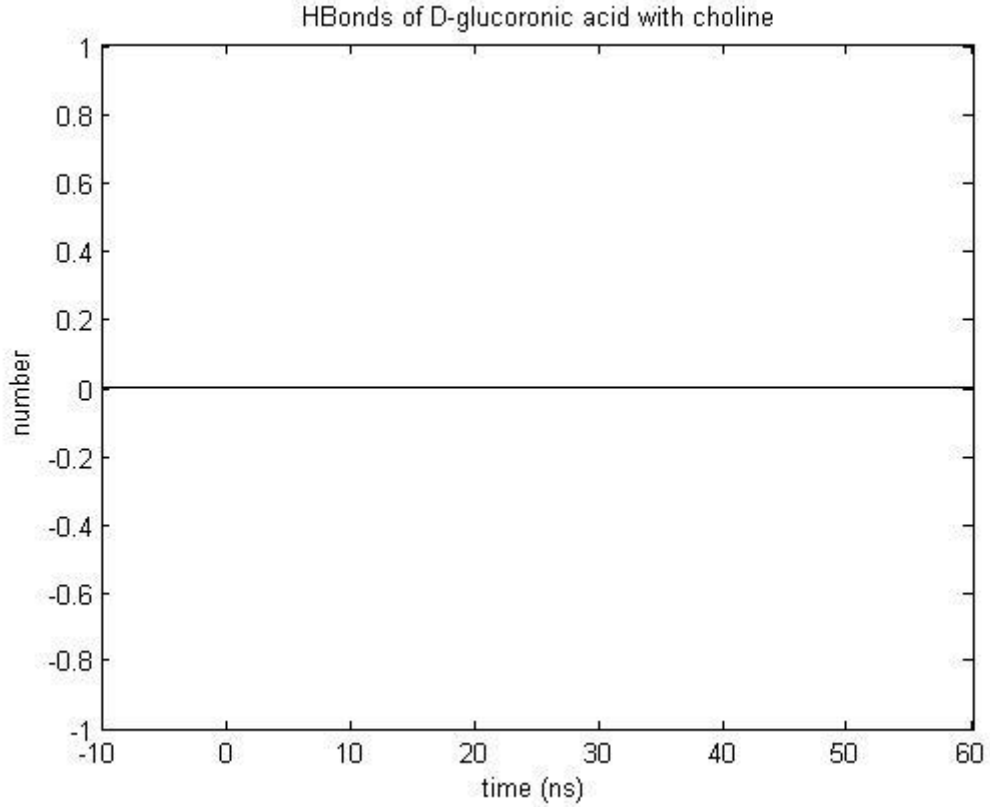

Figure 88: Hydrogen bond analysis between D-glucoronic acid and choline group of the DPPC lipid bilayer for 50ns.

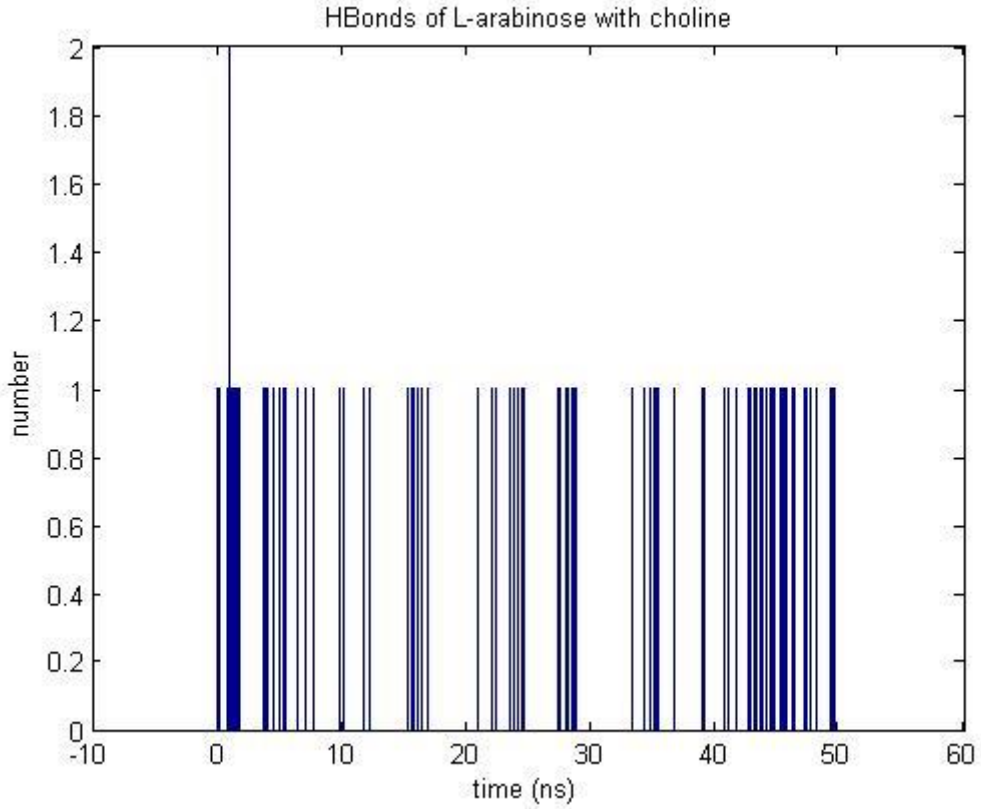

Figure 89: Hydrogen bond analysis between L-arabinose and choline group of the DPPC lipid bilayer for 50ns.

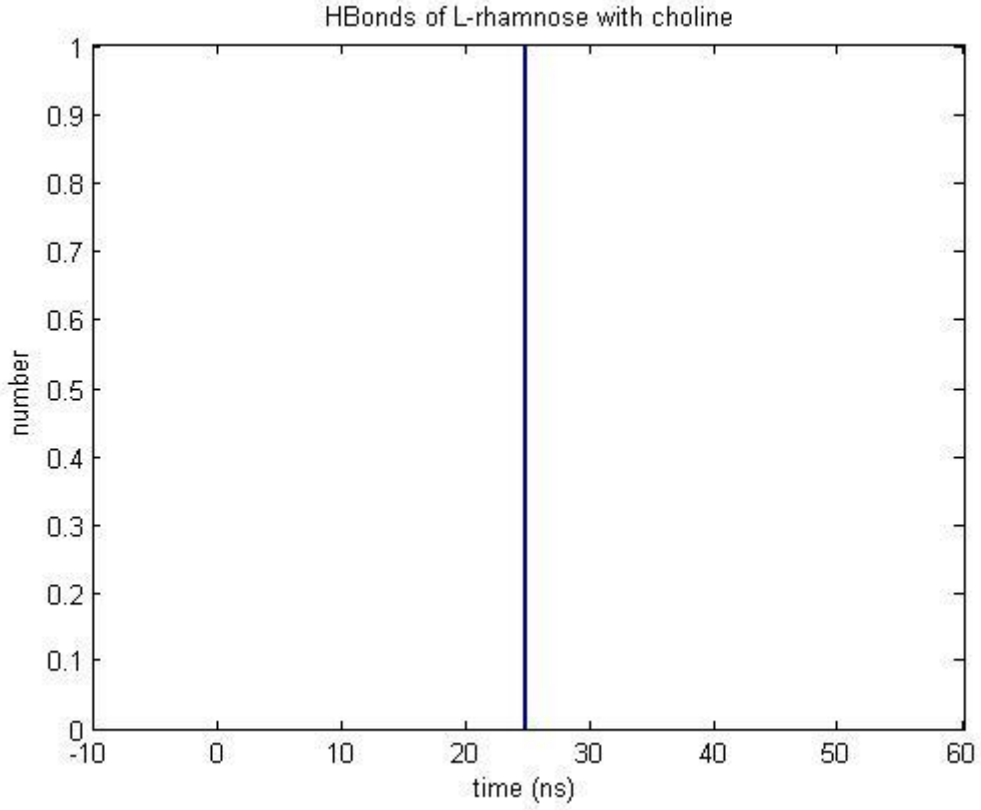

Figure 90: Hydrogen bond analysis between L-rhamnose and choline group of the DPPC lipid bilayer for 50ns.

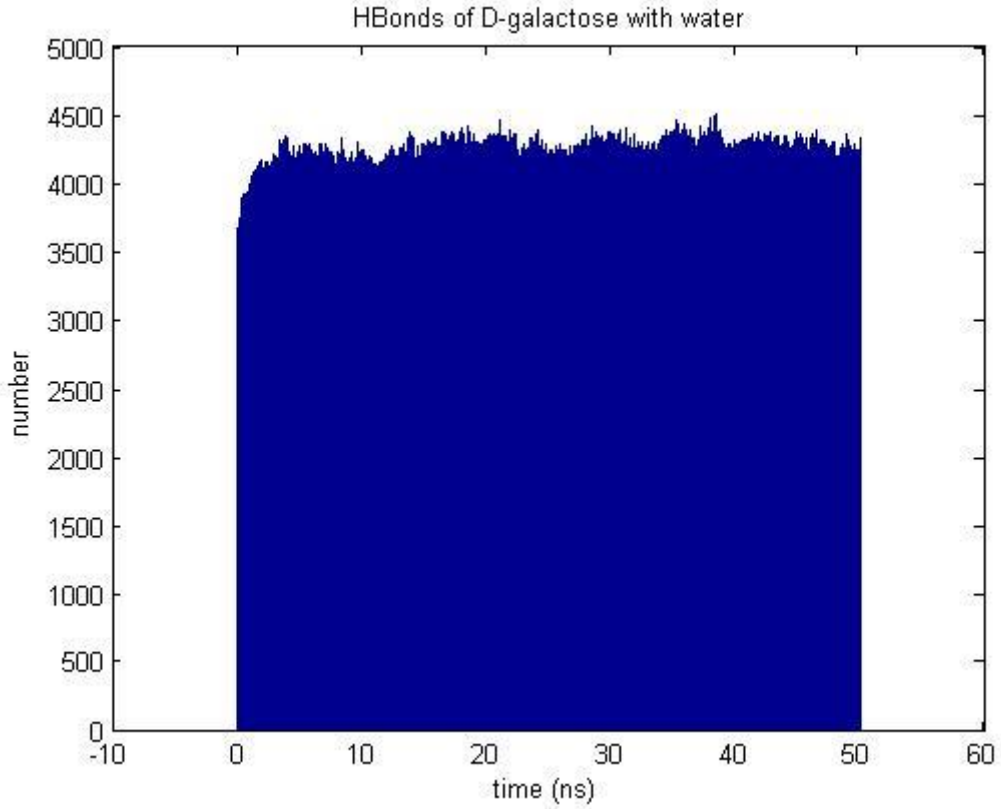

Figure 91: Hydrogen bond analysis between D-galactose and water for 50ns.

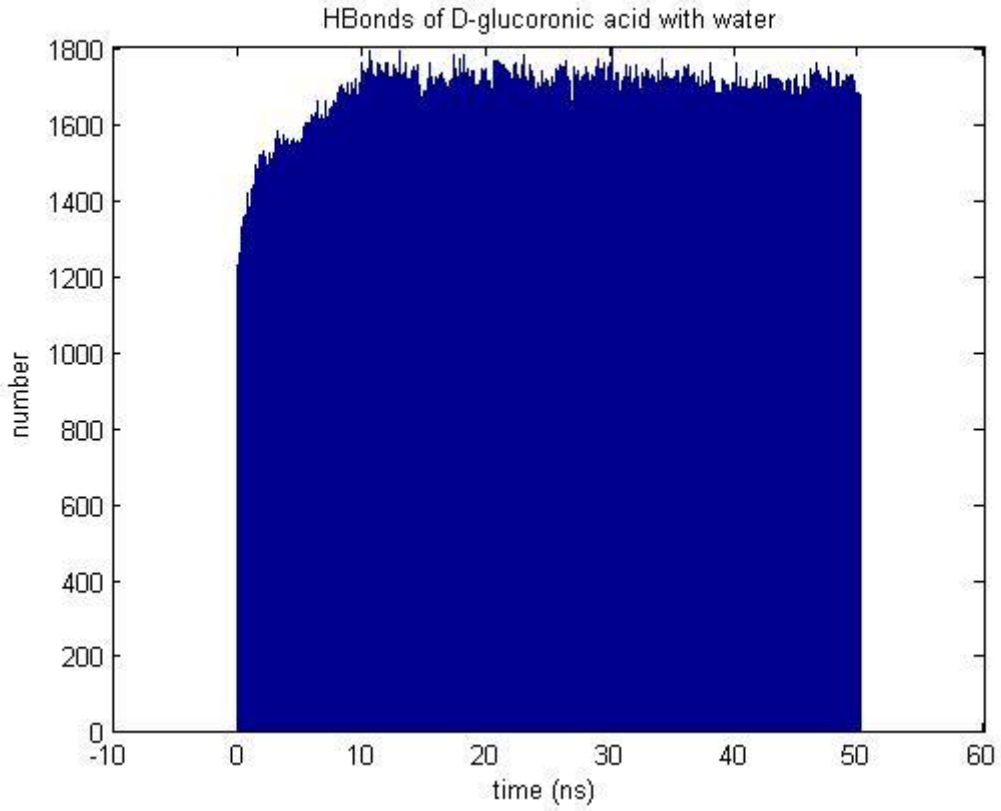

Figure 92: Hydrogen bond analysis between D-glucoronic acid and water for 50ns.

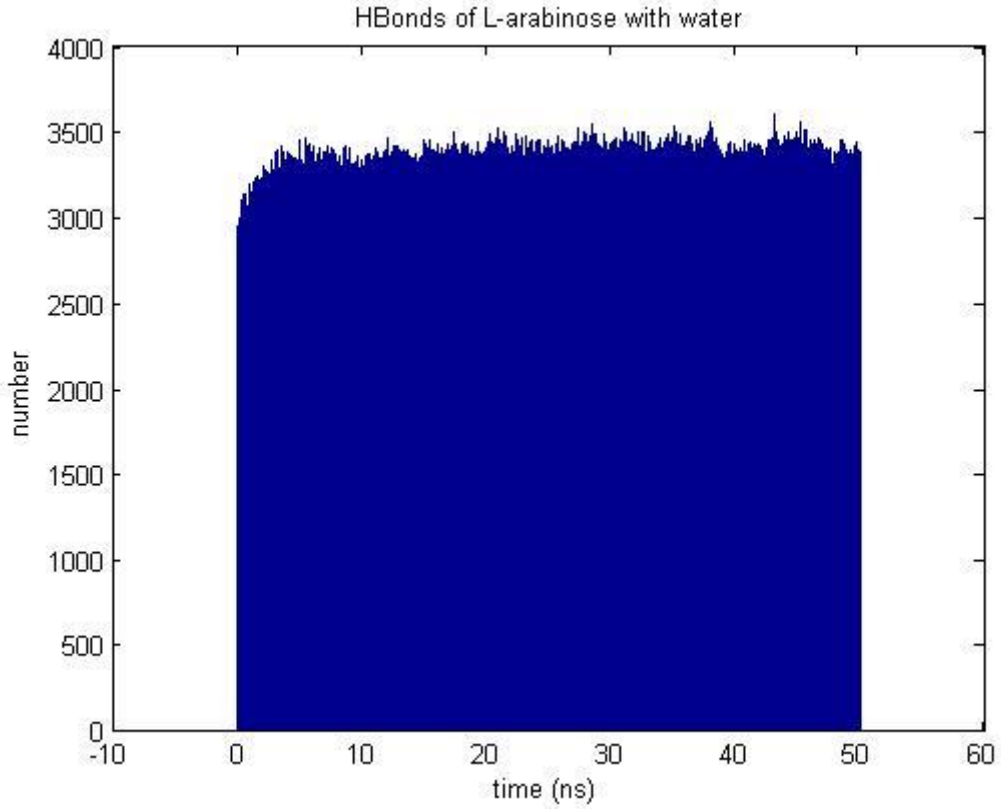

Figure 93: Hydrogen bond analysis between L-arabinose and water for 50ns.

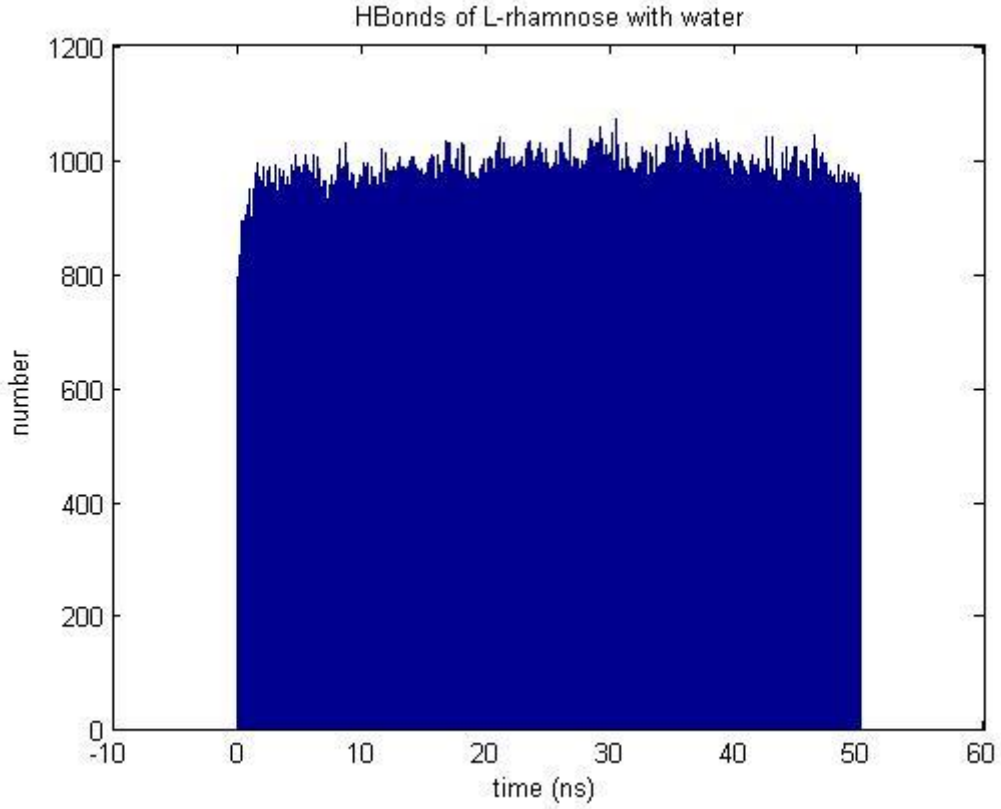

Figure 94: Hydrogen bond analysis between L-rhamnose and water for 50ns.

The hydrogen bond interactions of the Polyarabic acid saccharides with the phospholipid headgroups of the lipid bilayer are shown in Figures 95-97 after 50ns of MD simulations in the NPT ensemble.

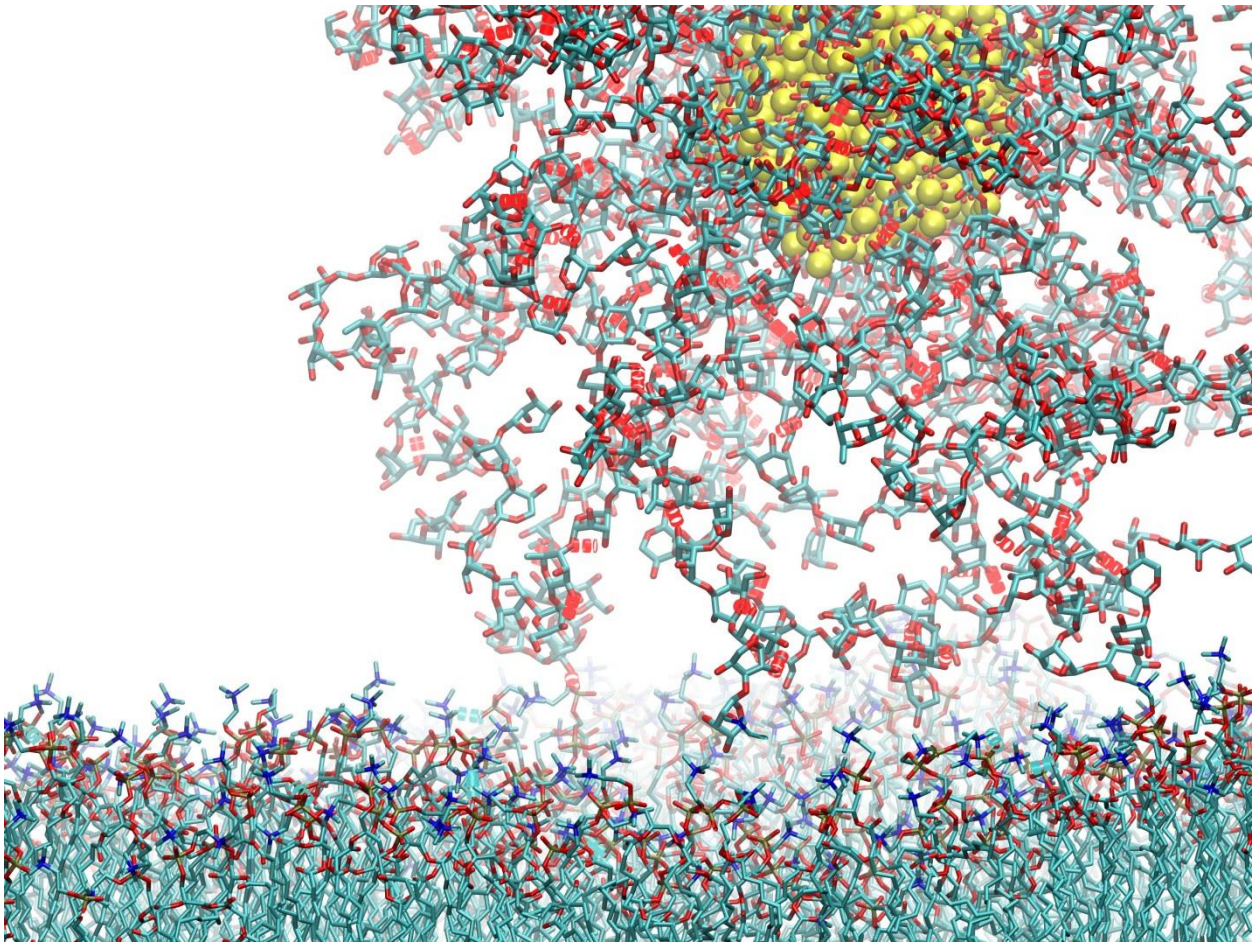

Figure 95: Hydrogen bond representation between different Polyarabic acid saccharides and the phospholipid headgroups of the lipid bilayer after 50ns of MD simulation (NPT ensemble) using NAMD. Visualization performed with VMD. The MNP core is shown in yellow.

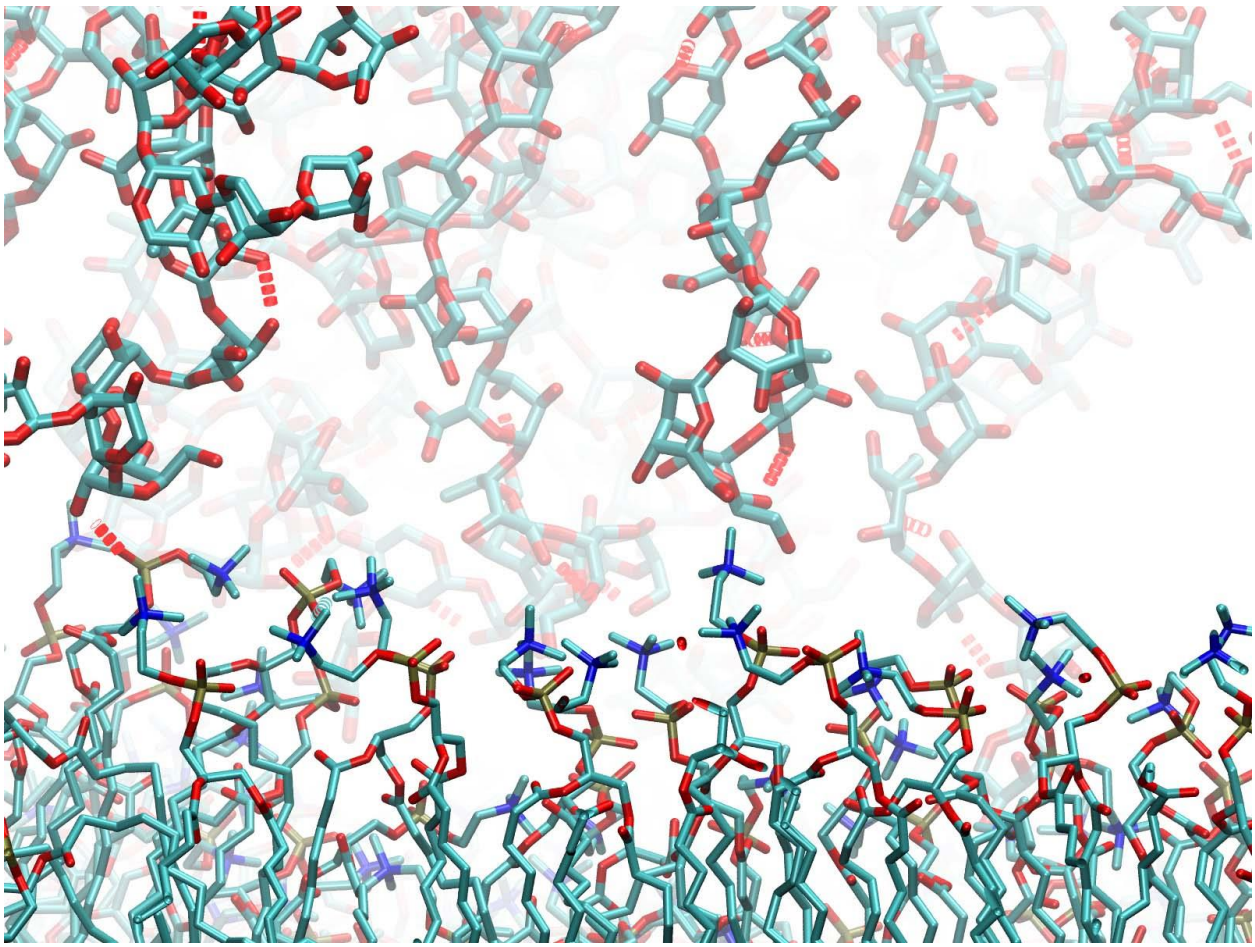

Figure 96: A closer visualization using VMD of hydrogen bond interactions between different Polyarabic acid saccharides and the phospholipid headgroups of the lipid bilayer after 50ns of MD simulation (NPT ensemble) using NAMD.

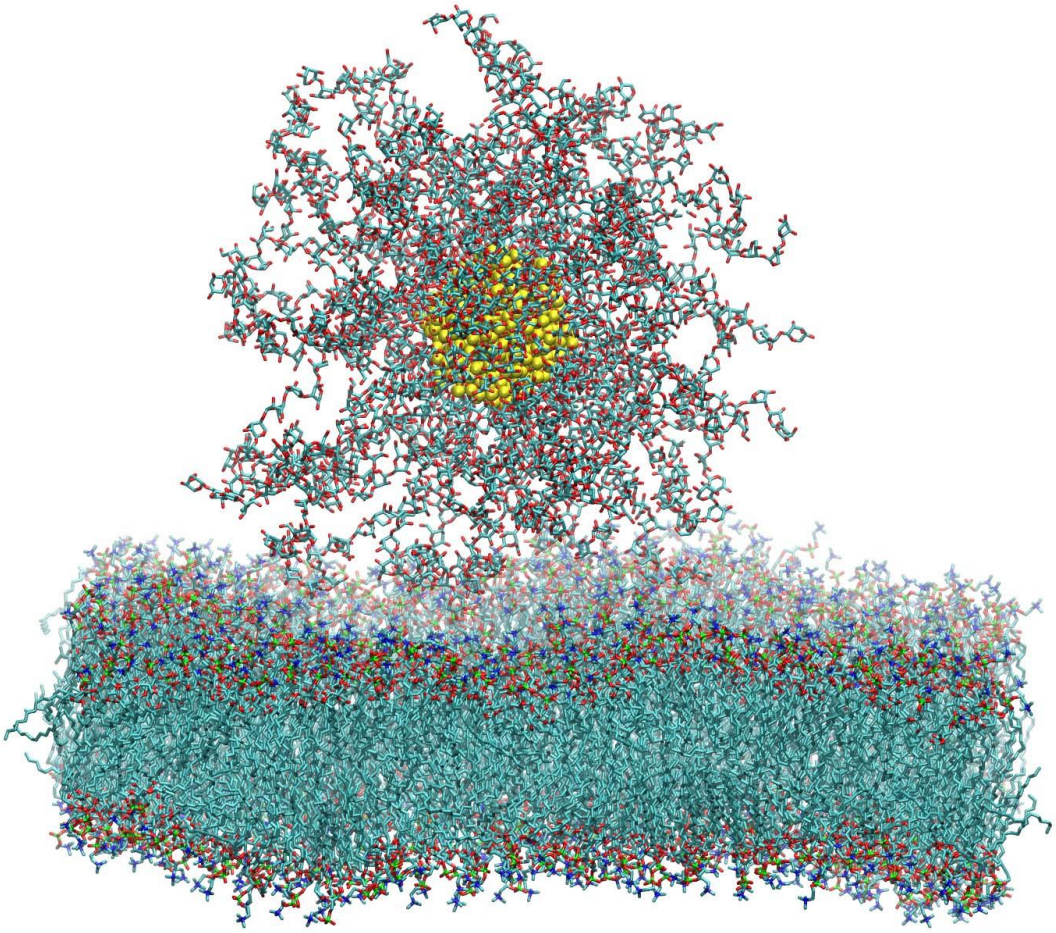

Figure 97: Last VMD snapshot of the MAG-ARA system at the water phase of the lipid bilayer after 50ns of MD simulation run (NPT ensemble) using NAMD.

3.8 Benchmarks and scaling

Molecular Dynamics simulations were performed on the ARIS supercomputer at GRNET (Greek Research and Technology Network) in Athens (https://hpc.grnet.gr/). The system comprises 426 nodes, equipped with latest HPC oriented x86_64 CPU technologies, providing power efficiency.

ARIS	
Architecture	x86-64
Compute Nodes	
System	IBM NeXtScale nx360 M4
Total number of nodes	426
Total number of cores	8520
Total ammount of RAM [TByte]	27
Total Linpack Performance [TFlop/s]	180
Components	
Processor Type	Ivy Bridge - Intel Xeon E5-2680v2
Nominal Frequency [GHz]	2.8
Processors per Node	2
Cores per Processor	10
Cores per Node	20
Hyperthreading	OFF
Memory	
Memory per Node [GByte]	64 (57 usable)
Interconnect	
Technology	Infiniband FDR10
Topology	Fat tree
Bandwidth	56 Gb/s
Storage	
Type	IBM GPFS
Size [PByte]	1
Bandwidth	5 GB/s
System Sofware	
Operating system	RedHat Linux 6.6
Batchsystem	SLURM
System Management	xCat IBM
Monitoring	Nagios, Ganglia

Figure 98: ARIS supercomputer Technical Info (http://doc.aris.grnet.gr/).

Table 7 describes the performance of GROMACS 5.0.6 on ARIS for the lipid-bilayer system consisting of 412,150 atoms, with the use of regular MD simulations for 100,000 steps during equilibration phase in the NPT ensemble. In table 8, number of 2 threads per MPI task is selected and the performance (ns/day) is given for 100, 500 and 1000 cores. Our results show significant scaling, up to 500 cores for GROMACS 5.0.6 making ARIS supercomputer a suitable resource for our study purposes. With this scaling behavior we can achieve production of approximately ~50-120 ns/day for our systems.

Table 7: GROMACS 5.0.6 performance on ARIS supercomputer infrastructure

Performance			
#cores	#nodes	#threads per MPI thread	ns/day
100	5	1	11.328
500	25	1	49.523
1000	50	1	74.807
2000	100	1	120.397
3000	150	1	125.799
4000	200	1	53.578

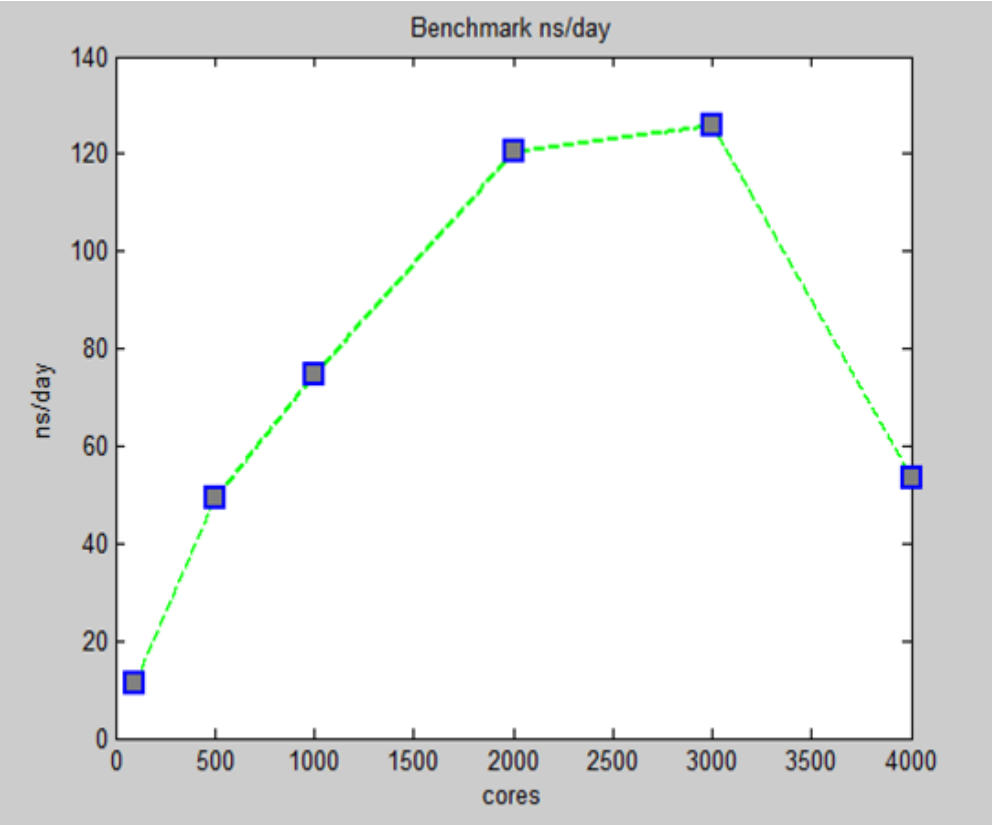

Figure 99: ns/day of MD simulations of lipid bilayer system using ARIS resources.

Table 8: GROMACS 5.0.6 performance on ARIS supercomputer infrastructure (Pure MPI)

Performance (Pure MPI)			
#cores	#nodes	#threads per MPI thread	ns/day
100	5	2	21.539
500	25	2	84.917
1000	50	2	93.180

4. CONCLUSIONS

In recent years, nanotechnology has demonstrated enormous promise to overcome the problems of conventional chemotherapeutic agents used in the treatment of cancer. Significant efforts have been lately dedicated to grow multi-functional theranostics nanosystems for both cancer diagnosis and therapy that can transport medicines exclusively to tumours and at the same time observe their therapeutic reaction by picturing the tumour legions in the body [191-192]. In this respect, one important consideration in the study of such systems is the interaction of the NP with the cell membrane. NPs will unavoidably come in contact with both healthy and diseased cells and should therefore not pose any risks for healthy tissues. Because of the importance of this interaction, the nanoparticle-membrane interface has been investigated, both with theoretical and computational methods.

Magnetic nanoparticles (MNPs) in particular are key nanocarriers for theranostic applications in cancer because they can be manipulated using a magnetic field and directed to the diseased site. MNPs are comprised of metal oxide cores commonly magnetite (Fe_3O_4) or TiO_2. These metal oxides grow in nature with characteristic external shapes of the individual crystal or crystal group, called crystal habits. Crystal habits depend each time on the minimum free energy surfaces of the crystal growing planes. In the past decades, significant attempts have been made to calculate accurately the growth morphology of crystals, although, it remains a difficult task. The complexity of comprehending the crystal growth phenomena occurs as a result of multifaceted interactions between diverse processes, observed on the different wide scales of time and length [164]. The crystal shape directed each time by the individual crystal habit, imposes directly on the parting efficiency and the stability of crystalline chemicals, the bioavailability, their behavior in biomedical applications (efficient delivery of drug molecules etc.) [162]. Therefore, the understanding of the growth behavior and morphological qualities of the molecular crystals is of vital significance in the comprehension and use of a variety of their physicochemical properties [156, 162].

In this study, a crystal morphology toolbox was created consisting of different algorithms. Initially, an algorithm was implemented for creating spherical nanoparticles based on the radius of the NP, and the radius of smaller spheres, that cover the surface of the nanoparticle. Next, the construction of an appropriate structure for magnetite nanoparticle (based on its crystal habit or Wulff morphology) [159], using computational approaches, was achieved. The magnetite NP was further simulated using MD simulations in vacuum and in water. Our results indicate a stable structure of the NP. The construction of the magnetite NP was then generalized by developing an algorithm that constructs different morphologies for a given crystal based on its preferred growing planes, the Miller indices, and a user-defined size of the crystal.

Coating of the NPs with suitable ligands can enhance their biodistribution and provide then with suitable properties for their efficient uptake. Therefore, an algorithm was developed to coat the Fe_3O_4 MNP core with polyvinyl alcohol (PVA) and polyarabic acid (ARA) ligands. The user is given the option to adjust the length of the molecular chains that can be connected to specific Fe octahedral surface atoms. For modeling the cell membrane, a dipalmitoylphosphatidylcholine (DPPC) lipid bilayer was built.

Finally, in order to observe the interactions between coated MNPs and the lipid bilayer, we have performed MD simulations using, the GROMACS simulation package, version 5.0.6 [183]. The topology files of the system were constructed dynamically using our in-house code, which included partial charges for magnetite and PVA and ARA chains, and all the information needed for bonds, angles and dihedrals of the system atoms.

The two model MNPs were placed in the water phase of the lipid bilayer system and atomistic MD simulations were performed in order to describe the nanoparticle-membrane interactions in atomic-level detail.

From our simulations, it is evident that MAG-ARA preferentially interacts by the lipid head groups compared to MAG-PVA and it can be used for further simulation and analysis. Within the first 10ns it starts interacting with the polar headgroups of the lipid bilayer. However, not all saccharides are equally interacting with the phospholipid headgroups. Analysis of the hydrogen bonds between the MAG-ARA and the phosphate groups shows that D-galactose and L-arabinose interact preferentially with the phosphate group and perform 2 hydrogen bonds on average over the simulation time, respectively. On the other hand, MAG-PVA shows preferential solvation from the water phase. No internalization is observed during the simulation time for both systems. Our results are in agreement with the available experimental data from our collaborators deriving conclusions from the distinct interactions between different ligand coating of the NP and the membrane.

FUTURE PERSPECTIVES

Nanoparticle-based systems have enormous potential in improving cancer diagnosis, detection, imaging, and treatment [193]. NPs may soon resolve issues of conventional cancer therapies such as nonspecific targeting, low therapeutic effectiveness, unpleasant side effects, and drug resistance [194]. The capacity of NPs to be customized for a patient-based medicine strategy portrays them as the perfect vehicles for the treatment of cancer. Generally, NPs with multicomponent structures permit pattern flexibility in drug delivery of poorly water soluble molecules, while conveying the capacity to prevail over biological barriers and selectively target desired sites within the body [10].

Due to the complexities of the drug delivery process and the large amount of uncertainty involved, computational modeling is extensively applied for NP design in order to elucidate atomic-level interactions that are out of reach for conventional experimental techniques. Our study, as a molecular modeling process, includes the construction of two coated nanoparticles and their modeling at the interface of a model cell membrane. Although important physicochemical interactions were modeled and quantified at the nano-bio interface, spontaneous NP translocation across the membrane was not observed. This could be attributed to the short simulation time (50 ns) of the system. As a future direction, simulations could run for additional time deriving important insights into the physicochemical properties that govern the interactions between different classes of MNPs and the membrane and allowing the analysis of a possible internalization process of the nanoparticle into the cell membrane.

The implementation of our software for constructing different crystal morphologies based on the preferred growing planes and the user-defined size of the crystal is of crucial importance and can be used for various applications of modeling NP, not only for medical applications but also in materials science. In this thesis, the magnetite NP was constructed and modeled but the code could be used and extended to include NPs of any crystal size, shape, and morphology. The shape of crystals has a direct impact on the separation efficiency and the stability of crystalline chemicals, the bioavailability or the effective delivery of drugs. The knowledge of the growth habits and morphological properties of the molecular crystals is of crucial importance in understanding and exploiting many of their physicochemical properties.

A future work direction is the extension of the algorithm for computing the preferred growing planes using some energetic or other type of simulations. The preferred planes and the unit cell of any periodic crystal given by the user would allow the construction of any crystal morphology. Currently, the crystal habits for the construction of each NP using our crystal morphology tool are provided based on literature quantum chemical data. However, our code could be further extended to predict the crystal habits based on the Donnay-Hacker rules [201]. Finally, our software program could be extended to include coated NPs through the dynamic attachment of custom molecules/ligands to the constructed crystal.

These future directions could lead to a complete computational toolbox, able to make a link between the macroscopic morphology and the atomistic structure for any periodic crystal and can be used for various biomedical or materials design applications.

BIBLIOGRAPHY

[1] K. H. Bae, H. J. Chung, and T. G. Park, (2011). Nanomaterials for cancer therapy and imaging. Mol Cells, 31(4), 295-302. doi:10.1007/s10059-011-0051-5.

[2] N. Wiradharma, Y. Zhang, S. Venkataraman, J. L. Hedrick, and Y. Y. Yang. (2009). Self-assembled polymer nanostructures for delivery of anticancer therapeutics. Nano Today, 4(4), 302-317. doi:10.1016/j.nantod.2009.06.001

[3] H. Maeda. (2012). Vascular permeability in cancer and infection as related to macromolecular drug delivery, with emphasis on the EPR effect for tumor-selective drug targeting. Proceedings of the Japan Academy, Series B, 88(3), 53-71. doi:10.2183/pjab.88.53

[4] L. Jabr-Milane, L. V. Vlerken, H. Devalapally, D. Shenoy D, S. Komareddy, M. Bhavsar, and M. Amiji. (2008). Multi-functional nanocarriers for targeted delivery of drugs and genes. J. Control. Release, 130(2), 121-128. doi:10.1016/j.jconrel.2008.04.016

[5] M. Pulkkinen, J. Pikkarainen, T. Wirth, T. Tarvainen, V. Haapaaho, H. Korhonen, K. Jarvinen. (2008). Three-step tumor targeting of paclitaxel using biotinylated PLA-PEG nanoparticles and avidin–biotin technology: Formulation development and in vitro anticancer activity. Eur J Pharm Biopharm, 70(1), 66-74. doi:10.1016/j.ejpb.2008.04.018

[6] Q. Weili, W. Bochu, W. Yazhou, Y. Lichun, Z. Yiqiong, and S. Pengyu. (2010). Cancer Therapy Based on Nanomaterials and Nanocarrier, Systems Journal of Nanomaterials Volume 2010, Article ID 796303, 9 pages, doi:10.1155/2010/796303

[7] S. P. Egusquiaguirre, M. Igartua, R. M. Hernández, and J. L. Pedraz. (2012). Nanoparticle delivery systems for cancer therapy: advances in clinical and preclinical research. Clinical and Translational Oncology, 14(2), 83-93. doi:10.1007/s12094-012-0766-6

[8] K. Smriti, L. Pratyush, G. Shweta. (2011). Nanoemulsions in Cancer Therapy. Indian J Pharm Sci, 2013; 3(2): 124-133.

[9] N. Bertrand, J. Wu, X. Xu, N. Kamaly, and O. C. Farokhzad. (2014). Cancer Nanotechnology: The impact of passive and active targeting in the era of modern cancer biology. Adv. Drug Deliv. Rev., 66, 2–25. http://doi.org/10.1016/j.addr.2013.11.009

[10] Y. Zhang, Y. Huang, and S. Li. (2014). Polymeric Micelles: Nanocarriers for Cancer-Targeted Drug Delivery. AAPS PharmSciTech, 15(4), 862–871. http://doi.org/10.1208/s12249-014-0113-z

[11] L. Cabeza, R. Ortiz, J. L. Arias, J. Prados, M. A. Ruiz Martínez, J. M. Entrena, C. Melguizo. (2015). Enhanced antitumor activity of doxorubicin in breast cancer through the use of poly(butylcyanoacrylate) nanoparticles. International Journal of Nanomedicine, 10, 1291–1306. http://doi.org/10.2147/IJN.S74378

[12] S. Salmaso, and P. Caliceti. (2013). Stealth Properties to Improve Therapeutic Efficacy of Drug Nanocarriers. Journal of Drug Delivery, 2013, 374252. http://doi.org/10.1155/2013/374252

[13] N. Tang, G. Du, N. Wang, C. Liu, H. Hang, and W. Liang. (2007). Improving Penetration in Tumors With Nanoassemblies of Phospholipids and Doxorubicin. JNCI Journal of the National Cancer Institute, 99(13), 1004-1015. doi:10.1093/jnci/djm027

[14] J. W. Nichols, and Y. H. Bae. (2012). Odyssey of a cancer nanoparticle: from injection site to site of action. Nano Today, 7(6), 606–618. http://doi.org/10.1016/j.nantod.2012.10.010

[15] S. Sahoo, S. Parveen, and J. Panda. (2007). The present and future of nanotechnology in human health care. Nanomedicine: Nanotechnology, Biology and Medicine, 3(1), 20-31. doi:10.1016/j.nano.2006.11.008

[16] R. Rachana, and D. Snehal. (2013). Biomedical Approach of Nanomaterials for Drug Delivery. International Journal of Chemistry and Chemical Engineering. ISSN 2248-9924 Volume 3, Number 2 (2013), pp. 95-100

[17] J. F. Honek, A. Francq, and A. J. Carty. (2010). Research Spotlight: Bionanotechnology: small can have a big impact in the medical sciences: a WIN-win situation. Part 1. Future Medicinal Chemistry, 2(10), 1515-1522. doi:10.4155/fmc.10.240

[18] E. Blanco, A. Hsiao, A. P. Mann, M. G. Landry, F. Meric-Bernstam, and M. Ferrari. (2011). Nanomedicine in cancer therapy: Innovative trends and prospects. Cancer Science, 102(7), 1247-1252. doi:10.1111/j.1349-7006.2011.01941.x

[19] P. Ma, and R. J. Mumper. (2013). Anthracycline Nano-Delivery Systems to Overcome Multiple Drug Resistance: A Comprehensive Review. Nano Today, 8(3), 313–331. http://doi.org/10.1016/j.nantod.2013.04.006

[20] J. Safari, and Z. Zarnegar. (2014). Advanced drug delivery systems: Nanotechnology of health design A review. Journal of Saudi Chemical Society,18(2), 85-99.

[21] M. Rezaei-Kelishadi, M. Nuri, Z. Erfani, A. Palizban, and R. Parandin, R. (2014). Control, Management and Treatment of Diabetes Using Modern Drug Delivery Systems and Special Properties of Nanoparticles. Journal of Biology and Todays World,3(9). doi:10.15412/j.jbtw.01030905

[22] F. Cheng, C. Su, P. Wu, and C. Yeh, C. (2010). Multifunctional polymeric nanoparticles for combined chemotherapeutic and near-infrared photothermal cancer therapy in vitro and in vivo. Chemical Communications,46(18), 3167. doi:10.1039/b919172k

[23] J. Wolfram, M. Zhu, Y. Yang, J. Shen, E. Gentile, D. Paolino, Y. Zhao. (2015). Safety of nanoparticles in medicine. Current Drug Targets, 16(14), 1671–1681.

[24] D. B. Chithrani, S. Jelveh, F. Jalali, M. V. Prooijen, C. Allen, R. G. Bristow, D. A. Jaffray. (2010). Gold Nanoparticles as Radiation Sensitizers in Cancer Therapy. Radiation Research,173(6), 719-728. doi:10.1667/rr1984.1

[25] H. D. Han, L. S. Mangala, J. W. Lee, M. M. K. Shahzad, H. S. Kim, D. Shen, A. K . Sood (2010). Targeted Gene Silencing Using RGD-Labeled Chitosan Nanoparticles. Clinical Cancer Research : An Official Journal of the American Association for Cancer Research, 16(15), 3910–3922. http://doi.org/10.1158/1078-0432.CCR-10-0005

[26] Q. Mu, M. Jeon, M.-H. Hsiao, V. K. Patton, K. Wang, O. W. Press, and M. Zhang. (2015). Stable and Efficient Paclitaxel Nanoparticles for Targeted Glioblastoma Therapy. Advanced Healthcare Materials, 4(8), 1236–1245. http://doi.org/10.1002/adhm.201500034

[27] A. Lamprecht, and J. Benoit. (2006). Etoposide nanocarriers suppress glioma cell growth by intracellular drug delivery and simultaneous P-glycoprotein inhibition. Journal of Controlled Release, 112(2), 208-213. doi:10.1016/j.jconrel.2006.02.014

[28] O. Ozay, A. Akcali, M. T. Otkun, C. Silan, N. Aktas, and N.Sahiner. (2010). P(4-VP) based nanoparticles and composites with dual action as antimicrobial materials. Colloids and Surfaces B: Biointerfaces,79(2), 460-466. doi:10.1016/j.colsurfb.2010.05.013

[29] S. Parveen, R. Misra, and S. K. Sahoo. (2012). Nanoparticles: a boon to drug delivery, therapeutics, diagnostics and imaging. Nanomedicine: Nanotechnology, Biology and Medicine,8(2), 147-166. doi:10.1016/j.nano.2011.05.016

[30] C. D. Medley, J. E. Smith, Z. Tang, Y. Wu, S. Bamrungsap, and W. Tan. (2008). Gold Nanoparticle-Based Colorimetric Assay for the Direct Detection of Cancerous Cells. Analytical Chemistry, 80(4), 1067-1072. doi:10.1021/ac702037y

[31] S. Ganta, M. Talekar, A. Singh, T. P. Coleman, and M. M. Amiji. (2014). Nanoemulsions in Translational Research—Opportunities and Challenges in Targeted Cancer Therapy. AAPS PharmSciTech, 15(3), 694–708. http://doi.org/10.1208/s12249-014-0088-9

[32] K. K. Jain. (2007). Applications of Nanobiotechnology in Clinical Diagnostics. Clinical Chemistry, 53(11), 2002-2009. doi:10.1373/clinchem.2007.090795

[33] T. D. Tran, S. D. Caruthers, M. Hughes, J. N. Marsh, T. Cyrus, P. M. Winter, G. M. Lanza. (2007). Clinical applications of perfluorocarbon nanoparticles for molecular imaging and targeted therapeutics. International Journal of Nanomedicine, 2(4), 515–526

[34] A. J. Mieszawska, W. J. M. Mulder, Z. A. Fayad, and D. P. Cormode. (2013). Multifunctional gold nanoparticles for diagnosis and therapy of disease. Molecular Pharmaceutics, 10(3), 831–847. http://doi.org/10.1021/mp3005885

[35] T. R. Pisanic, Y. Zhang, and T. H. Wang. (2014). Quantum Dots in Diagnostics and Detection: Principles and Paradigms. The Analyst, 139(12), 2968–2981. http://doi.org/10.1039/c4an00294f

[36] X. Mao, J. A. Phillips, H. Xu, W. Tan, L. Zeng, and G. Liu. (2009). Aptamer-Nanoparticle Strip Biosensor for Rapid and Sensitive Detection of Cancer Cells. Analytical Chemistry, 81(24), 10013. http://doi.org/10.1021/ac901889s

[37] M. Cordeiro, F. F. Carlos, P. Pedrosa, A. Lopez, and P. Baptista. (2016). Gold Nanoparticles for Diagnostics: Advances towards Points of Care. Diagnostics,6(4), 43. doi:10.3390/diagnostics6040043

[38] H. Jo, and C. Ban. (2016). Aptamer–nanoparticle complexes as powerful diagnostic and therapeutic tools. Experimental & Molecular Medicine, 48(5). doi:10.1038/emm.2016.44

[39] Y.-E. Choi, J.-W. Kwak, and J. W. Park. (2010). Nanotechnology for Early Cancer Detection. Sensors (Basel, Switzerland), 10(1), 428–455. http://doi.org/10.3390/s100100428

[40] K. M. Abu-Salah, M. M. Zourob, F. Mouffouk, S. A. Alrokayan, M. A. Alaamery, and A.A. Ansari. (2015). DNA-Based Nanobiosensors as an Emerging Platform for Detection of Disease. Sensors (Basel, Switzerland), 15(6), 14539–14568. http://doi.org/10.3390/s150614539

[41] F. Corsi, C. D. Palma, M. Colombo, R. Allevi, M. Nebuloni, S. Ronchi, D. Prosperi. (2009). Towards Ideal Magnetofluorescent Nanoparticles for Bimodal Detection of Breast-Cancer Cells. Small,5(22), 2555-2564. doi:10.1002/smll.200900881

[42] A. D. Escosura-Muñiz, C. Sánchez-Espinel, B. Díaz-Freitas, A. González-Fernández, M. M Costa, and A. Merkoçi. (2009). Rapid Identification and Quantification of Tumor Cells Using an Electrocatalytic Method Based on Gold Nanoparticles. Analytical Chemistry,81(24), 10268-10274. doi:10.1021/ac902087k

[43] P. M. Farias, B. S. Santos, and A. Fontes. (2009). Semiconductor Fluorescent Quantum Dots: Efficient Biolabels in Cancer Diagnostics. Micro and Nano Technologies in Bioanalysis Methods in Molecular Biology, 407-419. doi:10.1007/978-1-59745-483-4_27

[44] D. Brambilla, J. Nicolas, B. L. Droumaguet, K. Andrieux, V. Marsaud, P. Couraud, and P. Couvreur. (2010). Design of fluorescently tagged poly(alkyl cyanoacrylate) nanoparticles for human brain endothelial cell imaging. Chemical Communications,46(15), 2602. doi:10.1039/b924028d

[45] S. K. Nune, P. Gunda, P.K. Thallapally, Y.-Y. Lin, M. L. Forrest, and C. J. Berkland. (2009). Nanoparticles for biomedical imaging. Expert Opinion on Drug Delivery, 6(11), 1175–1194. http://doi.org/10.1517/17425240903229031

[46] E. C. Cho, C. Glaus, J. Chen, M. J. Welch, and Y. Xia. (2010). Inorganic nanoparticle-based contrast agents for molecular imaging. Trends in Molecular Medicine, 16(12), 561–573. http://doi.org/10.1016/j.molmed.2010.09.004

[47] J. Tan, N. Yang, Z. Hu, J. Su, J. Zhong, Y. Yang, Y. Zhao. (2016). Aptamer-Functionalized Fluorescent Silica Nanoparticles for Highly Sensitive Detection of Leukemia Cells. Nanoscale Research Letters, 11, 298. http://doi.org/10.1186/s11671-016-1512-8

[48] Z. Hu, J. Tan, Z. Lai, R. Zheng, J. Zhong, Y. Wang, X. Lu. (2017). Aptamer Combined with Fluorescent Silica Nanoparticles for Detection of Hepatoma Cells. Nanoscale Research Letters, 12, 96. http://doi.org/10.1186/s11671-017-1890-6

[49] M. Nurunnabi, K. J. Cho, J. S. Choi, K. M. Huh, and Y. K. Lee. (2010) Targeted near-IR QDs-loaded micelles for cancer therapy and imagingBiomaterials. 2010 Jul;31(20):5436-44. doi: 10.1016/j.biomaterials.2010.03.057. Epub 2010 Apr 20.

[50] X.-H. Peng, X. Qian, H. Mao, A. Y. Wang, Z. Chen, S. Nie, ans D. M. Shin. (2008). Targeted magnetic iron oxide nanoparticles for tumor imaging and therapy. International Journal of Nanomedicine, 3(3), 311–321.

[51] X. Peng, H. Chen, J. Huang, H. Mao, and M. D. Shin. (2011). Targeted Magnetic Iron Oxide Nanoparticles for Tumor Imaging and Therapy. Biomedical Engineering - From Theory to Applications. doi:10.5772/22873

[52] A.L. Oldenburg, V. Crecea, S. A. Rinne, and S. A. Boppart. (2008). Phase-resolved magnetomotive OCT for imaging nanomolar concentrations of magnetic nanoparticles in tissues. Optics Express, 16(15), 11525–11539

[53] R. John, and S. A. Boppart. (2011). Magnetomotive Molecular Nanoprobes. Current Medicinal Chemistry, 18(14), 2103–2114.

[54] W. Cai, T. Gao, H. Hong, and J. Sun. (2008). Applications of gold nanoparticles in cancer nanotechnology. Nanotechnology, Science and Applications, 2008(1), 10.2147/NSA.S3788. http://doi.org/10.2147/NSA.S3788

[55] C. S. Kim, X. Li, Y. Jiang, B. Yan, G. Y. Tonga, M. Ray, V. M. Rotello. (2015). Cellular imaging of endosome entrapped small gold nanoparticles. MethodsX, 2, 306–315. http://doi.org/10.1016/j.mex.2015.06.001

[56] H. S. Choi, and J. V. Frangioni. (2010). Nanoparticles for Biomedical Imaging: Fundamentals of Clinical Translation. Molecular Imaging, 9(6), 291–310.

[57] J. E. Rosen, S. Yoffe, and A. Meerasa. (2011). Nanotechnology and Diagnostic Imaging: New Advances in Contrast Agent Technology. Journal of Nanomedicine & Nanotechnology, 02(05). doi:10.4172/2157-7439.1000115

[58] S. Chapman, M. Dobrovolskaia, K. Farahani, A. Goodwin, A. Joshi, H. Lee, L. Yang. (2013). Nanoparticles for cancer imaging: The good, the bad, and the promise. Nano Today, 8(5), 454–460. http://doi.org/10.1016/j.nantod.2013.06.001

[59] Y. C. Cao. (2008). Nanomaterials for biomedical applications. Nanomedicine,3(4), 467-469. doi:10.2217/17435889.3.4.467

[60] M. Tang, L. Lei, S. Guo, and W. Huang. (2010). Recent progress in nanotechnology for cancer therapy. Chinese Journal of Cancer,29(9), 775-780. doi:10.5732/cjc.010.10075

[61] W. H. De Jong, and P. J. Borm. (2008). Drug delivery and nanoparticles: Applications and hazards. International Journal of Nanomedicine, 3(2), 133–149.

[62] K. C. Liu, and Y. Yeo. (2014). Extracellular stability of nanoparticulate drug carriers. Archives of Pharmacal Research, 37(1), 16–23. http://doi.org/10.1007/s12272-013-0286-0

[63] S. R. Mudshinge, A. B. Deore, S. Patil, and C. M. Bhalgat. (2011). Nanoparticles: Emerging carriers for drug delivery. Saudi Pharmaceutical Journal,19(3), 129-141. doi:10.1016/j.jsps.2011.04.001

[64] E. Blanco, H. Shen, and M. Ferrari. (2015). Principles of nanoparticle design for overcoming biological barriers to drug delivery. Nature Biotechnology, 33(9), 941–951. http://doi.org/10.1038/nbt.3330

[65] R. Singh, and J. W. Lillard. (2009). Nanoparticle-based targeted drug delivery. Experimental and Molecular Pathology, 86(3), 215–223. http://doi.org/10.1016/j.yexmp.2008.12.004

[66] T. L. Moore, L. Rodriguez-Lorenzo, V. Hirsch, S. Balog, D. Urban, C. Jud, A. Petri-Fink. (2015). Nanoparticle colloidal stability in cell culture media and impact on cellular interactions. Chem. Soc. Rev.,44(17), 6287-6305. doi:10.1039/c4cs00487f

[67] B. Issa, I. M. Obaidat, B. A. Albiss, and Y. Haik. (2013). Magnetic Nanoparticles: Surface Effects and Properties Related to Biomedicine Applications. International Journal of Molecular Sciences, 14(11), 21266–21305. http://doi.org/10.3390/ijms141121266

[68] M. F. Dumont, S. Yadavilli, R. W. Sze, J. Nazarian, and R. Fernandes. (2014). Manganese-containing Prussian blue nanoparticles for imaging of pediatric brain tumors. International Journal of Nanomedicine, 9, 2581–2595. http://doi.org/10.2147/IJN.S63472

[69] M. M. Eltabey, A. M. Massoud, and C. Radu. (2014). Microstructure and Superparamagnetic Properties of Mg-Ni-Cd Ferrites Nanoparticles. Journal of Nanomaterials, 2014, 1-7. doi:10.1155/2014/492832

[70] F. Gerbal, Y. Wang, F. Lyonnet, J.-C. Bacri, T. Hocquet, and M. Devaud. (2015). A refined theory of magnetoelastic buckling matches experiments with ferromagnetic and superparamagnetic rods. Proceedings of the National Academy of Sciences of the United States of America, 112(23), 7135–7140. http://doi.org/10.1073/pnas.1422534112

[71] B. A. Maher, I. A. M. Ahmed, V. Karloukovski, D. A. MacLaren, P. G. Foulds, D. Allsop, L. Calderon-Garciduenas. (2016). Magnetite pollution nanoparticles in the human brain. Proceedings of the National Academy of Sciences of the United States of America, 113(39), 10797–10801. http://doi.org/10.1073/pnas.1605941113

[72] L. B. Thomsen, T. Linemann, K. M. Pondman, J. Lichota, K. S. Kim, R. J. Pieters, T. Moos. (2013). Uptake and Transport of Superparamagnetic Iron Oxide Nanoparticles through Human Brain Capillary Endothelial Cells. ACS Chemical Neuroscience, 4(10), 1352–1360. http://doi.org/10.1021/cn400093z

[73] J. Matuszak, J. Baumgartner, J. Zaloga, M. Juenet, A. E. Silva, D. Franke, I. Cicha. (2016). Nanoparticles for intravascular applications: physicochemical characterization and cytotoxicity testing. Nanomedicine,11(6), 597-616. doi:10.2217/nnm.15.216

[74] J. M. Poller, J. Zaloga, E. Schreiber, H. Unterweger, C. Janko, P. Radon, R. P. Friedrich. (2017). Selection of potential iron oxide nanoparticles for breast cancer treatment based on in vitro cytotoxicity and cellular uptake. International Journal of Nanomedicine, 12, 3207–3220. http://doi.org/10.2147/IJN.S132369

[75] J. Lodhia, G. Mandarano, N. Ferris, P. Eu, and S. Cowell. (2010). Development and use of iron oxide nanoparticles (Part 1): Synthesis of iron oxide nanoparticles for MRI. Biomedical Imaging and Intervention Journal, 6(2), e12. http://doi.org/10.2349/biij.6.2.e12

[76] S. Prijic, J. Scancar, R. Romih, M. Cemazar, V. B. Bregar, A. Znidarsic, and G. Sersa. (2010). Increased Cellular Uptake of Biocompatible Superparamagnetic Iron Oxide Nanoparticles into Malignant Cells by an External Magnetic Field. The Journal of Membrane Biology, 236(1), 167–179. http://doi.org/10.1007/s00232-010-9271-4

[77] W. Li, Y. Liu, Z. Qian, and Y. Yang. (2017). Evaluation of Tumor Treatment of Magnetic Nanoparticles Driven by Extremely Low Frequency Magnetic Field. Scientific Reports, 7, 46287. http://doi.org/10.1038/srep46287

[78] B. Chertok, A. E. David, and V. C. Yang. (2010). Polyethyleneimine-modified iron oxide nanoparticles for brain tumor drug delivery using magnetic targeting and intra-carotid administration. Biomaterials, 31(24), 6317–6324. http://doi.org/10.1016/j.biomaterials.2010.04.043

[79] J. Huang, Y. Li, A. Orza, Q. Lu, P. Guo, L. Wang, H. Mao. (2016). Magnetic Nanoparticle Facilitated Drug Delivery for Cancer Therapy with Targeted and Image-Guided Approaches. Advanced Functional Materials, 26(22), 3818–3836. http://doi.org/10.1002/adfm.201504185

[80] S. Prijic, and G. Sersa. (2011). Magnetic nanoparticles as targeted delivery systems in oncology. Radiology and Oncology,45(1), 1-16. doi:10.2478/v10019-011-0001-z

[81] M. Babincova, and P. Babinec (2009) Magnetic drug delivery and targeting: principles and applications. Biomed Pap Med Fac Univ Palacky Olomouc Czech Repub. 2009 Dec;153(4):243-50.

[82] Y.-F. Wang, L. Liu, X. Xue, and X.-J. Liang. (2017). Nanoparticle-based drug delivery systems: What can they really do in vivo? F1000Research, 6, 681. http://doi.org/10.12688/f1000research.9690.1

[83] A. Wicki, D. Witzigmann, V. Balasubramanian, and J. Huwyler. (2015). Nanomedicine in cancer therapy: Challenges, opportunities, and clinical applications. Journal of Controlled Release,200, 138-157. doi:10.1016/j.jconrel.2014.12.030

[84] R. Bazak, M. Houri, S. E. Achy, S. Kamel, and T. Refaat. (2015). Cancer active targeting by nanoparticles: a comprehensive review of literature. Journal of Cancer Research and Clinical Oncology, 141(5), 769–784. http://doi.org/10.1007/s00432-014-1767-3

[85] P.-C. Liang, Y.-C. Chen, C.-F. Chiang, L.-R. Mo, S.-Y. Wei, W.-Y. Hsieh, and W.-L. Lin. (2016). Doxorubicin-modified magnetic nanoparticles as a drug delivery system for magnetic resonance imaging-monitoring magnet-enhancing tumor chemotherapy. International Journal of Nanomedicine, 11, 2021–2037. http://doi.org/10.2147/IJN.S94139

[86] A. Kumar, P. K. Jena, S. Behera, R. F. Lockey, S. Mohapatra, and S. Mohapatra. (2010). Multifunctional Magnetic Nanoparticles for Targeted Delivery. Nanomedicine, 6(1), 64–69. http://doi.org/10.1016/j.nano.2009.04.002

[87] A. M. Alkilany, and C. J. Murphy. (2010). Toxicity and cellular uptake of gold nanoparticles: what we have learned so far? Journal of Nanoparticle Research, 12(7), 2313–2333. http://doi.org/10.1007/s11051-010-9911-8

[88] A. Ali, H. Zafar, M. Zia, I. ul Haq, A. R. Phull, J. S. Ali, and A. Hussain. (2016). Synthesis, characterization, applications, and challenges of iron oxide nanoparticles. Nanotechnology, Science and Applications, 9, 49–67. http://doi.org/10.2147/NSA.S99986

[89] B. S. Ungureanu, C. M. Teodorescu, and A, Săftoiu. (2016) Magnetic nanoparticles for hepatocellular carcinoma diagnosis and therapy. (2016). Journal of Gastrointestinal and Liver Diseases,25(3). doi:10.15403/jgld.2014.1121.253.nan

[90] A. G. Próspero, C. C. Quini, A. F. Bakuzis, P. Fidelis-de-Oliveira, G. M. Moretto, F. P. F. Mello, J. R. A. Miranda. (2017). Real-time in vivo monitoring of magnetic nanoparticles in the bloodstream by AC biosusceptometry. Journal of Nanobiotechnology, 15, 22. http://doi.org/10.1186/s12951-017-0257-6

[91] V. Wünsch-Filho, D. M. Pelissari, F. E. Barbieri, L. Sant'Anna, C. T. Oliveira, J. F. Mata, L. Kheifets,. (2011). Exposure to magnetic fields and childhood acute lymphocytic leukemia in São Paulo, Brazil. Cancer Epidemiology,35(6), 534-539. doi:10.1016/j.canep.2011.05.008

[92] V. Zablotskii, T. Polyakova, O. Lunov, and A. Dejneka. (2016). How a High-Gradient Magnetic Field Could Affect Cell Life. Scientific Reports, 6, 37407. http://doi.org/10.1038/srep37407

[93] K. Pawłowska-Góral, M. Kimsa-Dudek, A. Synowiec-Wojtarowicz, J. Orchel, M. Glinka, and S. Gawron. (2016). Effect of static magnetic fields and phloretin on antioxidant defense system of human fibroblasts. Environmental Science and Pollution Research International, 23, 14989–14996. http://doi.org/10.1007/s11356-016-6653-x

[94] S. Tocchio, B. Kline-Fath, E. Kanal, V. J. Schmithorst, and A. Panigrahy. (2015). MRI Evaluation and Safety in the Developing Brain. Seminars in Perinatology, 39(2), 73–104. http://doi.org/10.1053/j.semperi.2015.01.002

[95] J. I. Rodriguez-Devora, S. Ambure, Z.-D. Shi, Y. Yuan, W. Sun, and T. Xu. (2012). Physically facilitating drug-delivery systems. Therapeutic Delivery, 3(1), 125–139. http://doi.org/10.4155/tde.11.137

[96] S. Chaudhary, C. A. Smith, P. del Pino, J. M. de la Fuente, M. Mullin, A. Hursthouse, C. Berry. (2013). Elucidating the Function of Penetratin and a Static Magnetic Field in Cellular Uptake of Magnetic Nanoparticles. Pharmaceuticals, 6(2), 204–222. http://doi.org/10.3390/ph6020204

[97] S. Jafari, S. Maleki Dizaj, and K. Adibkia. (2015). Cell-penetrating peptides and their analogues as novel nanocarriers for drug delivery. BioImpacts : BI, 5(2), 103–111. http://doi.org/10.15171/bi.2015.10

[98] L. Zhang, Y. Hou, Z. Li, X. Ji, Z. Wang, H. Wang, X. Zhang. (2017). 27 T ultra-high static magnetic field changes orientation and morphology of mitotic spindles in human cells. eLife, 6, e22911. http://doi.org/10.7554/eLife.22911

[99] D. Coletti, L. Teodori, M. C. Albertini, M. Rocchi, A. Pristerà, M. Fini, S. Adamo. (2007). Static magnetic fields enhance skeletal muscle differentiation in vitro by improving myoblast alignment. Cytometry Part A,71A(10), 846-856. doi:10.1002/cyto.a.20447

[100] A. Ortolani, M. Bianchi, M. Mosca, S. Caravelli, M. Fuiano, M. Maracci, and A. Russo. (2016). The prospective opportunities offered by magnetic scaffolds for bone tissue engineering: a review. Joints, 4(4), 228–235. http://doi.org/10.11138/jts/2016.4.4.228

[101] Y. Zhai, J. Su, W. Ran, P. Zhang, Q. Yin, Z. Zhang, Y. Li. (2017). Preparation and Application of Cell Membrane-Camouflaged Nanoparticles for Cancer Therapy. Theranostics, 7(10), 2575–2592. http://doi.org/10.7150/thno.20118

[102] B. Alberts. (2015). Molecular biology of the cell. New York: Garland Science.

[103] Plasma Membrane. Retrieved July 27th, 2017, from http://biology.tutorvista.com/animal-and-plant-cells/plasma-membrane.html

[104] Cooper, G. M., & Hausman, R. E. (2016). The cell: a molecular approach. Yale J Biol Med. 2014 Dec; 87(4): 603–604.

[105] Cell Membranes. Retrieved July 27, 2017, from http://www.sparknotes.com/biology/cellstructure/cellmembranes/section1.rhtml

[106] A. E. Nel, L. Mädler, D. Velegol, T. Xia, E. M. Hoek, P. Somasundaran, M. Thompson. (2009). Understanding biophysicochemical interactions at the nano–bio interface. Nature Materials,8(7), 543-557. doi:10.1038/nmat2442

[107] P. N. Navya, and H. K. Daima. (2016). Rational engineering of physicochemical properties of nanomaterials for biomedical applications with nanotoxicological perspectives. Nano Convergence, 3(1), 1. http://doi.org/10.1186/s40580-016-0064-z

[108] A. Bhaumik, A. M. Shearin, R. Delong, A. Wanekaya, and K. Ghosh. (2014). Probing the Interaction at the Nano–Bio Interface Using Raman Spectroscopy: ZnO Nanoparticles and Adenosine Triphosphate Biomolecules. The Journal of Physical Chemistry. C, Nanomaterials and Interfaces, 118(32), 18631–18639. http://doi.org/10.1021/jp506200a

[109] L. Wang, M. B. O'Donoghue, W. Tan. (2006). Nanoparticles for multiplex diagnostics and imaging. Nanomedicine (Lond). Dec;1(4):413-26. doi: 10.2217/17435889.1.4.413

[110] R. Wilson. (2008). The use of gold nanoparticles in diagnostics and detection. Chem Soc Rev. 2008 Sep;37(9):2028-45. doi: 10.1039/b712179m.

[111] A. Hospital, J. R. Goñi, M. Orozco, and J. L. Gelpí. (2015). Molecular dynamics simulations: advances and applications. Advances and Applications in Bioinformatics and Chemistry : AABC, 8, 37–47. http://doi.org/10.2147/AABC.S70333

[112] I. M. Kapetanovic. (2008). COMPUTER-AIDED DRUG DISCOVERY AND DEVELOPMENT (CADDD): in silico-chemico-biological approach. Chemico-Biological Interactions, 171(2), 165–176. http://doi.org/10.1016/j.cbi.2006.12.006

[113] P. Gkeka and Z. Cournia. (2015) Molecular Dynamics simulations of lysozyme in water. MSc in Bioinformatics and Medical Informatics Biomedical research foundation, Academy of Athens.

[114] W. Phadungsukanan, M. Kraft, J. A. Townsend, and P. Murray-Rust. (2012). The semantics of Chemical Markup Language (CML) for computational chemistry : CompChem. Journal of Cheminformatics, 4, 15. http://doi.org/10.1186/1758-2946-4-15

[115] J. R. Perilla, B. C. Goh, C. K. Cassidy, B. Liu, R. C. Bernardi, T. Rudack, K. Schulten. (2015). Molecular dynamics simulations of large macromolecular complexes. Current Opinion in Structural Biology, 31, 64–74. http://doi.org/10.1016/j.sbi.2015.03.007

[116] C. Kandt, W. L. Ash, D. P. Tieleman. (2007) Setting up and running molecular dynamics simulations of membrane proteins. Methods. 2007 Apr;41(4):475-88. https://doi.org/10.1016/j.ymeth.2006.08.006

[117] D. C. Rapaport. (2010). The art of molecular dynamics simulation. Cambridge: Cambridge Univ. Press.

[118] D. Frenkel, and B. Smit. (2012). Understanding molecular simulation: from algorithms to applications. San Diego, Calif.: Academic Press.

[119] C. J. Cramer. (2013). Essentials of computational chemistry: theories and models. Chichester: John Wiley & Sons.

[120] R. Stote, D. Dejaegere, and D. Kuznetsov. (2016) Molecular Dynamics simulations. Retrieved September 19, 2017, from http://www.ch.embnet.org/MD_tutorial/pages/MD.Part3.html

[121] K. Vanommeslaeghe, O. Guvench, and A. D. MacKerell. (2014). Molecular Mechanics. Current Pharmaceutical Design, 20(20), 3281–3292.

[122] K. Vanommeslaeghe, O. Guvench, and A. D. MacKerell. (2014). Molecular Mechanics. Current Pharmaceutical Design, 20(20), 3281–3292.

[123] S. A. Adcock, and J. A. McCammon. (2006). Molecular Dynamics: Survey of Methods for Simulating the Activity of Proteins. Chemical Reviews, 106(5), 1589–1615. http://doi.org/10.1021/cr040426m

[124] P. J. Steinbach. (2010, November 15). The Empirical Potential Energy Function. Retrieved September 19, 2017, from https://cmm.cit.nih.gov/intro_simulation/node15.html

[125] M. P. Allen, and D. J. Tildesley. (2017). Computer simulation of liquids. Oxford: Oxford University Press.

[126] M. Ciocoiu. (2015). Materials behavior: research methodology and mathematical models. Toronto: Apple Academic Press.

[127] H. Watanabe, N. Ito, and C. Hu. (2012). Phase diagram and universality of the Lennard-Jones gas-liquid system. The Journal of Chemical Physics,136(20), 204102. doi:10.1063/1.4720089

[128] M. D. Pierro, R. Elber, and B. Leimkuhler. (2015). A Stochastic Algorithm for the Isobaric-Isothermal Ensemble with Ewald Summations for all Long Range Forces. Journal of Chemical Theory and Computation, 11(12), 5624–5637. http://doi.org/10.1021/acs.jctc.5b00648

[129] Lennard-Jones potential. (2017, August 29). Retrieved September 20, 2017, from https://en.wikipedia.org/wiki/Lennard-Jones_potential

[130] Coulomb's law. (2017, September 12). Retrieved September 20, 2017, from https://en.wikipedia.org/wiki/Coulomb%27s_law

[131] D. Dibenedetto, G. Rossetti, R. Caliandro, P. Carloni. A molecular dynamics simulation-based interpretation of nuclear magnetic resonance multidimensional heteronuclear spectra of α-synuclein•dopamine adducts. Biochemistry. 2013 Sep 24;52(38):6672-83. doi: 10.1021/bi400367r.

[132] T. A. Manz, and D. S. Sholl. (2010). Chemically Meaningful Atomic Charges That Reproduce the Electrostatic Potential in Periodic and Nonperiodic Materials. Journal of Chemical Theory and Computation,6(8), 2455-2468. doi:10.1021/ct100125x.

[133] X-ray crystallography. (2017, September 13). Retrieved September 20, 2017, from https://en.wikipedia.org/wiki/X-ray_crystallography
[134] A. L. Fuller. (2009). Applications of X-ray crystallography: studies into the structural perturbations of peri-substituted naphthalene derivatives(Unpublished master's thesis). University of St Andrews, November. doi:http://hdl.handle.net/10023/826
[135] N. Grozev, I. Botiz, and G. Reiter. (2008). Morphological instabilities of polymer crystals. The European Physical Journal E,27(1), 63-71. doi:10.1140/epje/i2008-10352-1
[136] S. R. Miller. (2007). Scandium bearing open framework materials (Unpublished master's thesis). doi:http://hdl.handle.net/10023/570
[137] Miller index. (2017, September 12). Retrieved September 20, 2017, from https://en.wikipedia.org/wiki/Miller_index
[138] X.-D. Su, H. Zhang, T. C. Terwilliger, A. Liljas, J. Xiao, and Y. Dong. (2015). Protein Crystallography from the Perspective of Technology Developments. Crystallography Reviews, 21(1-2), 122–153. http://doi.org/10.1080/0889311X.2014.973868
[139] A. M. Glazer. (2016). Crystallography: a very short introduction. New York, NY: Oxford University Press.
[140] R. M. Nix. (2014). Retrieved September 21, 2017, from http://www.chem.qmul.ac.uk/surfaces/scc/scat1_1b.htm
[141] Crystal directions, planes and the zone axis. (2016). Retrieved September 21, 2017, from http://www.ebsd.com/popup/crystal_directions.htm
[142] M. D. Graef, and M. E. McHenry. (2013). Structure of materials: an introduction to crystallography, diffraction and symmetry. Cambridge: Cambridge University Press.
[143] C. Hammond. (2015). The basics of crystallography and diffraction. Oxford: Oxford University Press.
[144] T. P. Almeida, A. R. Muxworthy, A. Kovács, W. Williams, P. D. Brown, and R. E. Dunin-Borkowski. (2016). Direct visualization of the thermomagnetic behavior of pseudo–single-domain magnetite particles. Science Advances, 2(4), e1501801. http://doi.org/10.1126/sciadv.1501801
[145] Monnington, Amy Elizabeth (2014) Modelling magnetite biomineralisation: the interactions of proteins and Fe3O4 surfaces. Doctoral thesis, University of Huddersfield.
[146] N. A. Spaldin. (2012). Magnetic materials: fundamentals and applications. Cambridge: Cambridge University Press.
[147] P. Kumar, M. Bulk, A. Webb, L. Weerd, T. H. Oosterkamp, M. Huber, and L. Bossoni. (2016). A novel approach to quantify different iron forms in ex-vivo human brain tissue. Scientific Reports, 6, 38916. http://doi.org/10.1038/srep38916
[148] M. Friák, A. Schindlmayr, and M. Scheffler. (2007). Ab initio study of the half-metal to metal transition in strained magnetite. New Journal of Physics,9(1), 5-5. doi:10.1088/1367-2630/9/1/005
[149] L. Perloff. (2013). Black, opaque octahedral crystals of magnetite on matrix. [Photograph found in Photo Atlas of Minerals, Isle of Ischia, near Naples, Compania, Italy]. Retrieved September 21, 2017.
[150] Wikipedia. (2017, September 21). Sphere. Retrieved September 22, 2017, from https://en.wikipedia.org/wiki/Sphere
[151] T. Hales. (2005). A proof of the Kepler conjecture. Annals of Mathematics,162(3), 1065-1185. doi:10.4007/annals.2005.162.1065
[152] Wikipedia. (2017, September 21). Kepler conjecture. Retrieved September 22, 2017, from https://en.wikipedia.org/wiki/Kepler_conjecture
[153] H. Cohn, A. Kumar, S. Miller, D. Radchenko, and M. Viazovska. (2017). The sphere packing problem in dimension 24. Annals of Mathematics,185(3), 1017-1033.
[154] M. M. Ghobashy. (2017). In-situ core-shell polymerization of magnetic polymer nanocomposite (PAAc/Fe3O4) particles via gamma radiation. Nanocomposites,3(1), 42-46.
[155] Description of Magnetite Structure. Retrieved September 22, 2017, from http://www.cmp.liv.ac.uk/shrike/mphys/chap2.html
[156] I. R. Krauss, A. Merlino, A. Vergara, and F. Sica. (2013). An Overview of Biological Macromolecule Crystallization. International Journal of Molecular Sciences, 14(6), 11643–11691. http://doi.org/10.3390/ijms140611643

[157] Bragg, W H.; The Structure of Magnetite and the Spinels Nature (London), 1915, 95, 561-561.
[158] Santos-Carballal, D.; Roldan, A.; Grau-Crespo, R.; NH de Leeuw, A DFT study of the structures, stabilities and redox behaviour of the major surfaces of magnetite Fe3O4 Phys.Chem.Chem.Phys. 2014,16:21082-21097.
[159] Liu, XY.; Bennema, P. Theoretical consideration of the growth morphology of crystals Physical Review B. 1996,53(5):2314-2325.
[160] MAPS, Version 4.0.1, Scienomics, Paris, France
[161] W. Humphrey, A. Dalke, K. Schulten, “VMD: visual molecular dynamics”, J Mol Graph. 1996;14:33–8.
[162] D. Friedmann, T. Messick, and R. Marmorstein. (2011). Crystallization of Macromolecules. Current Protocols in Protein Science / Editorial Board, John E. Coligan ... [et Al.], 0 17, Unit17.4. http://doi.org/10.1002/0471140864.ps1704s66
[163] Barber, CB.; Dobkin, DP.; Huhdanpaa, H. The Quickhull Algorithm for Convex Hulls, ACM TRANSACTIONS ON MATHEMATICAL SOFTWARE 1995, Volume: 22 Issue: 4 Pages: 469-483
[164] Wikipedia. Convex hull. Retrieved September 22, 2017, from https://en.wikipedia.org/wiki/Convex_hull
[165] Truncation (geometry). Retrieved September 22, 2017, from http://www.wikiwand.com/en/Truncation_(geometry)
[166] Finch, C. A., Poly(vinyl alcohol) : Developments. John Wiley and Sons: London, 1992.
[167] Lyoo, W. S.; Ha, W. S. Polymer 1996, 37(14), 3121–3129.
[168] Choi, J. H.; Lyoo, W. S.; Ko, S. W. Macromol. Chem. Phys. 1999, 200, 1421–1427.
[169] Lyoo, W. S.; Ha, W. S. Polymer 1999, 40, 497–505.
[170] Lyoo, W. S.; Han, S. S.; Yoon, W. S.; Ji, B. C.; Lee, J.; Cho, Y. W.; Choi, J. H.; Ha, W. S. J. Appl. Polym. Sci. 2000, 77, 123–134.
[171] Finch, C. A., Poly(vinyl alcohol) : Properties and Applications. John Wiley and Sons: London, 1973.
[172] Probiotics-prebiotics. Retrieved June 05, 2017 from http://instandpure.com/probiotics-prebiotics/
[173] T. H. Schmidt, C. Kandt, J. Chem. Inf. Model. 2012, 52, 2657.
[174] W. Humphrey, A. Dalke, K. Schulten, J. Mol. Graph. Model. 1996, 14, 33.
[175] B. Sommer, T. Dingersen, C. Gamroth, S. E. Schneider, S. Robert, J. Kruger, K. J. Dietz, J. Chem. Inf. Model. 2011, 51, 1165.
[176] M. G. Wolf, M. Hoefling, C. Aponte-Santamaria, H. Grubmuller, G. Groenhof, J. Comput. Chem. 2010, 31, 2169.
[177] L. Martinez, R. Andrade, E. G. Birgin, J. M. Martinez, J. Comput. Chem. 2009, 30, 2157.
[178] Jo S, Kim T, Im W (2007) Automated Builder and Database of Protein/Membrane Complexes for Molecular Dynamics Simulations. PLoS ONE 2(9): e880.
[179] Petrache HI, Grossfield A, MacKenzie KR, Engelman DM, Woolf TB (2000) Modulation of glycophorin A transmembrane helix interactions by lipid bilayers: molecular dynamics calculations. J Mol Biol 302: 727–746.
[180] Woolf TB, Roux B (1994) Molecular dynamics simulation of the gramicidin channel in a phospholipid bilayer. Proc Natl Acad Sci U S A 91: 11631–11635.
[181] Woolf TB, Roux B (1996) Structure, energetics, and dynamics of lipid-protein interactions: A molecular dynamics study of the gramicidin A channel in a DMPC bilayer. Proteins 24: 92–114.
[182] Im W, Roux B (2002) Ions and counterions in a biological channel: a molecular dynamics simulation of OmpF porin from Escherichia coli in an explicit membrane with 1 M KCl aqueous salt solution. J Mol Biol 319: 1177–1197.
[183] Abraham, M.J.; D. van der Spoel; Lindahl, E.; Hess, B.; and the GROMACS development team, GROMACS User Manual version 5.0.6, www.gromacs.org (2015).
[184] T. Manz, D. Sholl; Chemically Meaningful Atomic Charges That Reproduce the Electrostatic Potential in Periodic and Nonperiodic Materials; J. Chem. Theory Comput. 2010, 6, 2455–2468.
[185] Huang, J.; MacKerell AD, Jr. CHARMM36 all-atom additive protein force field: validation based on comparison to NMR data. J Comput Chem. 2013, Sep 30,34(25):2135-45.

[186] Charles Aguilar, M; Wagner, B.; De Almeida; Willian Rocha, R; The electronic spectrum of Fe2+ ion in aqueous solution: A sequential Monte Carlo/quantum mechanical study, CHEM. PHYS. LETT. 449 (2007) 144–148.

[187] Pekka, M.; Lennart N., Structure and Dynamics of the TIP3P, SPC, and SPC/E Water Models at 298 K, J. Phys. Chem. A, 2001, 105 (43), pp 9954–9960.

[188] Glenn Martyna, J; Remarks on "Constant-temperature molecular dynamics with momentum conservation", Physical Review E. 1994, 50(4):3234-3236.

[189] Essmann, U.; Perera, L; Berkowitz, M.L.; Darden, T.; Lee, H; and Pedersen, L.G. A smooth particle mesh Ewald method. J. Chem. Phys. 1995, 103:8577–8593.

[190] E. Arunan, G. R. Desiraju, R. A. Klein, J. Sadlej, S. Scheiner, I. Alkorta, D.C. Clary, R. H. Crabtree, J. J. Dannenberg, P. Hobza, H. G. Kjaergaard, A. C. Legon, B. Mennucci, D. J. Nesbitt, Defining the hydrogen bond: An account (IUPAC Technical Report), Pure Appl. Chem. 2011, Vol. 83, No. 8, pp. 1619–1636.

[191] L. Fu, and H.–T. Ke. (2016). Nanomaterials incorporated ultrasound contrast agents for cancer theranostics. Cancer Biology & Medicine, 13(3), 313–324. http://doi.org/10.20892/j.issn.2095-3941.2016.0065

[192] S. S. Chandratre, and A. K. Dash. (2015). Multifunctional Nanoparticles for Prostate Cancer Therapy. AAPS PharmSciTech, 16(1), 98–107. http://doi.org/10.1208/s12249-014-0202-z

[193] A. Ahmad, and S. M. Gadgeel. (2016). Lung cancer and personalized medicine: novel therapies and clinical management. Cham: Springer.

[194] W. Lohcharoenkal, L. Wang, Y. C. Chen, and Y. Rojanasakul. (2014). Protein Nanoparticles as Drug Delivery Carriers for Cancer Therapy. BioMed Research International, 2014, 180549. http://doi.org/10.1155/2014/180549.

[195] J. Meller. 2001. Molecular Dynamics. eLS [doi:10.1038/npg.els.0003048].

[196] MATLAB R2016b, The MathWorks, Inc., Natick, Massachusetts, United States.

[197] Python Software Foundation. Python Language Reference, version 3.6. Available at http://www.python.org.

[198] ISO/IEC. (2014). ISO International Standard ISO/IEC 14882:2014(E) – Programming Language C++. [Working draft]. Geneva, Switzerland: International Organization for Standardization (ISO). Retrieved from https://isocpp.org/std/the-standard

[199] Qt, Cross-platform software development for embedded & desktop, version 4.8. Available at https://www.qt.io/.

[200] Wu, EL, Cheng, X, Jo, S, Rui, H, Song, KC, Dávila-Contreras, EM, Qi, Y, Lee, J, Monje-Galvan, V, Venable, RM, Klauda, JB, Im, W (2014). CHARMM-GUI Membrane Builder toward realistic biological membrane simulations. J. Comput. Chem 35:1997-2004

[201] J. D. H. Donnay, D. Harker, 1937: A new law of crystal morphology extending the law of Bravais. Am. Mineral. 22(5): 446-467.